KATHOLIEKE UNIVERSITEIT
LEUVEN

Arenberg Doctoral School of Science, Engineering & Technology
Faculty of Engineering
Department of Mechanical Engineering

Passive Hypersonic Boundary Layer Transition Control Using Ultrasonically Absorptive Carbon-Carbon Ceramic with Random Microstructure

Alexander WAGNER

Dissertation presented in partial
fulfillment of the requirements for
the degree of Doctor
in Engineering

September 2014

Passive Hypersonic Boundary Layer Transition Control Using Ultrasonically Absorptive Carbon-Carbon Ceramic with Random Microstructure

Alexander WAGNER

Jury:
Prof. dr. ir. H. Hens, chair
Prof. dr. ir. J. Steelant, supervisor
Prof. Dr.-Ing. K. Hannemann, co-supervisor
Prof. dr. ir. E. Van den Bulck
Prof. dr. G. Paniagua
Prof. dr. ir. J. Meyers
Prof. O. Chazot
(von Karman Institute for Fluid Dynamics)

Dissertation presented in partial fulfillment of the requirements for the degree of Doctor in Engineering

September 2014

D/D/2014/7515/124
ISBN 978-94-6018-900-5

Acknowledgments

I would first like to thank Johan Steelant for supervising and guiding my research. I also want to thank Klaus Hannemann for co-supervising the work and moreover for providing me all possible support to conduct the present study in the Spacecraft Department of DLR Göttingen. The academic freedom and confidence I was granted by both supervisors throughout the study is very much appreciated.
I also want to thank the entire HEG team, Jan Martinez Schramm, Stuart Laurence, Ingo Schwendtke, Bartek Klaskala, Uwe Frenzel and Patrick Schenke for their support during the test campaigns at HEG. In particular the support provided by Jan Martinez Schramm in all aspects of HEG was (and is) highly appreciated. Furthermore, I value all the thorough discussions and the close cooperation on the topic with Viola Wartemann and Markus Kuhn. Moreover, I would like to thank Alexander V. Fedorov for the numerous discussions which I appreciate greatly.

Finally, I would like to thank my wife Kerstin for her continuous support and understanding throughout the past years. I also thank my two children Jannek and Pia who, without being aware of it, help me not to lose sight of the important things in life.

Abstract

In the presented work ultrasonically absorptive carbon-carbon ceramic was shown for the first time to delay hypersonic laminar to turbulent boundary-layer transition. Three 7° half-angle cones with nose radii between 0.1 mm and 5.0 mm and a total length of 1100 mm were tested at zero angle of attack in the High Enthalpy Shock Tunnel Göttingen (HEG) of the German Aerospace Center (DLR) at Mach 7.5. One model was equipped with an in-house manufactured ultrasonically absorptive carbon-carbon ceramic insert with random microstructure covering one third of the model surface in circumferential direction. The remaining model surface consisted of polished steel and served as reference surface. The free-stream unit Reynolds number was varied over a range of $\mathrm{Re_m} = 1.5 \cdot 10^6\ \mathrm{m^{-1}}$ to $\mathrm{Re_m} = 9.8 \cdot 10^6\ \mathrm{m^{-1}}$ at stagnation enthalpies of $\mathrm{h_0} \approx 3.2$ MJ/kg and a wall temperature to total temperature ratio of $\mathrm{T_w/T_0} \approx 0.1$. The ultrasonic absorption properties of carbon-carbon ceramic (C/C) were assessed theoretically by means of the quasi-homogeneous absorber theory and experimentally by means of direct reflection coefficient measurements at varying ambient pressure levels. For the first time broadband ultrasonic sound transducers with resonance frequencies of up to 370 kHz were applied to directly cover the frequency range of interest with respect to the second mode instabilities observed on cone geometries in HEG. C/C was found to absorb up to 19% of the acoustic power transmitted towards the surface. The experimental results were found to be in good agreement with the theory. The present study revealed the second mode instability to dominate the transition process. A distinctive attenuation of instability waves and a delay of boundary layer transition on the ultrasonically absorptive carbon-carbon insert was proven by means of fast-response surface pressure measurements, high speed schlieren visualization and surface heat flux measurement.

Beknopte samenvatting

In dit werk wordt voor het eerst aangetoond dat koolstof gebaseerde keramische materialen de transitie van een laminaire naar een turbulente grenslaag kunnen uitstellen bij hypersone stromingen. Hierbij wordt vooral aandacht besteed aan de secondaire instabiliteit die de dominante mode is bij hoge snelheden. Drie kegelvormige windtunnelmodellen met een totale lengte van 1100 mm en met neus radii die variëren van 0.1 mm tot 5 mm werden experimenteel getest bij een snelheid van Mach 7.5 in de Hoge Enthalpie Schok Tunnel (HEG) van het Duitse Centrum voor Lucht- en Ruimtevaart (DLR) in Göttingen (D). Een van de modellen uit gepolijst staal werd voorzien van een keramisch inzetstuk dat een derde van het oppervlak innam en waarbij de microstructuur absorberend is in het ultrasone spectrum. De geteste eenheids-Reynolds getallen varieerden van $\mathrm{Re_m} = 1.5 \cdot 10^6\ \mathrm{m^{-1}}$ tot $\mathrm{Re_m} = 9.8 \cdot 10^6\ \mathrm{m^{-1}}$ bij een totale enthalpie van $\mathrm{h_0} \approx 3.2\ \mathrm{MJ/kg}$ en een relatieve wandtemperatuur van $T_w/T_0 \approx 0.1$. Voor het eerst werden breedband transducers voor ultrasoon geluid met resonantie frequenties tot 370 kHz toegepast om het volledige spectrum van de secondaire instabiliteiten te capteren bij de verschillende uitgeteste windtunnelmodellen. De ultrasone karakteristieken van het koolstof gebaseerd keramisch materiaal werd eerst theoretisch bepaald op basis van quasi-homogene absorptie theorie en dan experimenteel door middel van directe meeting van reflectie coëfficiënten bij variërende omgevingsdrukken. Het toegepaste keramisch materiaal was in staat om tot 19 % van het akoestische vermogen te absorberen overeenstemmend met de theoretisch voorspelde waarden. Deze eigenschap liet toe om de secondaire stabiliteit wel degelijk te dempen en het transitiepunt uit te stellen. Dit werd in HEG experimenteel overtuigend aangetoond op de conische modellen met de keramische inzetstukken dankzij het gebruik van hoogfrequente druksensoren, hoge-snelheid schlieren visualisatie en thermische flux sensoren.

Abbreviations

AFRL	Airforce Research Laboratory
ALTP	Atomic Layer Thermopile
ASD	Amplitude Spectral Density
ATLLAS	Aerodynamic and Thermal Load Interactions with Lightweight Advanced Materials for High Speed Flight
C/C	Carbon-Carbon Ceramic
CFD	Computational fluid dynamics
CFRP	Carbon Fiber Reinforced Plastic
CUBRC	Calspan - University of Buffalo Research Center
DLR	Deutsches Zentrum für Luft- und Raumfahrt (German Aerospace Center)
EQ	Equilibrium
HEG	High Enthalpy Shock Tunnel Göttingen (DLR)
HIEST	High-enthalpy shock tunnel (JAXA)
HIFiRE	Hypersonic International Flight Research Experimentation Program
JAXA	Japan Aerospace Exploration Agency
NASP	National Aerospace Plane Program
NEQ	Non-equilibrium
LAPCAT	Long-Term Advanced Propulsion Concepts and Technologies
LED	Light-Emitting Diode
SA	Spalart-Almaras turbulence model
SHEFEX	Sharp Edge Flight Experiment
TAU	DLR's Navier-Stokes flow solver
TF	Thin Film
TPS	Thermal Protection System
UAC	Ultrasonically Absorptive Coatings

Superscripts and subscripts

0	reservoir (total) conditions
1	conditions just upstream of a shock wave
2	conditions just downstream of a shock wave
c	convective, critical
eff	effective
k	breaking value
r	recovery condition
ref	reference
s	surface coordinate
$stat$	static condition
t	total conditions
TB	transition onset on blunted cone (first measurable rise of heat flux)
TS	transition onset on sharp cone (first measurable rise of heat flux)
w	wall condition
x	coordinate along model symmetry axis
∞	free-stream conditions
*	pore entrance conditions
$'$	fluctuation quantity

List of Symbols

Roman Symbols

a	speed of sound	m/s
A	area	m^2
A	amplitude	-
c	phase speed	m/s
c_p	isobaric specific heat capacity	J/(kg K)
d	thickness, pore depth	m
D	pore diameter	m
f	frequency	Hz
h	specific enthalpy	J/kg
H	enthalpy	J
I	intensity	W/m^2
k	wave number	m^{-1}
k_a	complex wave number	m^{-1}
L	model length	m
m	mass	kg
M	Mach number	-
N	N-factor	-
p	pressure	Pa
$\dot{q}$	heat flux density	W/ m^2
r	radius	m
r_s	flow resistivity	Pa s/m
R	specific gas constant	J/(kg K)
R	reflection coefficient	-
R_n	cone tip radius	m
Re	Reynolds number	-
Re_m	unit Reynolds number	m^{-1}
Re_N	Reynolds number based on tip radius	-
Re_t	transition Reynolds number	-

s	streamwise surface coordinate	m
t	time	s
T	temperature	K
u	velocity along x	m/s
V	volume	m^3
x, y, z	coordinate	m
z	impedance	Ns/m^3

Greek symbols

α	wave number in x direction	m^{-1}
β	wave number in y direction	m^{-1}
β	absorption coefficient	-
γ	ratio of specific heats	-
γ	surface tension	kg/s^2
κ	structure coefficient	-
μ	dynamic viscosity	Pa s
ν	acoustic particle velocity	m/s
θ	contact angle, angle of incidence	$^\circ$
ρ	density	kg/m^3
σ	porosity	-
τ	tortuosity	-
ω	angular frequency	s^{-1}
ψ	wave angle	$^\circ$
Ξ	length specific flow resistance	Pa s / m^2

Contents

List of Figures

List of Tables

Chapter 1

Introduction

A body moving through a viscous fluid is surrounded by a thin bounded layer - the boundary layer. This fundamental principle was first demonstrated by Ludwig Prandtl in 1904, [92]. He demonstrated that the flow field around a body can be separated into a thin layer in the vicinity of the body (the boundary layer) where viscosity plays a distinctive role, and a layer further away in which viscosity can be neglected, [104]. His discovery was considered a breakthrough for practical fluid engineering and aerodynamics.
Boundary layer transition describes the process in which a laminar flow, i.e. a flow moving in parallel layers of different velocities without intense exchange between the layers, transitions to a turbulent flow with irregular motion in lateral direction, [105]. The change of state leads to an increase of the wall shear stress and thus wall heat flux. In hypersonic flows the wall heat flux of a turbulent boundary layer can be up to 8 times higher compared to the corresponding laminar flow, [124]. Considering a hypersonic flight vehicle the boundary layer state directly affects the viscous drag, vehicle controllability, engine inlet performance, combustor mixing efficiency and aerodynamic heating, [143]. The latter is crucial since it dominates all aspects involved in the design, i.e. materials, vehicle shape, and internal heat management, [91].

Despite the fact that hypersonic boundary layer transition has been an area of intense research over the past decades, the transition process is still not completely understood, [96]. This results in a huge uncertainty in the prediction of the transition location which has tremendous implications on the design and performance of, e.g., vehicles for sustained hypersonic flight. The consequences were found to be thoroughly concluded by the Defense Science Board which

evaluated the U.S. National Aerospace Plane Program (NASP) in 1988, [28]:

"The degree of uncertainty significantly affects the ... estimates of engine performance, structural heating and drag. The assumption made for the point of transition can affect the design vehicle gross take off weight by a factor of two or more".

Conceptual studies on future hypersonic commercial transport such as the European LAPCAT, ATLLAS or SKYLON programs assume a maximum take off weight in the range of $300 - 400$ t with a payload to gross weight fraction of approximately $4 - 6$ %, [117, 145, 61]. The comparison to the uncertainty in the vehicle gross take off weight illustrates the necessity to understand the transition process helping to predict and control boundary layer transition. Whitehead [143] provided an elementary calculation, shown in figure 1.1, which quantitatively addresses the implication of the transition location on the payload fraction of a single stage to orbit mission. The vertical line, with a zero reference value, represents a reasonable design target of a single stage to orbit vehicle. It can be seen that the reduction of vehicle drag and heating can result in a 60 % to 70 % increase of the payload fraction over the fully turbulent condition.

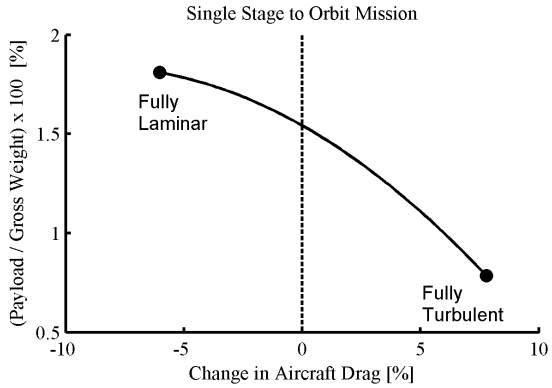

Figure 1.1: Impact of boundary layer transition on the payload fraction for a single stage to orbit mission, reproduced from Whitehead [143].

Beyond the prediction of the transition location, the increase of the laminar portion of the boundary layer is of critical importance to the design and optimization of these vehicles, [29]. This ultimately motivates the development of concepts to control hypersonic transition.

1.1 Hypersonic Boundary Layer Transition

1.1.1 Path to Transition

"The evolution to turbulence in compressible boundary layers follows the generally accepted view that laminar-turbulent transition is a consequence of the nonlinear response of the boundary layer to forcing disturbances", Saric et al. [103]. Among others such disturbances could include free-stream turbulence, entropy disturbances, radiated sound, surface roughness or vibration which are part of the test environment.

In a first step in the transition process described in figure 1.2 the disturbances enter the boundary layer providing the initial condition of amplitude, frequency and phase for the breakdown of laminar flow. This process is known as *receptivity*, Morkovin [81]. It is still not well understood until today. For disturbances with

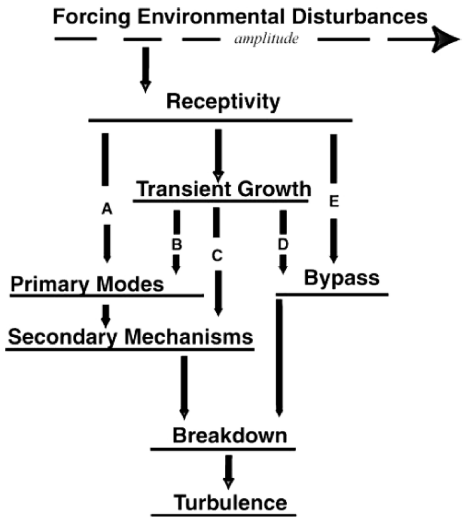

Figure 1.2: Path to transition, Saric et al. [102].

small amplitude the initial growth is weak and primary instability modes (path A) develop. This transition path is the only one well described by the linear stability theory which will be briefly described in section 1.1.3. After reaching a certain amplitude, secondary mechanisms occur which are characterized by three-dimensional and non-linear interactions. At this stage disturbance growth rapidly increases and breakdown to turbulence occurs.
In test environments with high free-stream disturbance levels and in the vicinity

of large roughness the development of primary modes can be by-passed as described by Morkovin [81] and Reshotko [96]. In this instance secondary mechanisms or turbulent spots develop, followed by a rapid break-down to turbulence (path E). However, the by-pass mechanisms are not well understood. A recent review on the effect of isolated and distributed roughness on hypersonic transition was provided by Schneider [106]. The general effect of wind tunnel free-stream disturbances on transition was studied by Pate [87] showing a direct relationship between transition Reynolds numbers and free-stream disturbance levels.

At least three additional possible ways of the transition process exist, as figure 1.2 depicts. Path B, C and D involve transient growth. It describes the growth of essentially stable modes due to their interaction with other stable modes. According to Reshotko [97] the superposition of the modes leads to a temporary (transient) increase of the disturbance amplitude. Depending on the amplitude the transition process will follow path B, C or D (in this order with increasing amplitude). Recent studies of transient growth were conducted by Choudhari and Fischer [14] who investigated roughness induced transient growth, in particular the effect of roughness height, shape and size of discrete roughness elements. The role of transient growth in surface roughness induced transition was investigated by Reshotko and Tumin [98]. The authors found a good agreement with experimental data and concluded that the transient growth theory is a promising explanation for early transition due to distributed roughness. Additional information on by-pass transition associated with transient growth are provided by Reshotko [97].

1.1.2 Streamwise Instabilities

Depending on the initial conditions, the Reynolds number and the vehicle shape, a variety of different instabilities can develop jointly or independently, [103]. In the presence of predominantly two-dimensional compressible boundary layers, small free-stream disturbances and negligible surface roughness, multiple subsonic modes of different order are present as shown by Mack [71]. The lowest order mode is the vortical mode corresponding to the Tollmien-Schlichting instability in subsonic boundary layers. Modes of higher order correspond to acoustic waves trapped in the boundary layer. They also exist in absence of viscosity, thus considered being an inviscid instability, and were first discovered numerically by Mack [68, 69]. Therefore, higher order modes are generally referred to as 'Mack' modes. Independently from Mack's discovery Gill [32] analytically found higher order modes in 2-D and axisymmetric jets or wakes. The first of these acoustic modes is called the 'second mode' which will be given

particular attention in the present study. Numerical studies on an insulated flat plate revealed higher order modes to appear for Mach numbers above 2.2 gaining experimental significance at Mach number around 4 and above, [69]. Figure 1.3 provides the effect of the free-stream Mach number on the spatial

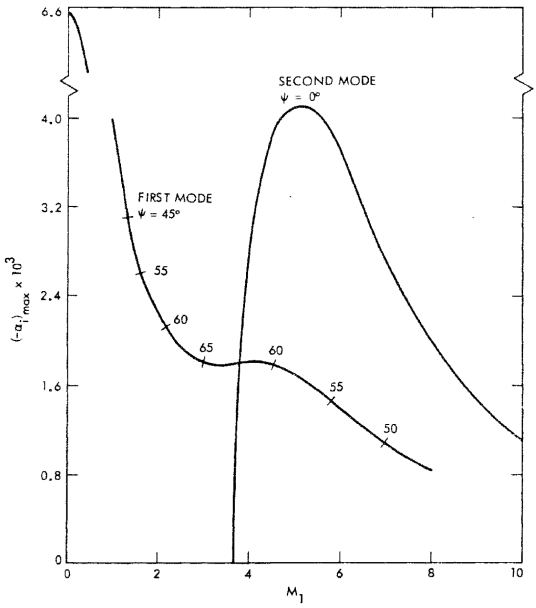

Figure 1.3: Effect of free-stream Mach number on the spatial amplification rates of the first and second mode disturbance above an insulated flat plate, provided for the most unstable wave angle, Mack [70].

amplification rates of the first and the second mode in the boundary layer of an insulated flat plate. The amplification rates are shown for the most unstable wave angles ψ, being the angle between the wave front normal and the direction of the flow. It can be seen that for Mach numbers above 4 the second mode amplification rates exceed those of the first mode. At this point the second mode becomes the dominant instability. However, most of the practically relevant configurations do not have perfectly insulated walls. Consequently, the wall appears to be cooled which is known to stabilize the first mode but destabilizes the second mode, [69]. In this particular case the Mach number limit at which the second mode becomes the dominant instability is shifted to lower values.

Acoustic Modes (Mack Modes)

As described before, acoustic modes, also called 'Mack' modes, are acoustic waves which are trapped in the boundary layer. This implies that they do not radiate outward. According to Mack [73] the necessary condition for the existence of acoustic modes is an embedded region of local supersonic mean flow relative to the phase speed of the instability wave. Mack provides further explanation saying that the local convective Mach number, M_c, must be supersonic at the wall and in the adjacent region whose thickness is less than the boundary layer thickness. The convective Mach number is the Mach number component of the flow in the direction of the wave-number vector and relative to the phase speed, [73]. As seen in figure 1.3 for second mode disturbances the most unstable wave angle is found at $\psi = 0$ which simplifies the following notation. Several definitions of the convective Mach number were found. The following definition was found useful in this study:

$$M_c = \frac{c - u(y)}{a(y)}$$

with $u(y)$ being the velocity profile, $a(y)$ the local speed of sound and c the disturbance phase speed. Morkovin [82] clarified the structure of this layer based on Mack's inviscid linear stability theory by providing figure 1.4 . The

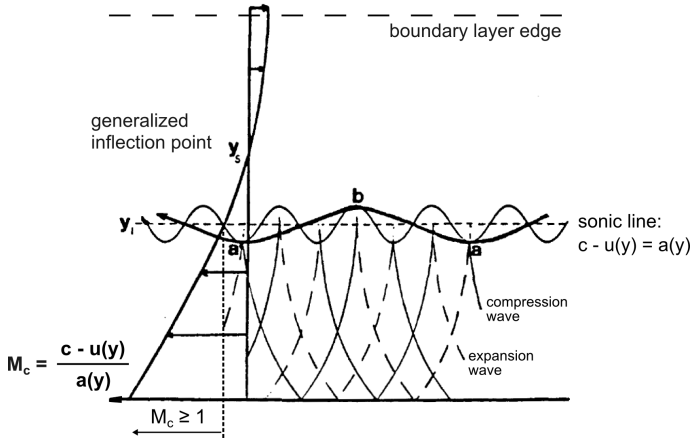

Figure 1.4: Acoustic modes trapped in the boundary layer, stationary in this frame of reference, adapted from Morkovin [82].

figure shows the profile of the convective Mach number over the extent of the boundary layer. The relative sonic line indicates the location at which $M_c = 1$, i.e. the disturbances are sonic relative to the local mean flow. In the layer

below, the local convective Mach number is supersonic and thus fulfills the requirement for the existence of higher modes. Furthermore, the figure depicts acoustic modes trapped in the boundary layer provided in the reference frame traveling with the mean speed at the generalized inflection point, y_s. The modes travel along Mach lines being reflected at the wall and the sonic line. Each time an acoustic wave is reflected at the sonic line it is changed from a compression to an expansion wave and vice versa. Besides, harmonic vorticity and entropy perturbations travel along the sonic line as stated by Morkovin [82]. These disturbances are phase tuned to the acoustic modes.
Finally the generalized inflection point y_s is introduced. It plays the same role in the compressible theory as the inflection point in the incompressible theory. Its existence is a precondition for the existence of neutral disturbances, [69].

1.1.3 Linear Stability Theory

In principle, linear stability theory addresses the question whether a small sinusoidal disturbance introduced into a given laminar flow will be amplified or damped, [69]. The theory covers the first stage of the eigenmode development, i.e. the development of primary modes as shown along path A in figure 1.2. It does not cover the non-linear process by which a boundary layer changes from laminar to turbulent flow and does not predict the transition location. However, the theory provides information on the amplification and damping rates as well as wave number, Reynolds number and phase velocity of neutral disturbances. A detailed review of the theory is provided by Mack [69, 71].

The principle of the linear stability analysis is to introduce small sinusoidal disturbances into the Navier-Stokes equations to derive the range of unstable frequencies. A typical assumption is that the mean flow quantities do not vary significantly over the wavelength of a disturbance. Consequently, the mean flow components in x and z direction and the temperature depend on y alone, the surface normal velocity is equal to zero, [103]. The introduced disturbances are sufficiently small allowing to linearize the Navier-Stokes equations by neglecting the quadratic terms of the disturbance. A three-dimensional normal mode disturbance is typically expressed by a harmonic wave of the form

$$q'(x, y, z, t) = q(y)\, e^{i(\alpha x + \beta z - \omega t)}, \tag{1.1}$$

where q' can be any fluctuation quantity such as velocity, pressure, density or temperature. The variables x, y, z might form an orthogonal coordinate system with x pointing in streamwise direction, y being normal to the surface and z pointing in the transverse direction. The quantities t, α, β and ω denote the time, the wave numbers in x and z direction as well as the angular frequency. $q(y)$ represents the normal mode shape of the given flow quantity. After solving

the corresponding eigenvalue problem it can be evaluated whether the traveling waves are stable or unstable by analyzing the sign of the exponent. For most practical applications a spatial stability analysis is of interest. It is performed assuming ω to be real and α to be complex, i.e. $\alpha = \alpha_r + \alpha_i$. Referring to equation 1.1 unbounded exponential growth of the (unstable) wave is expected if the imaginary part of α is negative. The calculation of the N-factor for the most amplified wave angles is conducted by integrating the amplification rate $-\alpha_i$ between two streamwise separated locations:

$$N = \ln \frac{A_2}{A_1} = \int_{s_2}^{s_1} -\alpha_i \, ds \tag{1.2}$$

with A_1 being the initial amplitude at the beginning of disturbance growth located at s_1. Analogous, A_2 denotes the disturbance amplitude at the downstream location s_2.

The present studies were accompanied by numerical investigations conducted by Wartemann [136] addressing second mode damping by means of porous coatings with regular microstructure.

1.2 Hypersonic Transition Control

Transition control addresses active and passive techniques to control the boundary layer state. The purpose of these techniques can be both, the delay of boundary layer transition or the promotion of the transition process for instance on engine inlets. A subset of the active control methods are the reactive methods using closed-loop control schemes. The principle of reactive methods is to cancel or reduce boundary-layer disturbances by artificially introducing out-of-phase disturbances into the boundary layer e.g. by applying wall vibration, periodic blowing/suction or heating/cooling, [26]. In subsonic flows active control techniques, particularly continuous suction and blowing, are well developed and to some extent used on today's operating aircraft. However, in hypersonic flows those techniques are limited in application due to the system complexity and the harsh environment. According to Kimmel [52] techniques with the highest potential for integration onto hypersonic vehicles are passive or non-reactive techniques such as porous coatings, local heating/cooling and vehicle shaping, i.e. the utilization of blunted nose tips and leading edges. Nevertheless, to effectively delay hypersonic boundary layer transition the dominant instability mechanism has to be identified to choose the appropriate control strategy. In the case of small free-stream disturbances, negligible surface roughness and predominantly two-dimensional hypersonic boundary layers,

second-mode instabilities are known to be the dominant mechanism leading to transition as shown theoretically by Malik [74]. Therefore, ultrasonically absorptive coatings (UAC) have the potential to be used for passive hypersonic boundary layer control delaying laminar-turbulent transition by means of second mode damping. The concept was proven theoretically by Malmuth [75] and confirmed experimentally by Fedorov [26] and Rasheed [93, 94] using cone models with porous surfaces of regularly spaced cylindrical blind holes. A significant delay of transition onset was reported. Additional measurements were conducted by Fedorov [24] showing a substantial decrease of the instability growth above the porous surface. Furthermore, Fedorov [27], Maslov [78, 77] and Lukashevich [65] conducted measurements on cones with randomly structured felt metal which confirmed the before observed damping effect on the second mode instability.
An alternative material is carbon-carbon ceramic (C/C) which will be investigated in detail in the present study. C/C combines ultrasonic absorption properties with a practical TPS (thermal protection system) potential. It exhibits a natural porosity with random microstructure typical for TPS materials. Furthermore, it provides a high temperature stability in absence of oxygen and represents an intermediate state of C/C-SiC which has been used successfully as TPS on hypersonic vehicles, [123, 142].
Beyond, C/C was shown to be applicable for transpiration cooling. It was successfully applied in the scope of the DLR Sharp Edge Flight Experiment (SHEFEX II) in wind tunnel tests in the High Enthalpy Shock Tunnel Göttingen (HEG), [10], and in flight, [9].
Therefore, porous materials are of particular interest for the TPS development of future re-entry vehicles with high aerodynamic efficiency, i.e. high lift-to-drag ratio, or hypersonic cruise vehicles. The present study highlights the vast potential of C/C as multifunctional TPS material, which however requires a targeted development.

To efficiently damp the second mode instability on a hypersonic vehicle the properties of the porous coating have to be adapted to the aerodynamic environment. Therefore, the acoustic characteristic of the material must be known. For thin porous coatings used on wind tunnel models the ultrasonic absorption characteristic has been determined first by Tsyryulnikov and Mironov [122]. Direct measurements of the absorptivity for frequencies of up to approximately 70 kHz under atmospheric pressure were conducted comparing the amplitudes of signals reflected by a porous surface to those reflected by an ideally sound reflecting surface. Fedorov et al. [25] conducted direct measurements at a distinct ultrasonic frequency of 180 kHz at ambient pressures in the range of $0.02 \cdot 10^5$ Pa to $0.8 \cdot 10^5$ Pa. The present study extends the investigated frequency range up to approximately 400 kHz and thus directly covers the 2nd mode instability frequencies observed in this study.

1.3 Scope of the Study

The present study investigates a passive hypersonic boundary layer transition control scheme applying for the first time a porous material with random microstructure which has the potential to be used as thermal protection system. The scheme is based on the reduction of the second mode instability growth rate by means of ultrasonically absorptive carbon-carbon ceramic. The study is conducted in the High Enthalpy Shock Tunnel Göttingen (HEG) and represents the first systematic investigation of hypersonic boundary layer transition in HEG.

After introducing the subject of the study in the present chapter, the methodology is addressed in chapter 2. It provides all required information on the test facilities, the wind tunnel models, their instrumentation and the calibration routine used in HEG to derive the free-stream quantities.
A major part of the present work was the assessment of the ultrasonic absorption properties of carbon-carbon ceramic which is addressed in chapter 3. The absorption properties were derived by means of the quasi-homogeneous absorber theory, section 3.3, and direct reflection coefficient measurements, section 3.4. The latter investigation required the design and realization of a specific test rig and the development of an elaborate test procedure to overcome deficits of this technique.
Chapter 4 provides the experimental results. It is subdivided in a section addressing the experiments on the solid wall, section 4.1, and a section addressing the experiments on the porous wall, section 4.2. The first section provides a basic understanding of the transition process in HEG addressing the facility dependence of the process and the effect of bluntness. Furthermore, it identifies the second mode instability as the dominant boundary layer instability. The section on the porous wall results proves carbon-carbon ceramic to effectively delay hypersonic boundary layer transition on slender cones in HEG.
Finally, the study is concluded with a detailed discussion of the results in chapter 5. Its main emphasis is to link the findings provided in the individual chapters to provide a complete picture of the subject.

Chapter 2

Methodology

The present chapter introduces the methodology followed within the study. It addresses the test facilities involved, their mode of operation as well as the wind tunnel models including the instrumentation. Furthermore, the calibration of the free-stream test conditions in the High Enthalpy Shock Tunnel Göttingen is described showing a good agreement between experimentally and numerically obtained free-stream quantities.

2.1 The High Enthalpy Shock Tunnel Göttingen (HEG)

2.1.1 Overview

The High Enthalpy Shock Tunnel Göttingen (HEG) is a free-piston driven reflected shock tunnel providing a pulse of gas to a hypersonic nozzle at stagnation pressures of up to 200 MPa and stagnation enthalpies of up to 25 MJ/kg, [22, 21, 39, 38]. The overall length and mass of the facility is 60 m and 250 t, respectively. As shown in figure 2.1 the tunnel consists of three main sections. The driver section consists of a secondary reservoir which can be pressurized up to 23 MPa and a 33 m long compression tube. The adjoining shock tube (or driven tube) has a length of 17 m. The end of the tube is equipped with a sleeve to allows tests at high enthalpy, [40]. The shock tube is separated from the compression tube by a $3 - 18$ mm stainless steel main diaphragm. The third section is separated by a thin Mylar® diaphragm and

consists of the Laval nozzle, the test section and the dump tank. An Overview on the characteristic dimensions of HEG is provided in table A.1. All available HEG nozzles are presented in figure A.1.

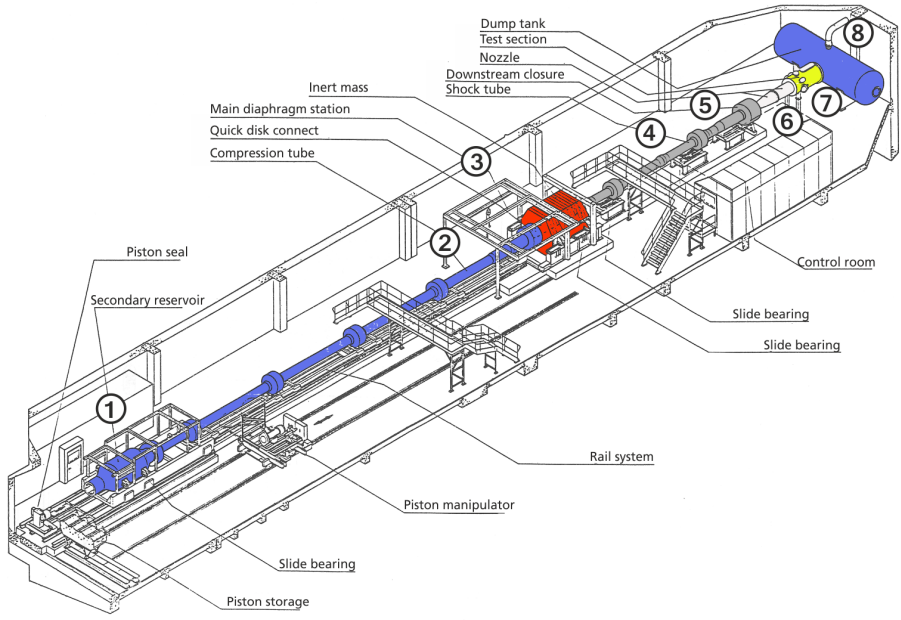

Figure 2.1: Schematic view of HEG, Martinez Schramm [107].

HEG was designed to investigate hypersonic flows with high enthalpies. To obtain such enthalpies, high shock speeds in the shock tube are required which is realized by generating a driver gas with a high speed of sound. This is achieved through a combination of light driver gas and a high driver gas temperature. Various techniques have been developed to generate such driver gas conditions, e.g. heating through electrical resistance, arc heating, combustion drivers or shock heated drivers. However, these techniques have a number of disadvantages such as difficult design constraints due to e.g. the high heating loads, [63, 66]. Furthermore, the presence of heavy combustion products in the driver gas reduces the driver speed of sound which is in contrast to the necessity of high gas temperatures, [80]. To bypass these problems the free-piston compression process, which allows high volumetric compression ratios without the previously mentioned disadvantages, was developed by Stalker [113, 114, 115]. Its principle is shown in 2.2. A driver gas particularly suited for the above requirements is helium. Compared to other gases it behaves as a perfect gas up to high

temperatures and thus requires less energy to raise its temperature.

2.1.2 Operating Principle

At the beginning of a test in HEG the piston is at the upstream end of the compression tube, see position 1 in figure 2.1. The compression tube, position 2, is filled with a driver gas at low pressure and ambient temperature. A helium/argon mixture is typically used as driver gas. While the pressure in the secondary reservoir is increased the piston is kept in place. Once the required pressure to drive the piston is reached it is released. At this point the energy of the expanding gas in the secondary reservoir accelerates the piston down the compression tube. By the time the pressure behind the piston is equal to the pressure in front, the piston has sufficient kinetic energy to continue the compression process due to the piston inertia. Its kinetic energy is then transferred to the driver gas which is adiabatically compressed until the downstream main diaphragm ruptures, position 3, and the shock-tube flow is initiated. To obtain a reproducible diaphragms rupture process all diaphragms are cross-scratched. Diaphragms of different thickness are used to realize a different burst pressures. Figure 2.2 shows the wave diagram for the time after shock-tube flow was initiated. To ensure constant nozzle reservoir conditions

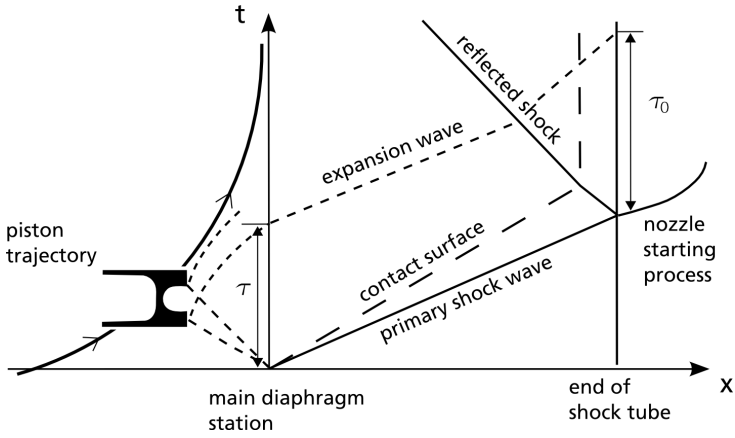

Figure 2.2: Wave diagram of flow after main diaphragm rupture with tailored interface, adapted from Stalker [115].

in the order of few milliseconds the conditions in the driver gas must be held constant for a similar time period. Therefore, the main diaphragm is allowed to rupture before the compression process is completed and the piston comes to

rest. With a cross-section area of the compression tube being sufficiently large compared to the cross-section area of the shock tube entrance (typical values are between 9 and 20, for HEG 13.4) it is possible to tune the piston trajectory such that after diaphragm rupture the volume displaced by the piston matches the mass flow into the shock tube, position 4. Thereby, the loss of driver gas due to the expansion into the shock tube is compensated and the driver pressure remains constant for a small holding time. Further, expansion waves reflected at the compression tube end wall are reduced or canceled. The pressure decrease at the end of the compression process is transmitted along the shock tube. It reaches the end of the shock tube after the time τ_0 after shock reflection and limits the maximum test time, see figure 2.2.

At the downstream end of the shock tube a thin secondary diaphragm is used to separate the shock tube containing the test gas from the downstream part of the tunnel which is kept under vacuum conditions. After the main diaphragm rupture a primary shock wave travels along the shock tube, figure 2.2. The shock wave is reflected at the shock tube end wall and ruptures the secondary diaphragm mounted close to the nozzle throat, position 5. The reflected shock leaves a region of almost stationary high temperature test gas in the nozzle reservoir which subsequently expands through the convergent-divergent hypersonic nozzle, position 6, into the test section, position 7, and the dump tank, position 8. The reflected shock, traveling towards the main diaphragm station, meets the contact surface of the driver gas and greatly reduces the velocity of the interface. In most cases a transmitted shock and a secondary reflected shock or an expansion fan are created. The arrival of these disturbances limit the duration of uniform flow entering the nozzle. However, a combination of initial compression tube and shock tube condition can be found to avoid the transmitted reflected shock to cause disturbances in the stagnant reservoir test gas due to a secondary reflected shock. This mode is referred to as the 'tailored interface' mode, [30]. Figure 2.3 provides the wave diagrams of a undertailored, tailored and overtailored interface. The undertailored case is obtained by increasing the initial pressure in the shock tube taking the tailored case as baseline. In this case the contact surface will reverse direction and an expansion wave will expand the test gas in the nozzle reservoir leading to a decrease of free-stream pressure during the test time. In contrast, if the initial shock tube pressure is lower the contact surface will continue moving forward and a shock is propagated down the shock tube again. The test gas compression is continued leading to a pressure increase during the test time. The operation of a shock tunnel in tailored mode allows a test time limited by driver gas contamination or loss of pressure in the stagnation region due to the gas expanding through the nozzle. However, by operating the tunnel in a slightly overtailored mode the pressure loss is compensated leading to an extend

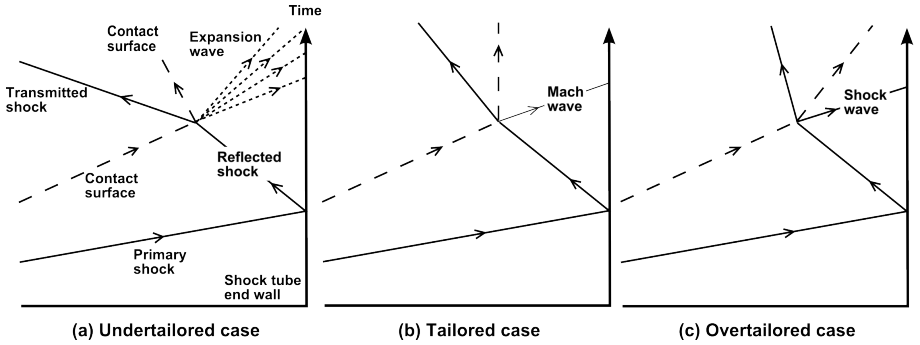

Figure 2.3: Wave diagrams of different tailoring cases, adapted from Nishida [84].

of test time. This technique is known as the equilibrium interface technique, investigated by Copper [17].

2.2 The High Enthalpy Shock Tunnel HIEST

The High Enthalpy Shock Tunnel (HIEST) is a large-scale free-piston reflected shock tunnel similar to HEG. It is operated by the Japan Aerospace Exploration Agency (JAXA). Similar to HEG, the facility consists of a high pressure air reservoir, a compression tube, a shock tube, a nozzle and a test section. The total length of the facility is 80 m. The principle of operation is identical to that of HEG, i.e. the driver gas is adiabatically compressed by a free piston generating a strong shock wave which propagates down the shock tube. The high-enthalpy stagnation conditions of the test gas are again attained by a reflected shock wave at the shock tube end. The Mach number and unit Reynolds number in this facility ranges from $M = 6$ to $M = 10$ and $Re_m = 0.25 \cdot 10^6$ m^{-1} to $Re_m = 10 \cdot 10^6$ m^{-1} respectively.

HIEST can generate stagnation pressures up to 150 MPa and stagnation enthalpies up to 25 MJ/kg. Conical and contoured nozzles are available at HIEST. Detailed information on the HIEST facility are provided in Itoh et al. [49, 48].
In the present study experiments in HEG are compared to experiments in HIEST which were conducted and partly published by Tanno [119, 120]. A contoured nozzle with an exit diameter of 0.8 m and an area ratio of 256 was used for all considered tests for comparison with HEG.

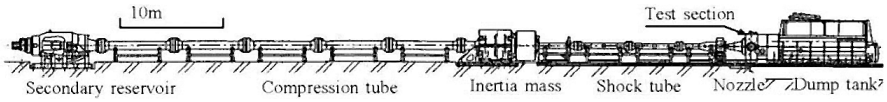

Compression tube	Bore: ϕ600 mm, Length: 42 m	Stagnation enthalpy	3 to 25 MJ/kg
Shock tube	Bore: ϕ180 mm, Length: 17 m	Stagnation pressure	12 to 150 MPa
Piston mass	220 to 780 kg	Test time	2 ms or longer
Nozzle	Conical: exit diameter ϕ 1.2 m		
	Contoured: exit diameter ϕ 0.8 m		

Figure 2.4: Schematic view of the HIEST, [119].

2.3 Model and Instrumentation

The section provides an overview on the three wind tunnel models used in the scope of this study. All models were positioned in the HEG test section as depicted in figure A.4. Further a description of the applied measurement techniques is provided.

2.3.1 Wind Tunnel Models

Cone Model 1

Cone model 1 was provided by JAXA[1] in the frame of the JAXA/DLR cooperative research on 'High Enthalpy Aerothermodynamics'. The model was a blunted 7° half-angle cone with an overall length of 1100 mm and an exchangeable nose tip. A tip with 2.25 mm radius was provided by JAXA. An additional tip with 5 mm radius was manufactured by DLR. The overall layout of the model is shown in figure 2.5. It is based on the dimensions of the HIFiRE-I flight vehicle forebody, [53, 127, 2, 3, 60, 116, 51]. Since the nose radius on HIFiRE-I was 2.5 mm, additional tests using a corresponding nose tip were performed in HEG to exactly match the flight test forebody geometry. Special emphasis was put on the fact that no discontinuities were present on the model surface. The tested model was equipped with 121 thermocouples, 4 pressure transducers of type KULITE™ XCL-100-100A and 10 piezoelectric fast response pressure transducers of type PCB132A37. The model was supported by a sting system at nominal 0° angle of attack. The instrumentation was chosen such that the transition location could be identified by evaluating the surface heat-flux distribution based on thermocouple readings. The flush-mounted KULITE™ pressure transducers were used to measure the surface pressure to control the angle of attack and the yaw angle of the model. Eight fast response pressure

[1] Japan Aerospace Exploration Agency

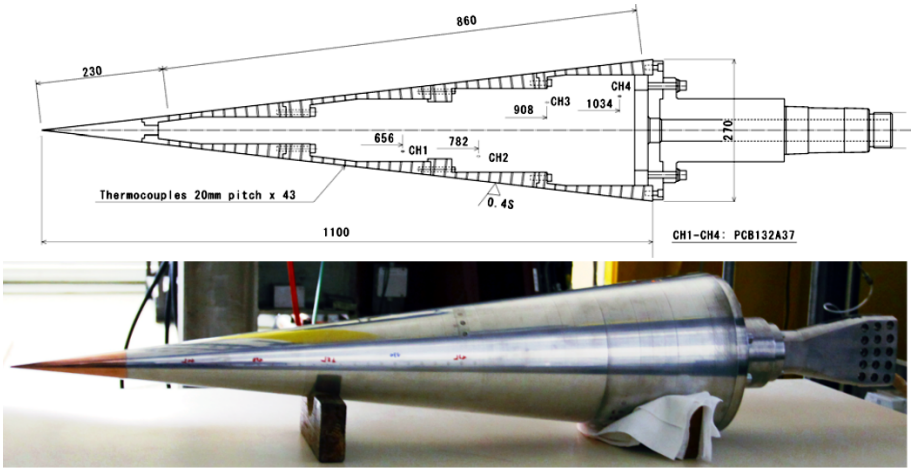

Figure 2.5: Technical drawing and photographic view of cone model 1. All dimensions are provided in millimeter.

transducers were grouped in pairs of two and flush mounted along the model at x = 656 mm, x = 782 mm, x = 908 mm and x = 1034 mm, measured from the sharp tip. These transducers feature a resonance frequency above 1 MHz and were used to measure pressure fluctuations in the boundary-layer above the cone surface. Piezoelectric type pressure transducers are sensitive to accelerations present in the model during the test time. Therefore, the pressure transducers were installed using cotton threads and silicone caulk to mechanically decouple the transducers and to reduce the transfer of high frequency vibrations from the model, [119]. For the tests in HEG, two additional blind reference pressure transducers of the same type were mounted at x = 908 mm and x = 1034 mm without access to the flow field. These transducers were used to measure the frequency components of the mechanical vibrations which possibly affect the transducer, despite the elaborate mounting. The recorded spectra were later on used to correct the data of the transducers exposed to the flow field.

Cone Model 2

Cone model 2 was a 7° half-angle blunted cone with an overall length[2] of 1077 mm and an exchangeable nose tip. The model was designed and manufactured in DLR in the scope of the present study. For the experiments a nose radius of 2.5 mm and 5 mm radius was used. The model was equipped

[2]The overall length measured from the extrapolated sharp tip was 1100 mm.

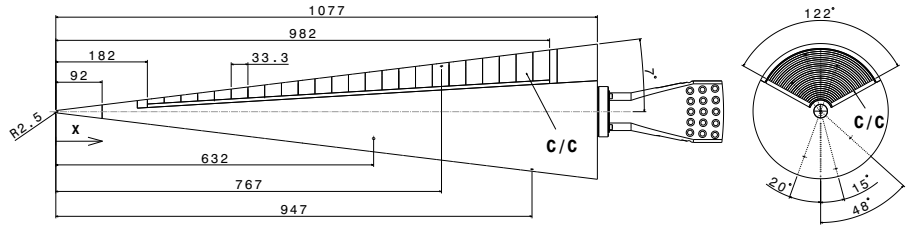

Figure 2.6: Technical drawing of cone model 2. All dimensions are provided in millimeter.

with a 835 mm long insert of ultrasonically absorptive carbon-carbon ceramic (C/C). The insert started at 182 mm measured from the 2.5 mm model tip and covers 122° of the model surface in circumferential direction. A detailed description of the C/C material follows in section 3. Figure 2.6 shows the basic dimensions of the model. Special attention was paid to the model surface quality. To minimize potential discontinuities at junctions the model was machined with the C/C insert installed. The nose tips were pre-machined separately and fitted to the main model by hand. The main model and the model tip were manufactured from stainless steel and attached to a sting system mounted at nominal zero angle of attack. The model was equipped with 49 flush mounted coaxial thermocouples of type E with a spacing of 33.3 mm to measure the transition location by means of surface heat flux evaluation. Thereof, 24 transducers were installed along the center ray of the porous surface as depicted in figure 2.6 on the right. Additional 25 thermocouples were installed along a ray directly opposite on the solid surface with identical x-coordinates starting at 190 mm from the model tip. Furthermore, 12 piezoelectric PCB132A32 fast response pressure transducers were flush mounted on the solid surface at x = 632 mm, x = 767 mm, x = 947 mm and on the porous surface at x = 632 mm, x = 767 mm, x = 932 mm from the blunted nose tip. The transducer locations were rotated about 48°, 15° and −20° from the center ray, see figure 2.6 on the right. Piezoelectric type pressure transducers are sensitive to accelerations. This time a silicone shroud was applied to mechanically decouple the transducers from the model as described for model 1. Reference pressure transducers of the same type mounted inside the model, and therefore not exposed to the flow, were used at each fast response pressure transducer location. Additional 8 pressure transducers of type KULITE™ XCL-100-100A were installed adjacent to the PCB™ transducer location at 182 mm and 402 mm on the solid surface to measure the surface pressure along the model. The transducer positions on the model were chosen based on the experience gathered in studies on cone model 1, reported in Wagner et al. [133].

Due to model manufacturing constraints the porous layer thickness varied in the range of 5 mm and 17 mm as shown in the enlarged cross section view in figure 2.7. Special attention is paid to this issue in section 3.3 which addresses the acoustic properties of the material.

Cone Model 3

The third model was a 7° half-angle cone with a total length of 1222 mm. It was designed to study the effect of local wall heating or cooling on hypersonic boundary layer transition. Therefore, the model was equipped with a section made of copper which could be temperature controlled between 345 K and 525 K. The temperature variable section ranges from 126 mm to 326 mm, measured from the sharp nose tip. The model could be fitted with a 0.1 mm tip and a 2.5 mm nose tip. Further, the model was equipped with four inserts starting at 346 mm from the tip. Each insert had a length of 871 mm and was designed to accommodate a specific type of transducer. Figure 2.8 shows the position of each insert and the transducer assignment. In the scope of the present study transducer based measurements with fast response pressure transducers (PCB™) and thermocouples (TC) were evaluated. Eleven PCB132A32 fast response pressure transducers were installed starting at x = 391 mm with a spacing of x = 39.4 mm. The same techniques as described in section 2.3.1 were used to mechanically decouple the transducers from the model. Further, 32 thermocouples with a spacing of 24.6 mm starting at x = 382 mm were integrated.

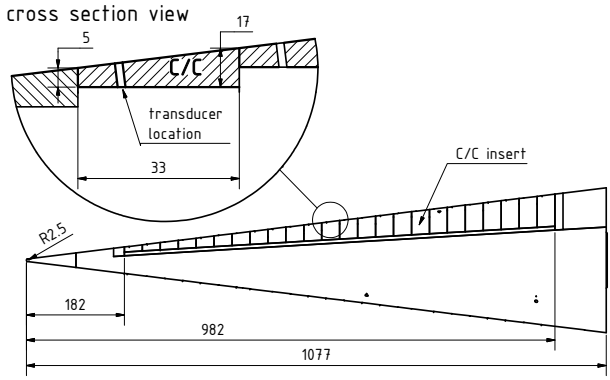

Figure 2.7: Section view of model 2 indicated minimum and maximum porous layer thickness. All dimensions are provided in millimeter.

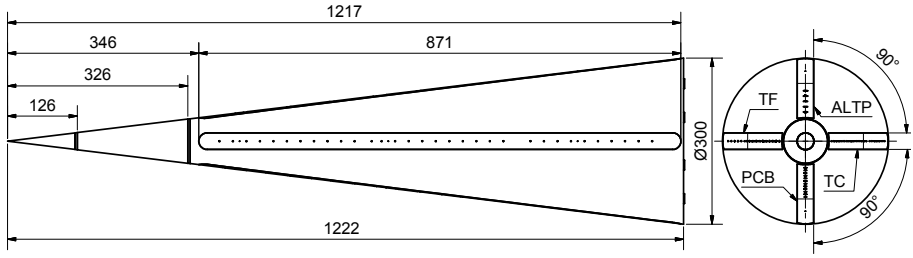

Figure 2.8: Technical drawing of cone model 2, ALTP: atomic layer thermopile, TC: thermocouple, PCB™: fast response surface pressure transducers, TF: thin film transducers. All dimensions are provided in millimeter.

To ensure the comparability of all tests conducted in the scope of this study cone model 3 was used at a surface temperature corresponding to the tests on cone model 1 and 2.

2.3.2 Instrumentation

Fast Response Pressure Transducer

Fast response pressure transducers of type PCB132A37 and PCB132A32 were used in this study. Both sensor types make use of the piezoelectric effect, i.e. an electrical charge is generated when a piezoelectric element is strained by an external force. Due to the functional principle such transducers are generally not suited for static pressure measurements, [89]. However the sensors offer response times of few microseconds and resonance frequencies above 1 MHz and thus are capable of measuring pressure fluctuations in a bandwidth of 11 kHz to 1 MHZ, [90]. The transducers are voltage mode-type sensors which use a built-in microelectronic amplifier to condition the signal, referred to as ICP®(Integrated Circuit Piezoelectric). The sensors possess a sensitivity of approximately 20.3 mV/kPa and a resolution of 7 Pa. In combination with a diameter of 3.8 mm to 5.6 mm a good spacial and temporal resolution is provided making them well suited to study second mode instabilities.

Coaxial Thermocouples

Coaxial thermocouples represent a robust technique to measure surface temperatures in harsh test environments. The functional principle of the gauge is based on the thermoelectric effect (or Seebeck effect). In the present

study coaxial thermocouples of type E were used. The corresponding chromel-constantan pairing is recommended for use in a temperature range of $-270°C$ to $1000°C$ and has a sensitivity of 68 μV/K, [1, 16, 101]. The thermocouple consists of an outer tube (chromel) and a coaxial center wire (constantan) which are electrically isolated from each other. By grinding the transducer head a junction between the two materials is generated representing the thermally active part of the transducer. The thin metal layer possesses a small thermal mass and thus a low thermal inertia leading to a response time of a few microseconds. The sensor diameter of only 1.65 mm allows an integration in wind tunnel models with limited installation space. By polishing the transducer head together with the surrounded model surface the transducer can be perfectly fitted to the model surface. Furthermore, assuming a one dimensional heat flux into the transducer the surface heat flux can be derived as proposed by Schultz et al. [108] or Cook et al. [15].
In the present study the coaxial thermocouples were used to evaluate the mean surface heat flux on the model and thus the beginning and progress of the boundary layer transition process.

Schlieren Visualization and Deflectometry

The flow field visualization presented in this study is based on a schlieren technique which is sensitive to density gradients. It was first introduced by Toepler [121]. A comprehensive overview on the principle of schlieren visualization and common schlieren setups is provided in Settles [109]. In the present study a standard Z-type 2-mirror schlieren system with two oppositely-tilted, on-axis spherical mirrors is used for visualization. For image recording a Phantom™ v1210 camera was used at a frame rate of approximately 175 kHz, an exposure time of 4 μs and a resolution of 1280×48 pixels, [47]. The camera was driven by a Cavilux™ Smart visualization laser which served as monochromatic and incoherent light source with a wavelength of 640 nm, [62]. The pulse length of the laser was set to 20 ns to overcome motion blur.
The setup allows the visualization and freezing of the boundary layer and its structures. Furthermore, the high sampling rate allows the tracking of structures, such as second mode waves, along the cone surface.

Additionally, measurements using a schlieren deflectometry setup were performed. The technique was first employed in a basic form by Davis [18] and later improved by McIntyre and Settles [79]. Recent studies on instability waves in laminar boundary layers were conducted by VanDercreek et al. [125] and Hofferth et al. [44] both using a focusing schlieren setup. In the present study a non-focusing schlieren setup was used similar to the standard schlieren setup described above. In contrast to the standard setup, the light source

was replaced by a continuously operated blue LED. Furthermore, the camera was replaced by two optical fibers with a diameter of 200 μm which were mounted in the imaging plane. The fiber diameter corresponds to a probing diameter in the boundary layer of approximately 0.8 mm. The fiber locations correspond to two streamwise-separated points inside the boundary layer with an estimated positioning inaccuracy of 1 mm. The light received was transmitted to Thorlabs™ Avalanche APD120A photodetectors which provide a bandwidth of 50 MHz, [46].
Finally, the setup allows measuring density gradient fluctuations at two points in the flow field at very high bandwidth.

Further information on both visualization techniques including a discussion on the capabilities and limitations can be found in Laurence et al. [57, 59].

Signal Recording

All transducer signals were recorded using an Amotronics™ transient recorder. The sampling rate was chosen according to the type of transducer used. Thus, coaxial thermocouples were sampled at 1 MHz, fast response pressure transducers at 10 MHz and photodetector signals at 100 MHz. According to the frequency content of the signal cable length were minimized to avoid the attenuation of the high frequency components.

2.4 Calibration of HEG Free-Stream Conditions

The HEG free-stream conditions are determined applying a scheme which couples experimental data with CFD, [107, 37]. For each run the initial shock tube pressure, initial temperature and shock speed[3] are measured. The latter is obtained using a series of thermocouples along the shock tube. The reservoir pressure at the end of the shock tube is measured by two pressure transducers of the type *Kistler 6215*[4]. All measurements are used as input parameters of the 1D equilibrium solver STN[5], [55], applied to compute the gas properties in the nozzle reservoir after shock reflection, i.e. total temperature, T_0, total density, ρ_0, and total enthalpy, h_0. Since viscous interactions at the shock tube wall are not considered by STN the computed reservoir pressure is too high and therefore corrected by an isentropic expansion of the reservoir condition to the measured reservoir pressure.
In a next step the complete expansion process of the test gas at stagnation conditions through the hypersonic nozzle is computed using the DLR TAU code, [67, 95]. To verify the computational results measurements in the nozzle exit plane are conducted for comparison. Therefore, quantities in the nozzle exit plane such as Pitot pressure, static pressure and sphere stagnation wall heat flux are experimentally determined.

The present section addresses both, the computational and the experimental approach in detail.

2.4.1 Free-Stream Quantity Measurements

Free-stream quantities such as Pitot and static pressure as well as wall heat flux on a sphere together with the corresponding distributions along the nozzle exit plane are measured using a rake with a set of different probes as shown in figure A.2a. The rake allows to arrange the probes along two lines perpendicular to each other with a minimal spacing of 12 mm. The wall heat flux is derived using spherical probes equipped with type E thermocouples, placed in the stagnation point as shown in figure A.2b. The Pitot pressure probe, shown in figure A.2c, as well as the static pressure probe, provided with its basic dimensions in figure 2.9, were equipped with pressure transducer of the type *KULITE-XCEL-100*[6]. A rated pressure of 350 kPa for the Pitot pressure measurements and 35 kPa for static pressure measurements was chosen. The pressure distribution around

[3] alternatively main diaphragm burst pressure
[4] Kistler Instrumente AG, Eulachstrasse 22, 8408 Winterthur, Schweiz
[5] Shock tube and nozzle calculations for equilibrium air.
[6] Kulite Semiconductor Products, Inc., One Willow Tree Road, Leonia, NJ 07605, USA

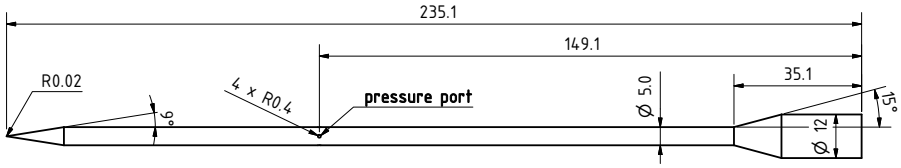

Figure 2.9: Dimensions of the cone-cylindrical probe used in HEG for static pressure measurements.

the static pressure probe is set by the conical shock developing at the probe tip followed by the expansion around the conical-cylindrical junction. At the pressure port, indicated in figure 2.9, the measured pressure is lower than the free-stream static pressure as depicted in figure 2.10. Therefore, the measured values have to be corrected. The correction factor is determined by means

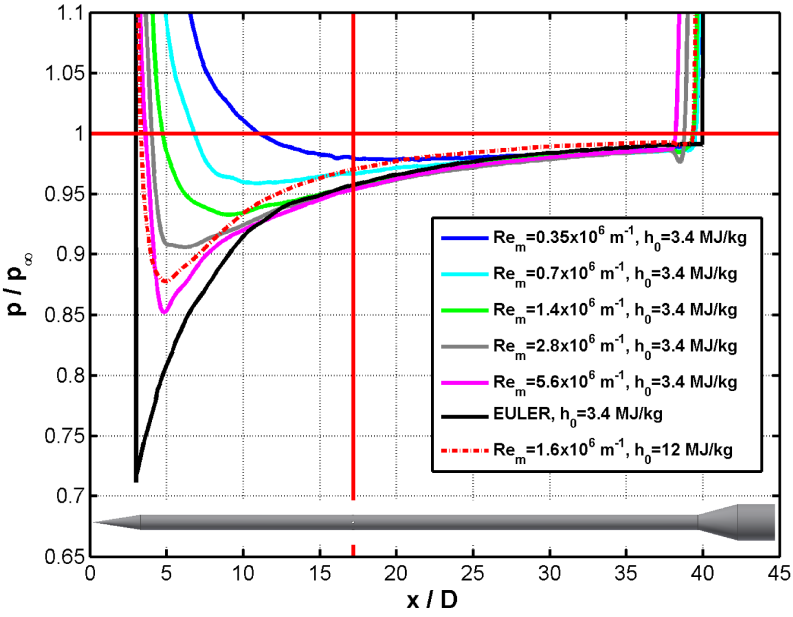

Figure 2.10: Static pressure distribution along the pressure probe depicted in figure 2.9 based on a numerical evaluation. The correction factors can be found along the vertical red line which indicates the location of the pressure taps. Reproduced and complemented from Karl [50].

of CFD computations using a two-dimensional axisymmetric computational domain. The computational grid was adapted to the flow and consisted of about 200,000 grid points. The probe walls were modeled using a no-slip boundary condition at a constant wall temperature of 300 K. The boundary layer was assumed to be laminar and the gas in chemical and thermal equilibrium.

2.4.2 Computational Verification

Computational Approach

The numerical approach is subdivided into two main steps. First, the expansion of the HEG test gas through the hypersonic nozzle is computed. The computational domain of the HEG Mach 8 nozzle which was used in the scope of this study is provided in figure 2.11. The free-stream quantities at

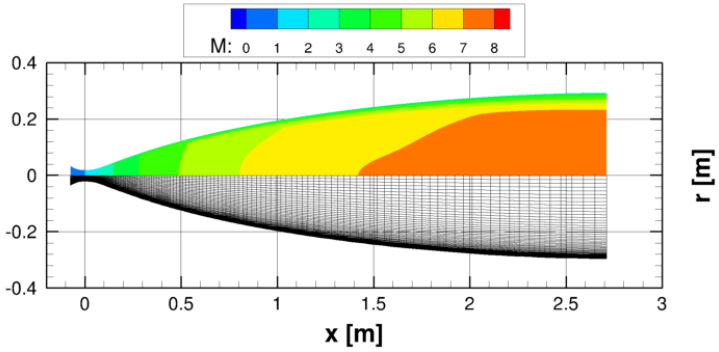

Figure 2.11: Mach number contour and grid of the computational domain of the HEG Mach 8 nozzle.

the nozzle exit are used to calculate the total pressure behind a strong shock which is subsequently compared to measured Pitot pressures. Since the specific heat ratio changes across the shock an effective specific heat ratio, γ_{eff}, has to be computed in a second step. This is done by using the before derived free-stream conditions to compute the flow field around a sphere which provides the stagnation pressure and the stagnation heat flux. The computational domain is shown in figure A.3. Subsequently, the stagnation quantities are used in combination with the Rayleigh-Pitot formula, [56], and the Verant correlation, [126], to derive the effective specific heat ratio and the factor for the Verant correlation. Both parameters allow to convert computed free-stream quantities to experimentally mensurable quantities for comparison.

Considering the computations of the nozzle flow field the nozzle wall is modeled using a no-slip condition with a constant temperature of 300 K. The computational grid consists of about 20,000 grid points. A detailed description of the computational approach is provided by Karl [50]. The nozzle boundary layer is assumed to be primarily turbulent, whereas the transition onset location is subject of the calibration and is addressed later in this section. Further, the Spalart-Allmaras turbulence model was applied and a gas at thermal equilibrium was considered which is addressed as well in the present section.

The computed free-stream conditions are compared to measurements in the nozzle exit plane, i.e. measuring the Pitot pressure, p_{t2}, the static pressure, p_{stat}, and the heat flux density in the stagnation point of a sphere $\dot{q}_{t2}$. The Pitot pressure based on the numerical solution is calculated using the Rayleigh-Pitot formular, [56]:

$$\frac{p_{t2}}{p_1} = \left[\frac{(\gamma+1)M_1^2}{2}\right]^{\frac{\gamma}{\gamma-1}} \left[\frac{\gamma+1}{2\gamma M_1^2-(\gamma-1)}\right]^{\frac{1}{\gamma-1}} \tag{2.1}$$

with p_1 being the static pressure upstream the shock. The above expression can be modified to be independent of the static pressure by using the following expressions for the speed of sound

$$a = \sqrt{\gamma RT}, \tag{2.2}$$

the Mach number

$$M = \frac{u}{a}, \tag{2.3}$$

and the perfect gas equation

$$p = \rho RT, \tag{2.4}$$

with u being the flow speed in axial direction, T the gas temperature, ρ the density of the gas and R the gas constant. From equation 2.2 to 2.4 the following expression for the static pressure is derived

$$p_1 = \frac{1}{\gamma M_1^2}\rho u^2 \tag{2.5}$$

which leads in combination with 2.1 to the following variation of the Rayleigh-Pitot formular:

$$p_{t2} = \left[\frac{1}{\gamma_{eff}M_1^2} \cdot \frac{\left(\frac{\gamma_{eff}+1}{2}M_1^2\right)^{\frac{\gamma_{eff}}{\gamma_{eff}-1}}}{\left(\frac{2\gamma_{eff}}{\gamma_{eff}+1}M_1^2-\frac{\gamma_{eff}-1}{\gamma_{eff}+1}\right)^{\frac{1}{\gamma_{eff}-1}}}\right] \cdot \rho u^2. \tag{2.6}$$

Equation 2.6 offers the advantage of a significantly lower sensitivity of the Pitot pressure to the ratio of specific heats as shown in Giese [31]. Hence, the error of p_{t2} due to uncertainties in γ_{eff} is strongly reduced. The strong shock upstream the blunt probe causes a strong temperature rise leading to a reduction of γ which is a function of temperature and pressure. Therefore, an effective specific heat ratio, γ_{eff}, which represents the compression over the strong shock has to be used in equation 2.6.

The calculation of the heat flux density at a sphere is conducted using the Verant correlation, [126]:

$$\dot{q}_{t2} = \sqrt{\frac{p_{t2}}{r_{sphere}}} \cdot K^{Verant} \left(\frac{h_0 - h_w}{R \cdot T_{ref}} \right)^{1.0688} \tag{2.7}$$

whereas r_{sphere} is the sphere radius with $\mathrm{r_{sphere}} = 10\,\mathrm{mm}$. The enthalpy at the wall is calculated with $h_w = c_p \cdot T_w$. R is the gas constant for air, $\mathrm{R} = 287\,\mathrm{J/kgK}$, at a reference temperature of $\mathrm{T_{ref}} = 273.15\,\mathrm{K}$. The original factor $K^{Verant} = 23.787$ was determined for chemically reacting high enthalpy shock layers and needs to be determined separately for the flow conditions used in this study. Therefore, both, γ_{eff} and K^{Verant}, are derived using equations 2.6 and 2.7 in combination with complementary CFD computations of a flow around a sphere. The inflow conditions for this computation correspond to the numerically determined free-stream conditions on the center line of the nozzle exit plane. For the sphere computations the wall is modeled using a no-slip condition with a constant temperature of 300 K. The computational grid consisted of about $5,300$ grid points. The sphere wall boundary layer is assumed to be fully laminar.

The Nozzle Boundary Layer State

An additional uncertainty which needs to be addressed is the state of the boundary layer along the nozzle wall and thus the boundary layer layer thickness. It changes the effective expansion ratio of the nozzle which in return directly affects the free-stream conditions at the nozzle exit. Figure 2.12 provides a comparison of measured Pitot pressure and static pressure distributions in the nozzle exit plane for various transition onset locations. The comparison is done for a unit Reynolds number of $\mathrm{Re_m} = 1.6 \cdot 10^6\,\mathrm{m^{-1}}$ which is the lowest unit Reynolds number used in the scope of this thesis. A good agreement of the Pitot pressure measurements and the static pressure measurements with CFD is obtained if a fully turbulent boundary layer is assumed as shown in figure 2.12. Thus, it is concluded that for higher unit Reynolds number conditions the

assumption of a fully turbulent boundary layer holds as well. Furthermore, the plot is provided in dimensional values showing a good run to run repeatability.

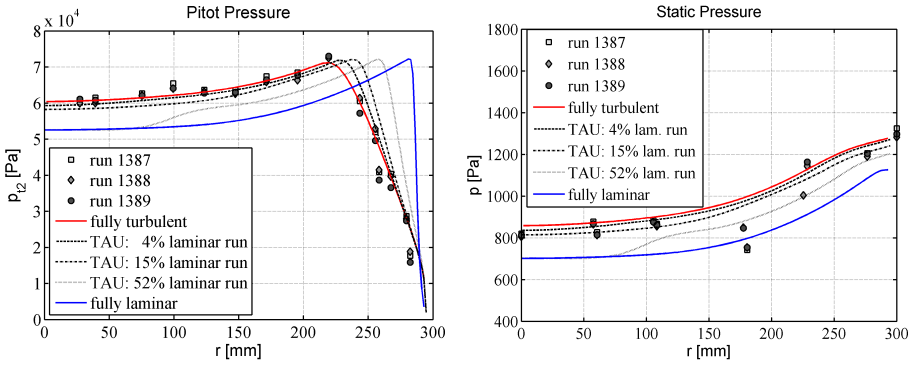

Figure 2.12: Effect of the transition onset location along the nozzle wall on the nozzle exit pressure distribution. $\mathrm{Re_m} = 1.6 \cdot 10^6\ \mathrm{m}^{-1}$.

Thermal State of the Test Gas

At stagnation temperatures around 2700 K high temperature effects such as vibrational excitation and dissociation of oxygen become important. To model the flow correctly the thermal state of the gas which is expanded through the nozzle has to be identified. Therefore, figure 2.13a provides normalized Pitot and static pressure distributions in combination with according CFD predictions. The CFD based pressure distributions are computed using the Spalart-Allmaras (SA) turbulence model with thermal equilibrium (EQ) and thermal non-equilibrium (NEQ). For the latter case the chemical reaction rates for air proposed by Gupta were used [35]. In principle a good agreement of the experimentally determined Pitot pressure, shown in 2.13a, and the stagnation heat flux, shown in figure 2.13b, with the corresponding CFD solutions is obtained. Both experimental quantities were normalized with the reservoir pressure, p_0, and the reference wall heat flux at reservoir conditions, $\dot{q}_{ref}$, respectively. The low sensitivity of the two quantities does not allow to distinguish between both thermodynamic states. In contrast the static pressure shows a high sensitivity to the thermodynamic states. Figure 2.13a also provides the normalized static pressure distribution. It is found to be in good agreement with the thermal equilibrium solution. Hence, it is concluded that the assumption of thermal equilibrium gas holds for the low enthalpy test conditions investigated in this study.

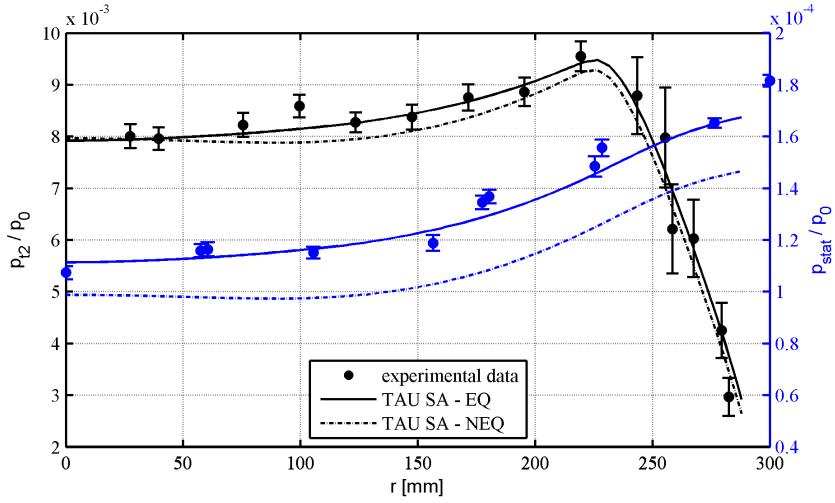

(a) Normalized Pitot pressure and static pressure.

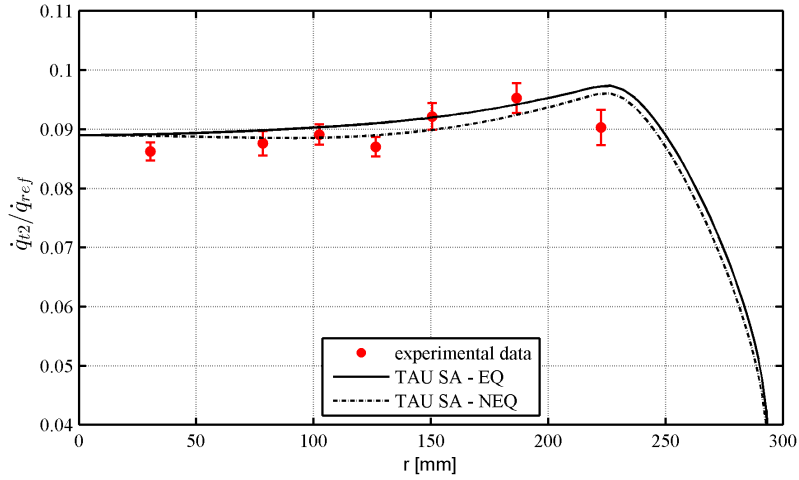

(b) Normalized stagnation heat flux density.

Figure 2.13: Pitot pressure p_{t2}, static pressure p_{stat} and heat flux $\dot{q}_{t2}$ along the radius in the nozzle exit plane compared to TAU computations with thermal equilibrium (EQ) and thermal non-equilibrium (NEQ), $\mathrm{Re_m} = 4.0 \cdot 10^6\ \mathrm{m}^{-1}$.

Due to the good agreement between the computations and the experimental data all subsequent nozzle computations for enthalpies around $h_0 = 3.4$ MJ/kg are conducted assuming a fully turbulent nozzle boundary layer and a flow at thermal equilibrium the latter being in agreement with Hannemann at al. [37].

2.4.3 Validation

In the scope of a specific calibration campaign the above described procedure was applied to a wide range of HEG test conditions relevant to this study. The comparison between the experimentally obtained free-stream quantities and the corresponding computational results is provided in figures 2.14, 2.15a and 2.15b. All CFD based free-stream quantities are in good agreement with the experimentally obtained results.
Thus, the applied procedure is shown to be valid in the investigated range. All subsequently presented free-stream conditions are derived following this approach. An overview on the HEG test conditions used in the frame of this study is provided in table A.2.

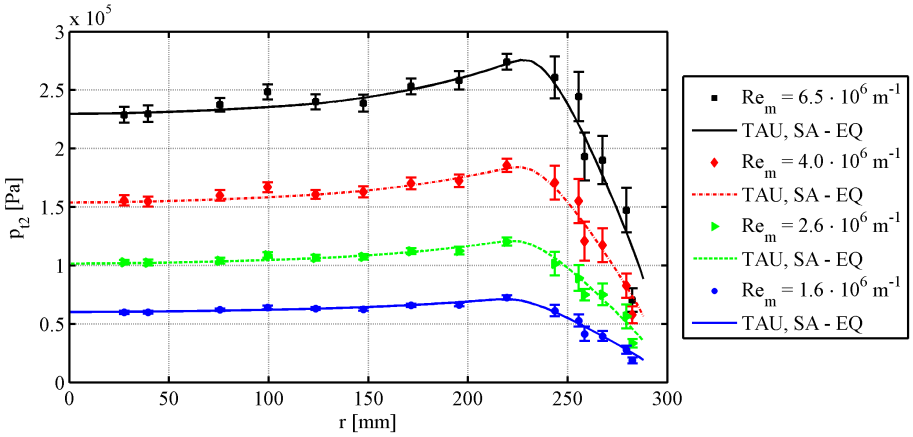

Figure 2.14: Pitot pressure p_{t2}, radial distribution in the nozzle exit plane obtained by experiments and computation.

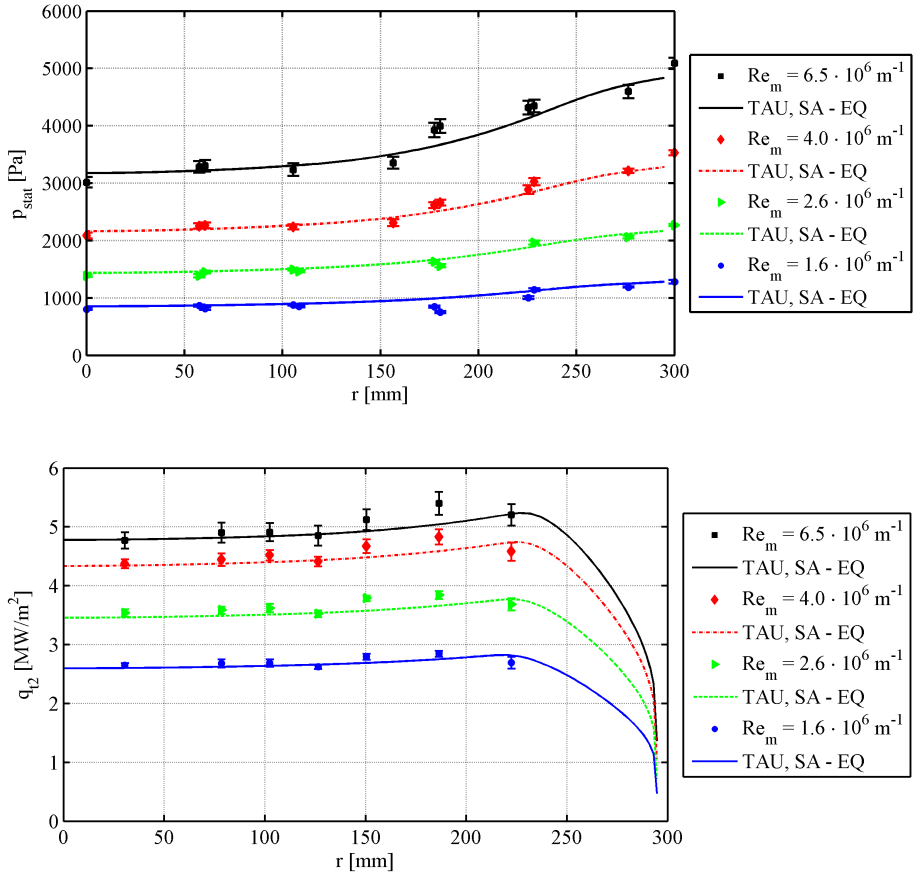

Figure 2.15: Static pressure p_{stat} (top) and stagnation heat flux q_{t2} on a sphere (bottom), radial distribution in the nozzle exit plane obtained by experiments and computation.

Chapter 3

Ultrasonically Absorptive Carbon-Carbon

The purpose of the present section is to provide all necessary information on the applied carbon-carbon ceramic (C/C) to understand the interaction between the porous material and the flow field. Therefore, the manufacturing procedure and basic mechanical properties are presented in section 3.1. In the following section 3.2 the pore filling time is estimated to verify the use of C/C in an impulse facility with short test times such as HEG. Furthermore, the acoustic properties of the material in the ultrasonic range are assessed theoretically and experimentally, section 3.3 and 3.4. The latter section provides detailed information on the test rig which was designed and realized to experimentally determine the absorption coefficient of C/C.

C/C is manufactured by the Institute of Structures and Design at DLR Stuttgart and was provided for wind tunnel testing in the frame of the DLR project IMENS-3C[1].

The results presented in the sections 3.1, 3.3 and 3.4 are based on the joint publication of Wagner et al. [132, 129].

[1] Integrated Multidisciplinary Design of Spacecraft Structures

3.1 Manufacturing and Basic Properties

Carbon fiber reinforced carbon ceramic (C/C) represents an intermediate state obtained during the C/C-SiC manufacturing process, [41, 42]. In order to reach this state the following steps are conducted: By means of an autoclave technique, a green body of carbon fiber reinforced plastic (CFRP) is formed using commercially available 0|90° carbon fibre fabrics impregnated with a phenolic resin. After curing, the green body is pyrolysed at temperatures of up to

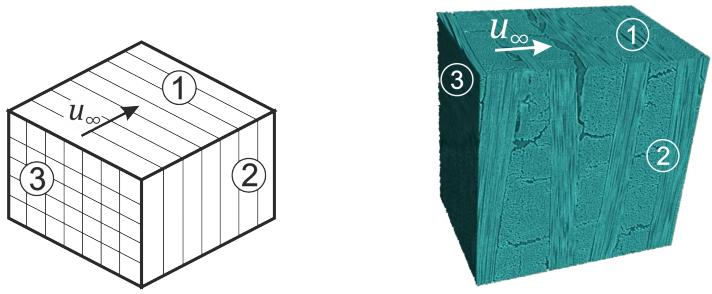

Figure 3.1: Schematic (left) and computer tomography (right) picture of the applied C/C material.

1650 °C, which converts the phenolic matrix to amorphous carbon. This results in a C/C body containing random patterns of micro cracks as depicted in figure A.5. Carbon fiber reinforced carbon offers low thermal expansion and specific weight as well as high temperature stability in absence of oxygen. Its structure can be very well reproduced during the manufacturing process and has already been applied widely for e.g. coated leading edges of hypersonic vehicles, [33, 34], and transpiration cooled combustion chamber applications, [36, 85].

The manufacturing of the type of C/C material applied here is based on stacking 0|90° carbon fiber fabrics. Hence, the material exhibits an orthotropic layout, as depicted in figure 3.1. This is associated with a different thermo-mechanical behavior in longitudinal (1,2) and transverse (3) direction with respect to the carbon fiber fabrics. The computer tomography picture shows the resulting micro crack system with a random distribution. The symbol ∞ indicates the free stream direction during the wind tunnel tests relative to the C/C material. In total, seven plates of C/C material were manufactured and used for the ceramic insert. For each plate, the open porosity and the raw density were determined by a gravimetric analysis according to *DIN EN 993-1*. This results in an averaged open porosity of 14.98 ± 0.24 % and density of 1.3304 ± 0.0031 g/cm^3,

as shown in figure 3.2. In order to get a better understanding of the occurring

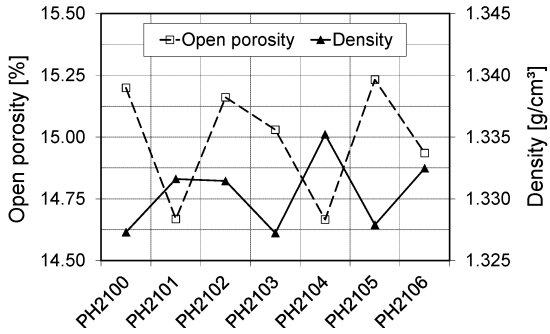

Figure 3.2: Measured density and porosity of manufactured C/C plates used for model insert. (averaged open porosity 14.98 ± 0.24 %)

pore geometries, the pore size distribution of the applied C/C material was determined by means of mercury intrusion porosimetry. Therefore, a sample was placed into a sample cell, which was evacuated. Non-wetting mercury was inserted and pressure was applied to force the mercury to penetrate the sample. At lower pressures, only bigger pores of the material were filled, whereas at higher pressures, smaller pores were intruded. A maximum pressure of up to 200 MPa was applied leading to a fully mercury intruded material. The relation between the applied pressure p and the volume of mercury intruded into the sample is recorded. By means of the Washburn equation the applied pressure can be correlated to the pore diameters D, [141]:

$$D = -\frac{4\gamma \cos\theta}{p} \tag{3.1}$$

with γ and θ being the mercury surface tension and contact angle, respectively. Hence, the pore size distribution as a function of pore volumes and pore diameters can be derived. The pore size distribution was determined in the pore diameter range $0.01 - 100$ µm, pore sizes beyond that range cannot be detected with the facility used. Figure 3.4 and 3.3 show histograms of the pore size distributions. The relative pore volume characterizes the volume of defined pore diameter ranges with respect to the total volume of mercury intruded into the C/C sample. Furthermore, the corresponding derivative $dV/dlog(D)$ of intruded pore volume with respect to the logarithm of the pore diameter is shown. The plots show the measured pore size distribution for two out of four samples, taken from four different C/C plates. This allows to determine peak and median pore diameters, ranging between 28-30 µm and 11-14 µm, respectively. All samples show a similar and comparable distribution. It can be stated, that there is no

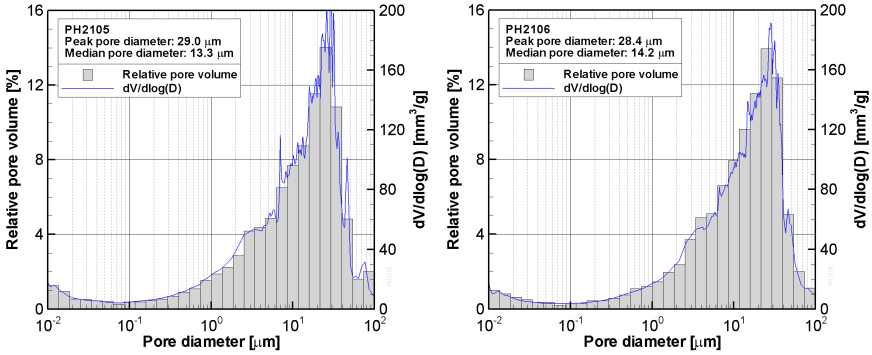

(a) PH2105 (b) PH2106

Figure 3.3: C/C pore size distributions of sample PH2105 and PH2106.

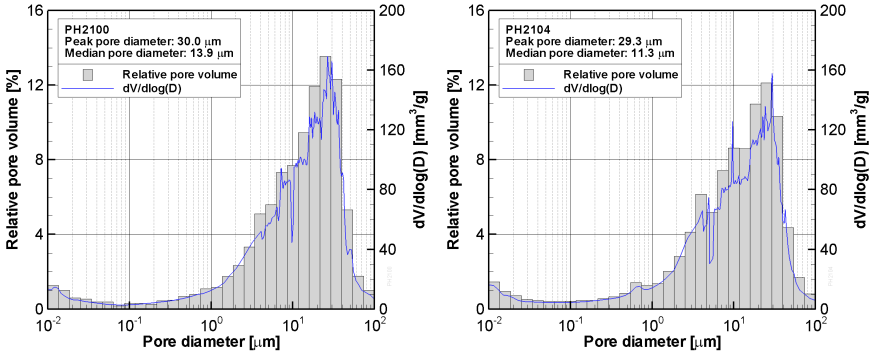

(a) PH2100 (b) PH2104

Figure 3.4: C/C pore size distributions of sample PH2100 and PH2104.

single dominant pore diameter, but rather a distinctive pore system for pore diameters between approximately 1 µm and 100 µm. Pores mainly occur in the matrix, whereas bigger pore diameters are related to microcracks which result from the shrinking of the matrix during the manufacturing process.

3.2 Pore Filling Time

Before a test in HEG the test section containing the wind tunnel model is evacuated. Therefore, the pores of the C/C ceramic do practically not contain any medium to transport sound waves. To make sure the porous surface is effective during a test time of a few milliseconds, an estimate of the required pore filling time is subsequently derived based on the pore geometry introduces in figure 3.5.

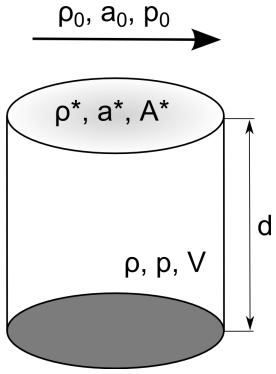

Figure 3.5: Pore geometry.

The chosen approach follows a procedure proposed by Hornung [45] to estimate the response time of pressure transducers in cylindrical pressure taps. The analytical approach assumes a cylindrical pore shape, an uniform distribution of the gas in the volume and neglects viscous effects. However, the pore shape of the C/C material resembles more a slit like shape which makes the viscous effects more important compared to circular shapes. The viscous effects will probably cause higher pore filling times due to an effectively smaller pore opening.

The pore filling process can be divided into two stages. During the first stage the pressure difference between the pressure in the pore volume and the ambient pressure is sufficiently high to assume the flow at the pore entrance to be choked. With increasing pressure inside the pores the choked flow breaks down and the flow field becomes subsonic. The limit between the two stages is reached when

$$p > p_0 \left(1 + \frac{\gamma - 1}{2} M^2\right)^{-\frac{\gamma}{\gamma - 1}}. \tag{3.2}$$

For a gas with $\gamma = 1.4$ and $M = 1$ the critical pressure ratio is $p/p_0 = 0.528$.

3.2.1 Choked Flow

Figure 3.5 provides a schematic view of a cylindrical pore with ρ^*, A^* and a^* being the density, the pore cross section area and the speed of sound in the pore entrance surface. Assuming the flow into the pore volume, V, being initially

choked the mass flow rate into the pore is

$$\frac{dm}{dt} = V\frac{d\rho}{dt} = \rho^* a^* A^*. \tag{3.3}$$

with ρ being the gas density inside the volume. Further, assuming the flow to be isentropic the mass flow rate

$$\rho^* a^* A^* = \rho_0 a_0 A_0 \tag{3.4}$$

can be rewritten as

$$\frac{\rho^* a^*}{\rho_0 a_0} = \frac{A_0}{A^*} = (1 + \frac{\gamma - 1}{2} M^2)^{-\frac{1}{\gamma - 1}} (1 + \frac{\gamma - 1}{2} M^2)^{-\frac{1}{2}}. \tag{3.5}$$

For choked flow the local Mach number in the throat is $M = 1$. Thus, equation 3.5 can be simplified. In combination with equation 3.3 the following expression is obtained:

$$\frac{d\rho}{dt} = \rho_0 \; a_0 \; \frac{A^*}{V} \left(\frac{2}{\gamma + 1} \right)^{\frac{\gamma+1}{2(\gamma-1)}}. \tag{3.6}$$

At this point it is assumed that the thermodynamic process of the gas being processed through the pore throat to a uniform state in the pore volume is isentropic. Although, this assumption is certainly not fully correct, the assumption is expected to provide an acceptable approximation of the process. Thus, using the isentropic pressure-density relation

$$\frac{p}{\rho^\gamma} = constant = \frac{p_0}{\rho_0^\gamma} \tag{3.7}$$

and differentiating the expression yielding

$$\frac{dp}{p} = \gamma \frac{d\rho}{\rho} \tag{3.8}$$

equation 3.7 and 3.8 can subsequently be used in equation 3.6 which leads to

$$\frac{dp}{p} = \left(\frac{2}{\gamma + 1} \right)^{\frac{\gamma+1}{2(\gamma-1)}} \; \frac{\rho_0}{\rho} \; \frac{\gamma \; a_0 \; A^*}{V} \; dt. \tag{3.9}$$

The integration of 3.9 provides the following expression:

$$\left(\frac{p}{p_0} \right)^{\frac{1}{\gamma}} = \left(\frac{2}{\gamma + 1} \right)^{\frac{\gamma+1}{2(\gamma-1)}} \; \frac{a_0 \; A^*}{V} \; t. \tag{3.10}$$

This expression can be used to estimate the time required to fill a pore volume, V, with a gas, described by γ and a_0, till a pore pressure p. The pressure which drives the pore filing process is denoted as p_0. The ratio A^*/V can be written as the pore depth, d. In the present study the pore depth equals the thickness of the material assuming the volumetric porosity, reported in section 3, being identical to the surface porosity which is likely true for the plane of interest, i.e. plane 1 and 2 in figure 3.1 (left).

3.2.2 Subsonic Flow

At the time t_c the pressure in the pore exceeds the critical pressure, p_c, given in equation 3.2. The flow through the pore entrance is no longer chocked and becomes subsonic. In this case the pressure rate of change is assumed to be inversely proportional to the pore depth and directly proportional to the pressure difference, the speed of sound and a constant, c_1. This approach neglects compressibility effects which are certainly still present. As a consequence the estimated time to fill a pore will be slightly too small. The following empirical approach is chosen, [45]:

$$\frac{dp}{dt} = c_1 \, \frac{a_0}{d} \, (p_0 - p). \tag{3.11}$$

To estimate the pressure in the pore over time c_1 needs to be determined. This has to be done such that the pressure and the pressure rate of change at the time the choked flow breaks downs are met. The pressure ratio at breakdown is known to be

$$\frac{p_c}{p_0} = \left(\frac{2}{\gamma + 1} \right)^{\frac{\gamma}{\gamma - 1}}. \tag{3.12}$$

The critical time is derived using equation 3.12 and equation 3.10:

$$t_c = \sqrt{\frac{\gamma + 1}{2}} \, \frac{d}{a_0} \tag{3.13}$$

The constant c_1 is obtained by first using equation 3.9 to assess the derivative dp/dt at the critical pressure ratio given in equation 3.12. The result is used in equation 3.11 yielding the constant c_1:

$$c_1 = \gamma \, \frac{\left(\frac{2}{\gamma+1} \right)^{\frac{3\gamma-1}{2(\gamma-1)}}}{1 - \left(\frac{2}{\gamma+1} \right)^{\frac{\gamma}{\gamma-1}}} \tag{3.14}$$

which is $c = 1.431$ for $\gamma = 1.4$.

Further equation 3.11 can be written as

$$\frac{dp}{(p_0 - p)} = c_1 \, \frac{a_0}{d} \, dt \tag{3.15}$$

and integrated to

$$p = p_0 - e^{c_2} \, e^{\frac{-c_1 \, a_0}{d} \, t} \tag{3.16}$$

where e^{c_2} contains the integration constant and is simplified to $c_3 = e^{c_2}$. Using the boundary condition given in equation 3.12 the constant can be determined to

$$c_3 = (p_c - p_0)\, e^{c_1 \frac{a_0}{d} t_c} \tag{3.17}$$

with t_c being the time at which the critical pressure, p_c, is reached. By substituting equation 3.17 into equation 3.16 the following expression is obtained providing the pore pressure as function of time for the subsonic filling process

$$\frac{p}{p_0} = 1 - \left(1 - \frac{p_c}{p_0}\right)\, e^{-c_1 \frac{a_0}{d}\,(t - t_c)}. \tag{3.18}$$

3.2.3 Pore Filling Times at HEG Test Conditions

Figure 3.6 provides the normalized pressure, p/p_0, for both the choked and the subsonic pore filling process for various γ. The non-dimensional parameter $a_0/d \cdot t$ and the variation of γ allows to account for different types of gas, pore depths and varying speed of sound or gas temperature, respectively. In figure 3.6, $a_0/d \cdot t$ is provided for $p/p_0 = 0.95$ and various γ. To determine

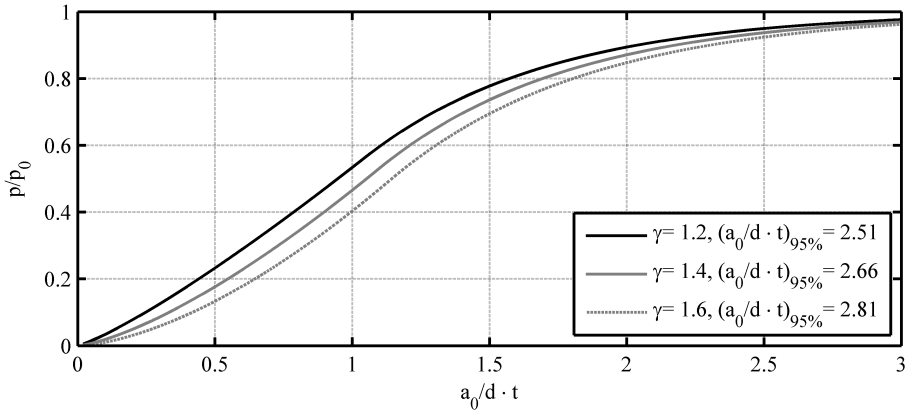

Figure 3.6: Estimated pore pressure as function of time, speed of sound and pore depth.

the pore filling time for the test conditions used in the scope of the study the above parameters need to be assessed. The pore depth varies in the range of $5 < \mathrm{d} < 17$ mm, section 2.3.1. The model surface is at room temperature before each test. Due to the short test times in HEG no significant change in surface

temperature is expected during the run.[2] By means of a TAU computation of the flow field around the model a representative peak temperature inside the boundary layer of 850 K was obtained. Thus, the gas entering the pore volume is expected to have a temperature in the range of $300 < \mathrm{T} < 850$ K which corresponds to $1.35 < \gamma < 1.4$ for air. By varying the relevant parameters in the most optimistic and the most conservative way, the time required to reach $p/p_0 = 0.95$ in a pore of 17 mm depth is estimated to be in the range of $0.08 < \mathrm{t} < 0.13$ ms. The time typically needed to establish a constant flow field around the cone is in the order of 1 ms, see, e.g., figure 4.6 for the first appearance of second mode instabilities. Thus, the pressure inside the pores is expected to be settled well before the test time starts.

In addition, figure 3.7 provides the parameter $(a_0/d \cdot t)_{95\%}$ for a wider range of γ which are of interest for tests in HEG.

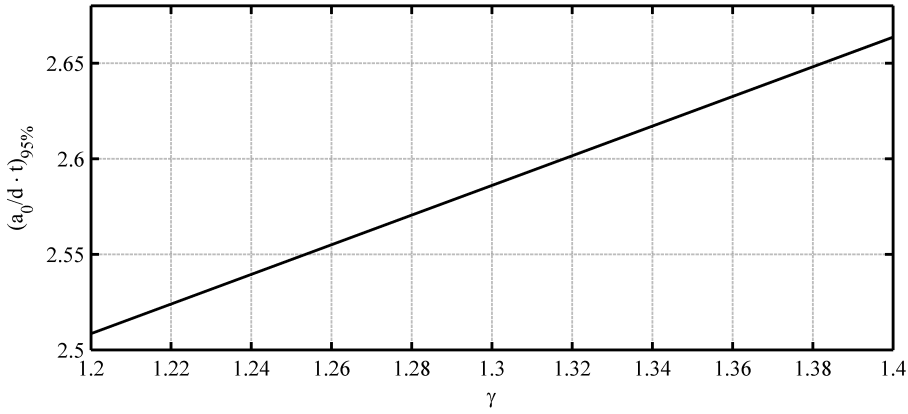

Figure 3.7: Non-dimensional pore filling time for a range of γ relevant for use in HEG.

[2]The surface temperature rise on C/C was estimated to be below 20 K at test time end assuming a fully turbulent boundary layer and $\mathrm{Re_m} = 6.8 \cdot 10^6$ m^{-1}.

3.3 Absorber Properties - Theory

Sound waves are mechanical oscillations of an elastic medium which propagate through gases, fluids or solids. A sound wave propagating in air forms a wave which superimposes pressure fluctuations in the order of $p_{rms} = 2 \cdot 10^{-5}$ Pa (hearing threshold level) and $p_{rms} = 200$ Pa (acoustic pain threshold) on the ambient pressure. Sound waves in gases and liquids are transmitted as longitudinal waves, i.e. the oscillating direction is identical with the propagation direction.
The acoustic characterization of materials typically used to absorb sound waves, e.g. to optimize the acoustic properties of lecture or concert halls, follows well established procedures as described e.g. in the norm EN ISO 10534[3]. These procedures were established for a frequency range between 16 Hz and 16 kHz, i.e. the range in which the human ear is sensitive to sound waves. A common test rig used in this scope is the Kundt's tube which presents a simple method to characterize reflecting and absorbing setups with perpendicular sound incidence.

In the present study the frequency range of interest is between 100 kHz and 500 kHz. The corresponding wavelength in air at ambient temperature is in the range of 3.4 mm to 0.68 mm. However, the application of a Kundt's tube requires the tube diameter to be significantly smaller than the wavelength. For obvious practical reasons this constraint prevents the application of the above described approach. Therefore, an alternative approach used by Tsyryulnikov et al. [122] and Fedorov [25] to determine the acoustic properties in the relevant frequency range is followed. This implies the set up of a new test rig. The test rig, the test procedure and the applied absorber theory are described in the present section.

The realization of direct absorption property measurements on porous materials at high frequencies and low air densities is challenging. It implies several practical and physical difficulties which need to be resolved for a successful measurement. The problems encountered throughout the subsequently presented experiments were found to be thoroughly summarized by Tsyryulnikov et al. [122]. The following practical and physical difficulties were identified:

- "high damping degree of acoustic waves in the free medium (especially at low densities of the medium), which increases with increasing frequency;
- decreased efficiency of audio transmission from the acoustic source to the medium because of impedance mismatch at low density of the medium;

[3]EN ISO 10534: Acoustics – Determination of sound absorption coefficient and impedance in impedance tubes

- variation in the level of sound generation by the acoustic source caused by the acoustic wave reflected by the coating under study and arriving at the source position;
- frequency limitations of sound-generating and sound-registering devices".

3.3.1 Homogeneous Absorber Theory

The absorption characteristics of a porous material can be described by the loss of acoustic power which is experienced by an acoustic wave traveling inside a porous material. In general, the power transmitted through a surface A is defined by

$$P = \int \vec{I}\, d\vec{A} \tag{3.19}$$

with $\vec{I}$ being the intensity, which is a vector pointing in the direction of wave propagation. Assuming the acoustic pressure, p, and the acoustic particle velocity, ν, being in phase with $p = \rho a \nu$, which is the case for plane waves, the intensity can be formulated with experimentally measurable values $I = p^2/(\rho a)$, with a being the speed of sound and ρ the density. The acoustic power loss:

$$\beta = P_\beta / P_+ \tag{3.20}$$

is defined as the ratio between the absorbed acoustic power, P_β, and the total acoustic power reaching the surface, P_+. For absorber materials of finite thickness and acoustically hard end the acoustic power is not transmitted through but absorbed inside the material and reflected. Therefore, P_β describes the loss of acoustic power due to the dissipative processes caused by viscosity and heat conduction inside the sample pores, [5]. Under these conditions the acoustic properties of a porous sample can be characterized by experimentally determining the reflection coefficient, R, which for a plane wave is defined as

$$R^2 = \frac{P_-}{P_+} \tag{3.21}$$

where P_- is the reflected acoustic power. Using the law of conservation of energy $P_+ = P_\beta + P_-$ and the definition of β, provided above, the relation between the reflection coefficient and the absorption coefficient yields

$$\beta = 1 - R^2. \tag{3.22}$$

To theoretically assess the absorption characteristics of a material the wall complex impedance at the absorber surface needs to be determined. The wall impedance describes the ability of the absorber material to interact with its

acoustic environment. In general, the impedance at the wall is defined as $z = p(0)/\nu(0)$. The absorption coefficient is related to the wall impedance by

$$\beta = \frac{4Re(\frac{z}{\rho a})}{\left[Re(\frac{z}{\rho a}) + 1\right]^2 + \left[Im(\frac{z}{\rho a})\right]^2}. \tag{3.23}$$

From equation 3.23 it follows that if the wall impedance is adjusted to $z = \rho a$ the absorption coefficient reaches its maximum. Further, it follows that the absorber properties can be optimized by realizing $Im(z) = 0$. The wall impedance of an homogeneous porous absorber of infinite thickness, z_∞, is given by Moser [83]:

$$z_\infty = \rho a \frac{\sqrt{\kappa}}{\sigma} \sqrt{1 - j\frac{\Xi\sigma}{\omega\rho\kappa}} \tag{3.24}$$

with $\omega = 2\pi f$ and Ξ the length specific flow resistance. The porosity σ ($\sigma \leq 1$) provides the ratio between the open pore volume inside the absorber and the total absorber volume. The structure coefficient κ ($\kappa \geq 1$) describes the pore structure in an indirect approximate way. All parameters are addressed in detail in section 3.3.2. Equation 3.24 can be rewritten in the following form to contain the breaking frequency, $\omega_k = \Xi\,\sigma/(\rho\kappa)$:

$$z_\infty = \rho a \frac{\sqrt{\kappa}}{\sigma} \sqrt{1 - j\frac{\omega_k}{\omega}}. \tag{3.25}$$

The breaking frequency is an important parameter to evaluate the suitability of a material to absorb acoustic waves. In general, at frequencies above the breaking frequency a good absorption characteristic is expected. At frequencies below ω_k the material is expected to have a low absorption capability. Further, it follows that the breaking frequency is proportional to the length specific flow resistance and the porosity.

For an absorber of finite thickness d with an acoustically hard end the wall impedance for frequencies, satisfying $|k_a d| >> 1$, becomes:

$$z = z_\infty \frac{1 + e^{-j2k_a d}}{1 - e^{-j2k_a d}}. \tag{3.26}$$

The complex absorber wave number k_a is defined as, [83]:

$$k_a = k\sqrt{\kappa}\sqrt{1 - j\frac{\omega_k}{\omega}} \tag{3.27}$$

with $k = \omega/c$ being the wave number with the phase speed c and angular frequency ω. Assuming a purely locally effective absorber, which is the case for

separated cavities inside the material preventing compensation effects in the surface parallel direction, the sound wave incidence angle, θ, measured towards the surface normal, has to be considered. According to Moser [83] this is done by adjusting the wall impedance to:

$$z = z_\infty \, cos\theta \, \frac{1 + e^{-j2k_a d}}{1 - e^{-j2k_a d}}. \tag{3.28}$$

The introduced angular dependency of the wall impedance does take into account possible effects of diffraction and sound interference caused by the porous surface micro-structure.

3.3.2 C/C Absorption Characteristics

Based on the theory presented in section 3.3.1 the used porous C/C material can be classified as an acoustic absorber. It follows from section 3.3.1 that the efficiency of an absorber depends on the following parameters:

- porosity σ
- length specific flow resistivity Ξ
- structure factor κ
- tortuosity τ.

Subsequently, the four geometrical parameters are assessed for C/C. Furthermore, the general absorber efficiency and the effect of pore depth are discussed. Ultimately, based on the introduced theory, the expected absorption coefficient is derived.

Porosity

The volume porosity σ describes the ratio between the accessible pore volume of the absorber and the total absorber volume. By means of mercury intrusion porosimetry the averaged open porosity of the material batch was measured to be 14.98 ± 0.24 %, see section 3.1.

Length Specific Flow Resistivity

A flow through a porous material experiences a resistivity r_s depending on the pressure difference across the material and the flow velocity. The relation

between pressure loss across the porous material and resistivity is provided by:

$$p_1 - p_2 = r_s U = \Xi \, d \, U \tag{3.29}$$

with p_1 and p_2 denoting the pressure upstream and downstream of the absorber and U being the velocity at the interface between absorber and flow field. Thus, Ξ is defined as $\Xi = r_s/d$ with d being the material depth. The length specific flow resistance was determined by an external company following DIN EN 29053. Four test samples were prepared, taken from the material batch used for wind tunnel model 2, section 2.3.1. Table 3.1 provides the results of the measurements and the corresponding standard deviation, *std*. It can be seen

sample number	Ξ [MPa · s/m^2]	$2 \cdot std$
1	11.5	0.16
2	13.4	0.18
3	13.6	0.14
4	14.5	0.10
mean	**13.3**	**-**

Table 3.1: Length specific flow resistivity and standard deviation based on DIN EN 29053.

that the results vary in the range of -14 % and $+9$ % around a mean specific flow resistivity of $\Xi = 13.3$ MPa s/m^2. This introduces an uncertainty in the reflection coefficient of less than 1 %.

Structure Factor

The structure factor κ plays an important role for porous materials with random micro structure. The parameter describes the nature of the pore pathway inside the material in an indirect approximate way. It cannot be measured or calculated directly for randomly structured porous materials. Instead it is derived from the acoustic performance of the absorber, see also section 3.4.2. To get a first estimate the factor is often set to unity providing good results for many practically relevant materials. A structure factor of $\kappa = 1$ implies that the total pore volume is equally involved in the absorption process. However, most of the porous absorber materials with random micro structure have pore structures which do not extend over the full material depth. Further, pores extending lateral to the propagation direction of the sound waves are expected. The fluid in these structures cannot be accelerated by the acoustic pressure to the same extend as in the case of a straight pore. Thus, the acoustic particle velocity which enters through the porous absorber surface is not propagated further into

the material. Additionally, only accelerated fluids dissipate energy by means of viscous interaction inside the porous material. It follows that the structure factor could be interpreted as the ratio between the totally accessible pore volume $V_{accessible} = \sigma \cdot V_{absorber}$ and the pore volume which can be accelerated by the acoustic pressure, $V_{accelerated}$.

$$\kappa = \frac{V_{accessible}}{V_{accelerated}} \geq 1. \tag{3.30}$$

In literature, structure factors of porous materials with random micro structure have been reported in a range of $2 \leq \kappa < 20$, for instance by Alber [4]. All following absorber properties were estimated assuming a structure factor of $\kappa = 8$, see also section 3.4.2.

Tortuosity

The tortuosity τ in general describes the torsion and the windings of a pore channel. According to Carman [13] it can be described as the ratio between the effective length l_{eff} of the oscillating fluid volume and the minimal length l_{min} of the pore channel, i.e. in most cases the material thickness d.

$$\tau = \frac{l_{eff}}{l_{min}} \geq 1. \tag{3.31}$$

A number of acoustic absorber theories use the tortuosity instead of the structure factor to describe the pore structure inside the material. However, the tortuosity was not used in the absorber theory applied within this study.

Absorber Efficiency

Using the material properties described above, the breaking frequency, ω_k, can be calculated. This frequency provides a first indication whether a porous material is an effective absorber or not. Figure 3.8 shows the ratio of three representative sound wave angular frequencies, ω, to the breaking frequency of the material. According to the absorber theory the material is expected to perform as an effective absorber if $\omega/\omega_k \geq 1$. As shown in figure 3.8 this is the case for all shown frequencies above an ambient pressure of $0.2 \cdot 10^5$ Pa. Hence, above the pressure level C/C is expected to have a damping effect on ultrasonic sound waves. However, the damping efficiency decreases with decreasing ambient pressure. Furthermore, figure 3.8 provides the dimensional frequency f_k which has to be exceeded to obtain an efficient absorber. It reveals that towards lower pressure levels only acoustic waves at high frequency are efficiently damped. The trend strongly increases towards very low pressures.

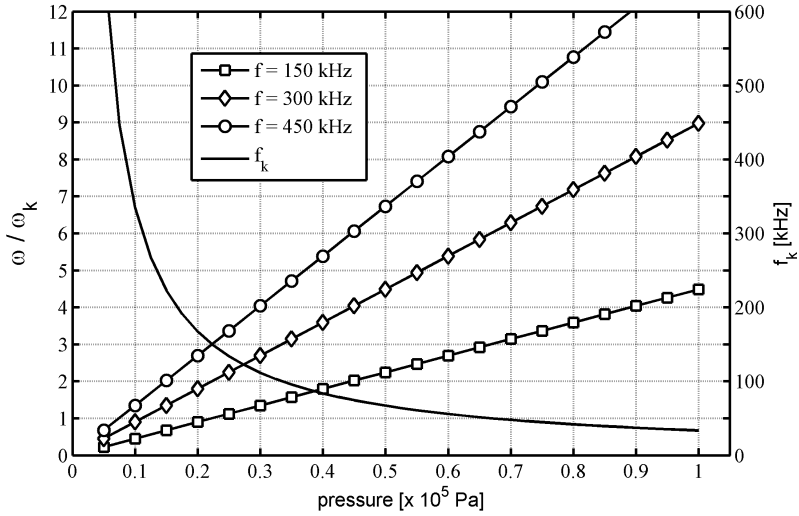

Figure 3.8: Angular frequency to breaking frequency for a representative disturbance frequencies range and representative material properties. The absorber is considered effective if $\omega/\omega_k \geq 1$.

Although, the C/C properties are not optimized the porous material will have a damping effect on the second mode instabilities. The absorber efficiency could be increased by lowering the breaking frequency which is achieved by e.g. lowering the length specific flow resistance.

Effect of Depth

Previous studies with ultrasonically absorptive coating using regularly spaced blind holes showed an effect of the material depth on the damping of second mode frequencies, [26, 64, 138, 12]. In the case of homogeneous porous absorbers the effect of material depth can be assessed by evaluating the resistivity $\Xi d/(\rho a)$. Figure 3.9 provides the absorption coefficient, β, as function of the sound wave frequency. The resistivity $\Xi d/(\rho a)$ was chosen in a representative range with respect to the conditions investigated in this study. In the bench tests the resistivity varied in the range of $170 \leq \Xi d/(\rho a) \leq 22000$. It can be seen in figure 3.9 that all curves collapse on each other. From theory it can be concluded that for the frequency range of relevance, $50\,kHz \leq f \leq 500\,kHz$, and for a resistivity of $\Xi d/(\rho a) \geq 100$ the material depth does not effect the absorption coefficient, anymore.

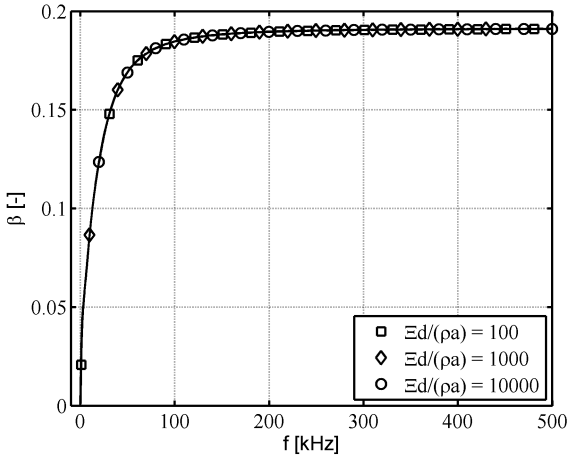

Figure 3.9: Estimated absorption coefficient β for varying resistivity, $\Xi d/(\rho a)$.

Absorption Coefficient

Based on the absorber theory the estimated absorption coefficient β of the C/C material considered here is provided in figure 3.10. The coefficient was

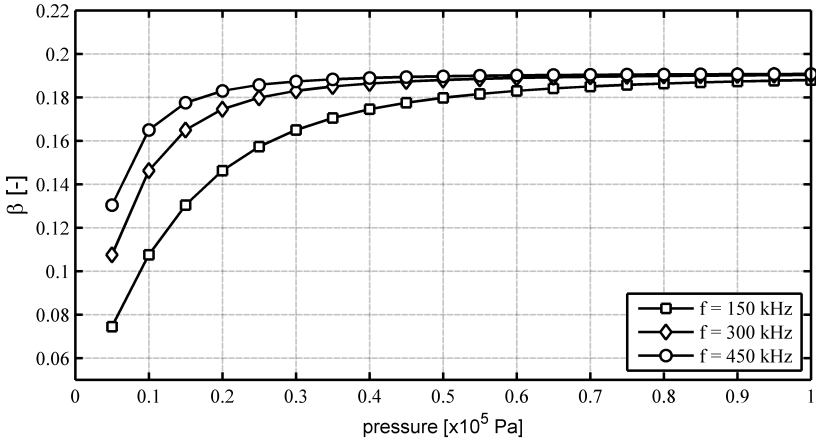

Figure 3.10: Estimated absorption coefficient of considered C/C material.

calculated for a frequency of 150 kHz, 300 kHz and 450 kHz considering the sound wave angle of incidence to be $\theta = 0°$. It can be seen that up to 19 % of the acoustic power transmitted towards the porous C/C material is expected to be absorbed depending on the ambient pressure and frequency.

3.4 Absorber Properties - Experiment

3.4.1 Test Rig

The test rig was designed to transmit ultrasonic wave packages of discrete frequencies at an angle of incidence towards a material sample of interest. The transmitted wave packages interact with the C/C material and a reference sample of polished steel. The wave packages are reflected at the surface and subsequently recorded for evaluation. By comparing the amplitude of a wave package reflected from a porous surface with the amplitude of a wave package reflected at a solid wall the reflection coefficient of the material is determined. The tests were conducted in a nitrogen atmosphere at ambient pressures between $0.01 \cdot 10^5$ Pa and $1 \cdot 10^5$ Pa to account for the low static pressure environment during tests in HEG. Three porous test samples with a porous layer thickness of d = 5 mm, d = 17 mm, according to the porous layer thickness limits provided in figure 2.7, and d = 30 mm were investigated. All porous samples had a cross section area of 100x100 mm and were equipped with an acoustically hard backing plate with a thickness of 3 mm as shown in figure 3.11. A steel sample with a polished surface and a surface roughness of Ra = 0.017 μm was used as reference assuming full reflection. The schematic of the setup is shown in figure 3.12. The measurements were conducted using two pairs of ultrasonic air-coupled Inoson™ sound transducers in transmitter/receiver mode. The PZT transducers (Plumb-Zirconate-Titanate piezoelectric ceramic) have an outer diameter of 17 mm and center frequencies of 197 kHz and 373 kHz. The sound transducers were mounted pairwise with a fixed inclination of 30° focusing on a point approximately 40 mm in front of the transducer holder yielding a signal path of approximately 80 mm. Further, the transducer holder was equipped with four bar spacers to eliminate uncertainties caused by transducer misalignment.[4] The angle of incidence was chosen based on the experimental work performed by Fedorov et al. [25] and a numerical investigation conducted by Brès et al [11]. The latter study

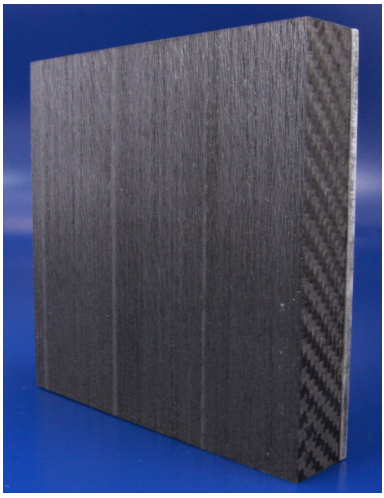

Figure 3.11: Sample with a porous C/C layer of d = 17 mm thickness.

[4] The bar spacers are not shown in figure 3.12.

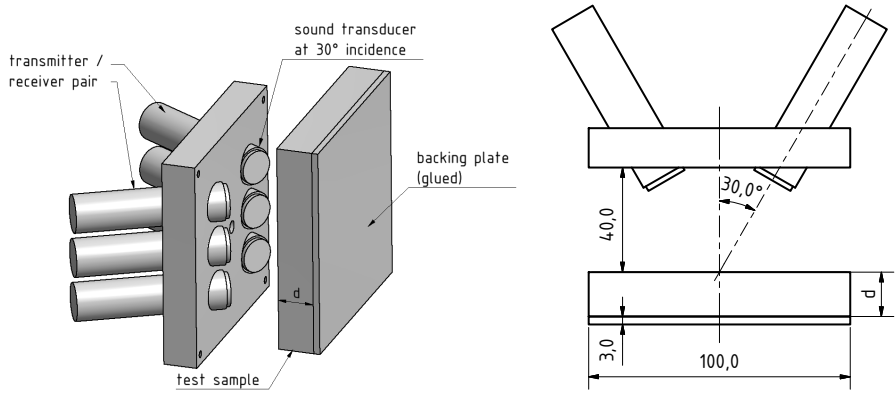

(a) Isometric view. (b) Top view.

Figure 3.12: Arrangement of sound transducers and samples. 3.12a showing an isometric view of the pairwise mounted ultrasonic sound transducers directed towards a sample of thickness d. 3.12b showing a top view of the setup with the main dimensions in millimeter.

revealed that in all cases relevant for the design of ultrasonically absorptive coatings the angle of incidence of second mode waves is smaller than 26°, with decreasing tendency for cooled model walls. The sound transducers were exited using a waveform generator Tektronix™ AFG320 in combination with a RF power amplifier Hubert™ A1020-75. Each sound transducer was driven with its center frequency at a voltage of approximately 160 V peak-to-peak to provide a high signal to noise ratio. Each wave package contained 40 sinusoidal oscillations which allowed the sound transducer to settle and at the same time prevented thermal overloading. The received signals were amplified using a Dewetron™HSI-STG amplifier with a bandwidth of 2 MHz. An Amotronics™ transient recorder was used to sample the signals at a sampling frequency of 50 MHz. The ambient pressure inside the test rig was measured by a MKS Baratron model 626AX13MDE pressure gauge with a range of $0.1 - 1333$ mbar and a resolution of 0.001 % of the full scale.

3.4.2 Evaluation Routine and Results

For each transducer pair and each material sample a series of tests with varying ambient pressure was conducted. Each series consists of up to 800 measurements including three repetitions. Each series was repeated at least twice which results

in a minimum of eight series to characterize two transducer types and four samples. The ambient pressure in each series was gradually increased from $0.01 \cdot 10^5$ Pa to $1 \cdot 10^5$ Pa within about 20 min. The transmitting sound transducer was excited by a sine function. Once the sound transducer was excited it passed a period of transient oscillation until a constant signal amplitude was reached. 15 periods of the second half of the wave package were evaluated. This ensures that only oscillations with constant amplitude contribute to the final result. The number of periods required to reach an oscillation with constant amplitude is about 15. Figure 3.13 provides a representative combination of an

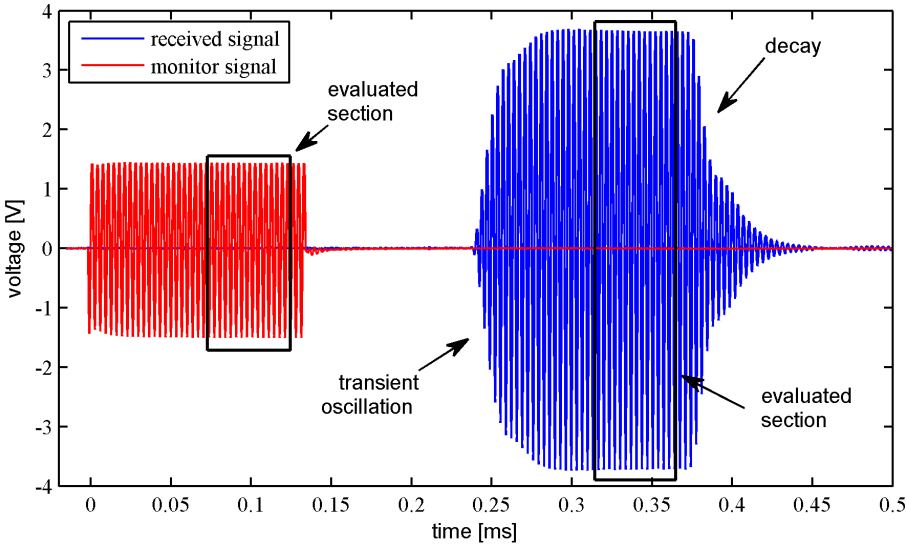

Figure 3.13: Representative amplifier monitor signal and receiver signal for a frequency of f = 295 kHz.

amplifier monitor signal, i.e. a scaled amplifier output signal, and the signal recorded by the receiving sound transducer. The part of the signal used for evaluation is marked. The standard deviation was used as a measure of the signal amplitude of the segment of interest. This approach turned out to be a very robust and reliable way to quantify the amplitude of the oscillations. Subsequently, the obtained amplitudes were plotted against the ambient pressure and fitted with a polynomial fit. Hence, a fit represents the amplitude variation with pressure for one material sample and one frequency. The calculation of the reflection coefficient is based on these fitted values. The error estimation is based on the 95 % confidence interval of the fitted values and the mean variation between two series of experiments.

Below a certain pressure level the received wave packages were found to rapidly decrease in quality and thus were excluded from evaluation. The lower pressure limit of each transducer was found by evaluating the signal quality in terms of its sinusoidal waveform. This was done by fitting a sine function to the part of the received signal chosen for evaluation. The remaining deviation to the optimized sine fit was used as a measure of the signal quality. Figure 3.14 provides a

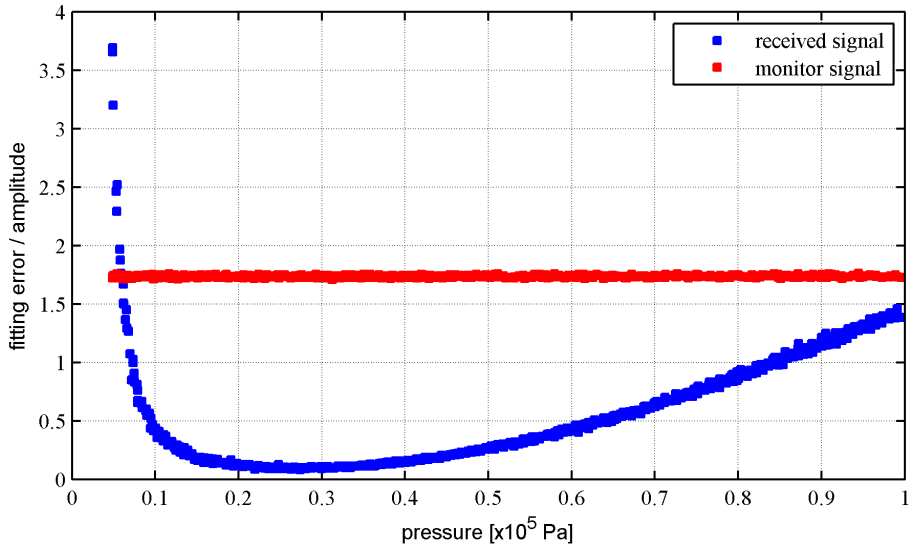

Figure 3.14: Normalized fitting error as function of pressure for a frequency of f = 295 kHz and a porous sample of 5 mm thickness.

representative plot showing the deviation of the sine fits normalized by the corresponding sine amplitude as function of pressure for a complete test series. For the given sound transducer it can be seen that the normalized deviation of the received signal decreases with decreasing pressure. A minimum is reached at approximately $0.27 \cdot 10^5$ Pa. At lower pressures the signal quality decreases which leads to an increasing normalized deviation. Hence, the signal evaluation is constraint to a transducer specific pressure range. The low pressure limit is derived separately for each transducer. The reason for the observed effect is expected to be found in the transducer design. To provide a reference to the measurements the amplifier output signal, driving the transmitter, is recorded and evaluated following the same procedure. It can be seen in figure 3.14 that the amplifier output signal exhibits a constant quality and an excellent repeatability.

The reflection coefficient of the porous material is $R = A_{porous}/A_{solid}$ with A_{porous} being the amplitude of the signal reflected at the porous surface and A_{solid} being the amplitude of the signal reflected at the solid surface. The reflection from the solid surface is assumed to be perfect. Figure 3.15 provides the experimentally obtained reflection coefficient determined for two frequencies, 197 kHz and 373 kHz, and three porous samples of 5 mm, 17 mm and 30 mm depth. The experimentally obtained reflection coefficients do not show a significant difference between the investigated sample depths. The estimated measurement errors overlap to a large extend. However, the reflection coefficients tend towards lower values for higher frequencies while showing a week dependency on the ambient pressure, i.e. below 3 % over the full pressure range. A good agreement between experiment and theory is obtained assuming a structure factor of $\kappa = 8$. The obtained theoretical values confirm the weak dependency on the pressure for pressure levels above $0.1 \cdot 10^5$ Pa.

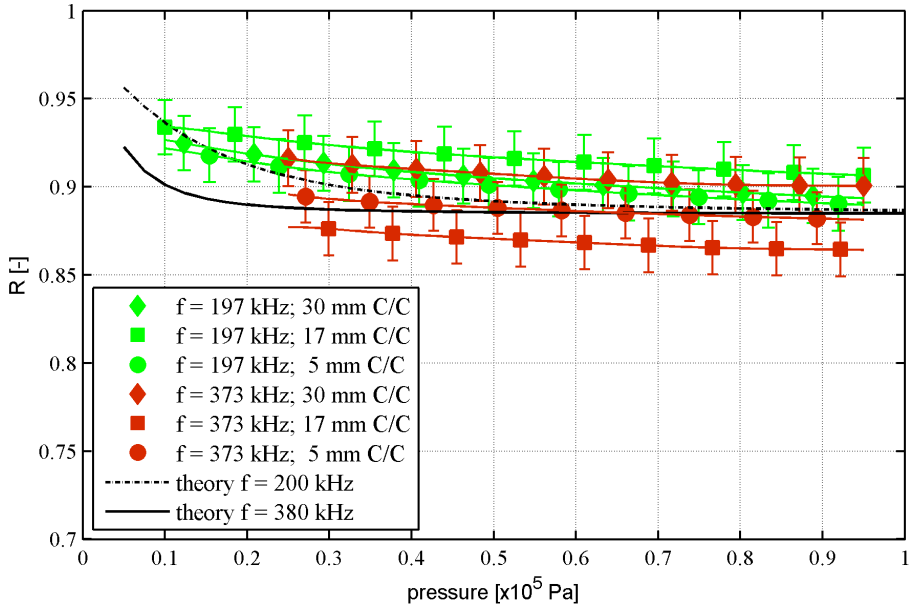

Figure 3.15: Reflection coefficient of porous C/C samples.

Chapter 4

Experimental Results

The present chapter is subdivided into two main sections. The first section solely addresses transition experiments conducted on the solid surface. It focuses on the comparison with other facilities and on the study of the second mode instability. The second section addresses the effect of the porous surface on the transition process. In particular the delay of boundary layer transition and the attenuation of the second mode instability are studied.

4.1 Experiments on Cone Configurations with Solid Surface

The purpose of this section is to provide a basic understanding of the transition process on the solid surface of conical models in HEG. The first subsection addresses the dependence of the transition process on the ground test facility. Tests on the identical model in two facilities with the same operation principle are compared. In the second subsection the effect of nose bluntness is addressed. Results with different nose Reynolds numbers are compared to results available in open literature. The results compare well which validates the methodology of the study. In the last subsection the role of the second mode instability on the transition process in HEG is assessed. It is shown that the second mode instability dominates the transition process. The latter observation was a basic prerequisite to passively control the transition process by means of a porous surface.

4.1.1 Transition Experiments in HEG and HIEST - an Intercomparison

Ground-based boundary-layer transition studies are usually conducted in high-noise conventional wind tunnels or impulse facilities, with disturbance levels higher than in flight. Pate and Schueler [88] conclusively demonstrated that the transition process is influenced by free-stream disturbances, which depend on the wind tunnel and the test conditions. In the framework of the HIFiRE-I project (Hypersonic International Flight Research and Experimentation) transition studies were carried out on a cone-flare configuration, Adamczak et al. [3]. Wind tunnel tests on the forebody of the flight configuration were conducted in three impulse facilities, LENS I at CUBRC (e.g. Wadhams et al. [127]), HIEST at JAXA (e.g. Tanno et al. [119, 120]) and HEG at DLR (e.g. Wagner et al. [133]). As part of the JAXA/DLR cooperative research on 'High Enthalpy Aerothermodynamics' cone model 1, introduced in section 2.3.1, and its instrumentation was exchanged to study hypersonic boundary layer transition. The latter circumstance and the fully available test conditions in both facilities make both studies particularly interesting for comparison. The results of the comparison which are presented in this section were partly published in Wagner et al. [131].

Figure 4.1 shows the nozzle reservoir pressure in HIEST and HEG for a range of representative test conditions. It can be seen that both facilities provide sufficiently long periods of constant nozzle reservoir pressure to investigate boundary layer transition. The test time duration varies between the test conditions which is taken into account in the data analysis. The JAXA cone model was provided to DLR with a cone tip radius of 2.25 mm which was used as the standard tip for all tests. However, run 1307 and 1308 were conducted using a tip radius of 2.5 mm to meet the HIFiRE-I flight model configuration. Table 4.1 provides an overview of the tests chosen for comparison. The free-stream conditions were evaluated at the nozzle exit plane. The tests are grouped according to the unit Reynolds number. The runs in HEG are carried out at low enthalpy, i.e. around 3 MJ/kg. In HIEST the enthalpy was varied up to 8.6 MJ/kg. Detailed information on the free-stream conditions of the tests in HEG are given in table A.2 and in Tanno et al. [120] for HIEST, respectively. Table 4.1 additionally provides the transition Reynolds numbers and the corresponding N-factors for the cases a stability analysis was conducted for. The transition Reynolds number was derived using the model x-coordinate at which the first distinct rise of wall heat flux above the laminar level was detected.

Comparing the transition Reynolds numbers listed in Table 4.1 a dependency on the unit Reynolds number can be seen in both facilities. At a unit

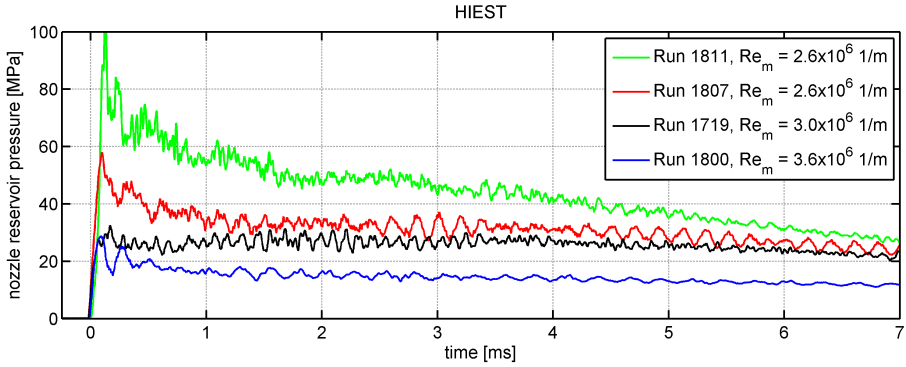

(a)

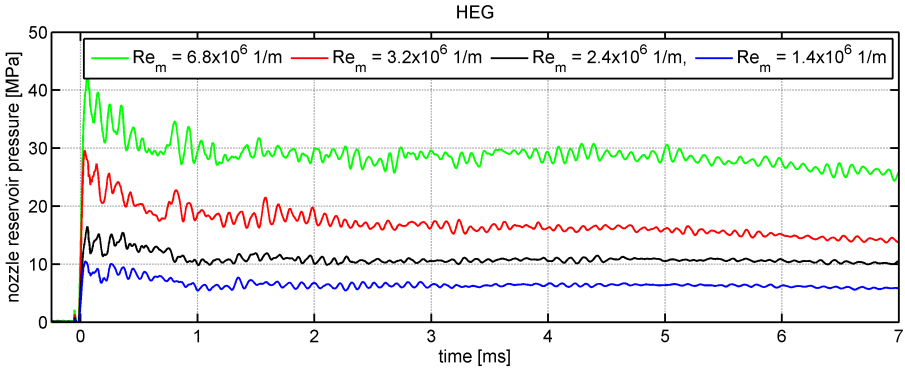

(b)

Figure 4.1: Nozzle reservoir pressure for representative test conditions in HIEST (4.1a) and HEG (4.1b), Wagner et al. [131].

Reynolds number of $\mathrm{Re_m} = 2.4 \cdot 10^6\ \mathrm{m}^{-1}$, e.g. HEG run 1307, a corresponding transition Reynolds number of $\mathrm{Re_{TB}} = 1.9 \cdot 10^6$ is obtained. By increasing the unit Reynolds number to $\mathrm{Re_m} = 6.4 \cdot 10^6\ \mathrm{m}^{-1}$, e.g. HEG run 1050, the corresponding transition Reynolds number significantly increases to $\mathrm{Re_{TB}} = 2.9 \cdot 10^6$. The same trend can be found in the results obtained in HIEST, e.g. showing almost a factor of two in the transition Reynolds number when the unit Reynolds number is increased from $\mathrm{Re_m} = 2.4 \cdot 10^6\ \mathrm{m}^{-1}$, HIEST run 1801, to $\mathrm{Re_m} = 5.9 \cdot 10^6\ \mathrm{m}^{-1}$, HIEST run 1717. The effect is well known in ground test facilities and is expected to be caused by a change of the free-stream disturbance characteristics with changing unit Reynolds number.

Figures 4.2 and 4.3 show the heat flux distribution along the model surface

	Run	Re_m $[x10^6 m^{-1}]$	h_0 $[MJ/kg]$	M [-]	Re_{TB} $[x10^6 m^{-1}]$	N-factor [-]
HEG	1052	1.4	3.1	7.4	laminar	-
	1053	1.5	3.1	7.4	laminar	-
	1054	1.4	3.1	7.4	laminar	-
	1307*	2.4	3.3	7.3	1.9	6.1
	1308*	2.4	3.3	7.3	1.9	6.1
	1046	3.7	3.0	7.4	2.1	5.7
	1047	3.2	3.1	7.3	2.0	5.6
	1055	3.7	3.0	7.4	2.3	6.0
	1049	6.8	3.4	7.4	3.0	6.4
	1050	6.4	3.4	7.4	2.9	6.3
HIEST	1817	1.1	5.0	7.2	laminar	-
	1733	1.5	8.6	6.4	laminar	-
	1818	1.9	3.9	7.5	laminar	-
	1801	2.4	3.3	7.7	2.1	6.0
	1807	2.6	6.1	6.9	2.1	-
	1811	2.6	8.4	6.5	laminar	-
	1719	3.0	4.7	7.3	2.8	7.9
	1800	3.6	2.7	8.0	2.8	-
	1732	5.6	3.3	7.8	3.9	-
	1717	5.9	3.3	7.8	4.1	-

Table 4.1: Test conditions and obtained transition Reynolds numbers for tests in HIEST and HEG on the identical model. The provided Mach numbers are based on the rotational free-stream temperatures. Run 1307 and 1308 were conducted with a cone tip radius of 2.5 mm all other tests with 2.25 mm. The location of first measurable rise in heat flux was used to calculate the transition Reynolds number.

for increasing free-stream unit Reynolds numbers. For a better comparison all heat flux traces were normalized by the heat flux derived from thermocouple readings at x = 230 mm. Figure 4.2a shows the surface heat flux for the lowest free-stream unit Reynolds number range, i.e. $\mathrm{Re_m} = 1.4 - 1.9 \cdot 10^6\ \mathrm{m}^{-1}$. The measured heat flux levels correspond to a laminar boundary layer with a good run to run repeatability. If the unit Reynolds number is increased to $\mathrm{Re_m} = 2.4 - 2.6 \cdot 10^6\ \mathrm{m}^{-1}$ the boundary layer becomes transitional towards the end of the model, see figure 4.2b. The first measurable rise in heat flux is detected at almost identical locations in HIEST and HEG resulting in similar transition Reynolds numbers of approximately $\mathrm{Re_{TB}} = 2.0 - 2.3 \cdot 10^6$. However, the transition process differs, showing a steeper rise of the heat flux in HEG compared to HIEST. As the free-stream unit Reynolds number is further increased the transition locations moves further upstream as indicated in figure 4.3a and figure 4.3b. The transition Reynolds numbers now become significantly higher in HIEST compared to HEG. Furthermore, the difference of the transition

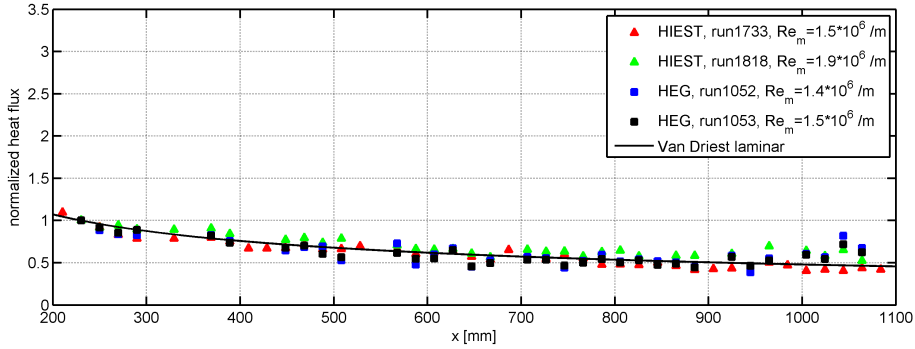

(a)

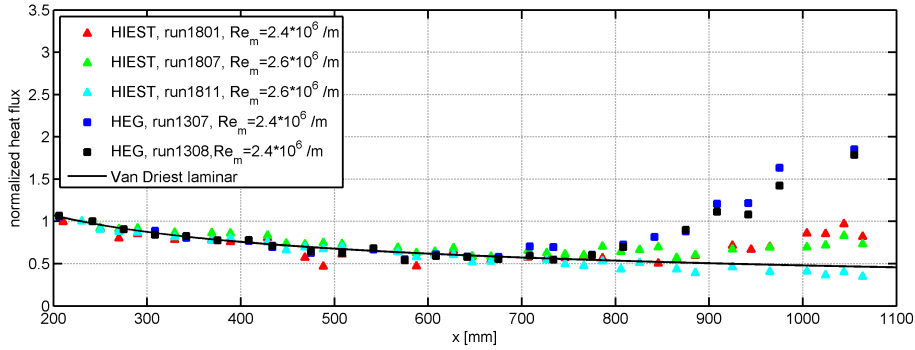

(b)

Figure 4.2: Normalized surface heat flux on cone model 1 in HIEST and HEG for a unit Reynolds number range of $\mathrm{Re_m} = 1.4 - 1.9 \cdot 10^6\ \mathrm{m}^{-1}$ (4.2a) and $\mathrm{Re_m} = 2.4 - 2.6 \cdot 10^6\ \mathrm{m}^{-1}$ (4.2b), Wagner et al. [131].

process in both facilities becomes evident. While in HEG the extent of transition is approximately $100 - 200$ mm, the extent of the transition region in HIEST is much higher. Thus, the increase of heat flux in the observable transition region appears to be much stronger in HEG. The reason for the different characteristic is expected to be caused by different free-stream disturbance levels in both facilities.

In conclusion, hypersonic boundary layer transition studies on a blunted 7° half-angle cone were conducted in HIEST and HEG using cone model 1 with identical instrumentation. Comparable test conditions were found in both facilities to assess the facility dependence on the transition process. A significantly larger transition length was observed in HIEST compared to HEG. Further, the transition Reynolds numbers and N-factors tend to be higher in HIEST. A

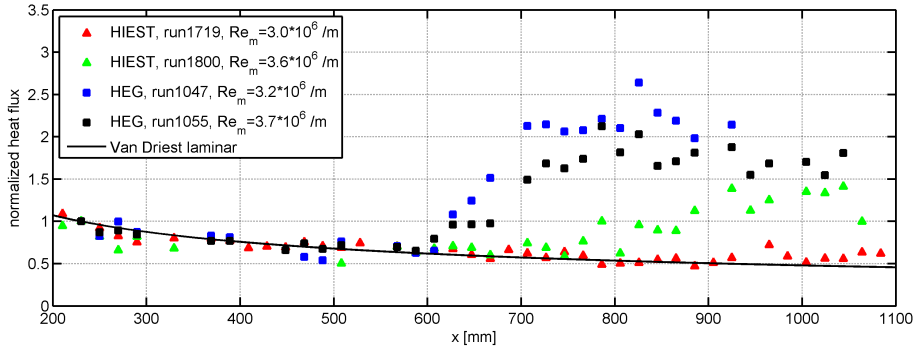

(a)

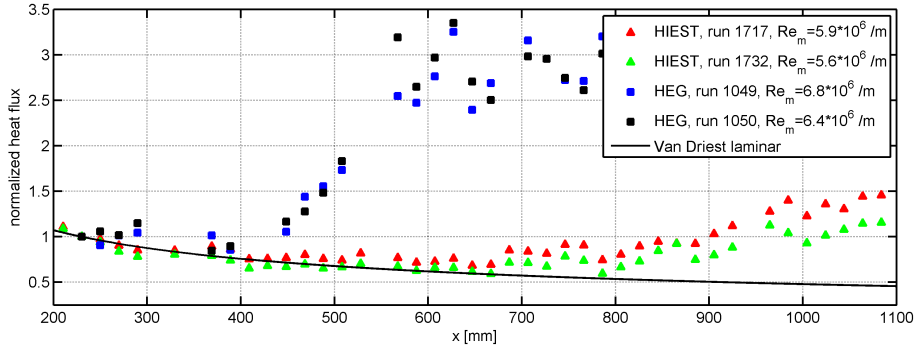

(b)

Figure 4.3: Normalized surface heat flux on cone model 1 in HIEST and HEG for a unit Reynolds number range of $\mathrm{Re_m} = 3.0 - 3.7 \cdot 10^6\ \mathrm{m}^{-1}$ (4.3a) and $\mathrm{Re_m} = 5.6 - 6.8 \cdot 10^6\ \mathrm{m}^{-1}$ (4.3b), Wagner et al. [131].

strong effect of the unit Reynolds number on the transition Reynolds number was found in both facilities indicating a change of the free-stream disturbance environment with changing test conditions. Surface pressure measurements using fast response piezoelectric pressure transducers in combination with boundary layer stability analysis using the DLR NOLOT code, Hein et al. [43], proved the presence of second mode instabilities in both facilities, Wagner et al. [131].

4.1.2 Nose Bluntness Effects

Nose bluntness is an important design parameter for hypersonic vehicles, Anderson [6]. It is known to effect hypersonic boundary layer transition on slender cones and was extensively studied in various wind tunnels in the past. The large number of tests with varying nose bluntness and unit Reynolds number conducted in HEG in the scope of this study allows a comparison with results provided in the literature. The comparison assesses the quality of the data gathered in HEG and the general tunnel disturbance characteristic.

Figure 4.4 provides the transition Reynolds number trend, Re_{sTB}, as function of the Reynolds number based on the nose radius, Re_N. The plot was reproduced from Softley [111] and complemented with results obtained on the three cone models in HEG. The original data were obtained in a shock tunnel at Mach 10 and Mach 12 with a unit Reynolds number ranging from $2.7 \cdot 10^6$ m^{-1} to $9.3 \cdot 10^6$ m^{-1}. A 3.66 m long cone with a 5° half angle and a nose bluntness between 0.254 mm and 25.4 mm was used, Softley et al. [112]. The tests were carried out at a temperature ratio of around $T_w/T_r = 0.26$. Figure 4.4

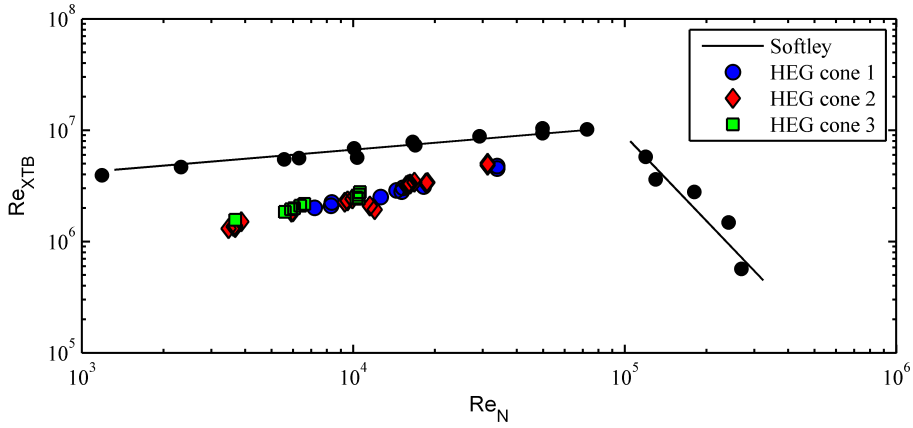

Figure 4.4: Local transition Reynolds number on cones as function of nose tip bluntness. Reproduced from Softley [111].

shows two regions of contrary trends. The region on the left is characterized by an increasing local transition Reynolds number with increasing bluntness. According to Softley [111] transition in this region is located downstream the entropy swallowing distance and the bluntness is considered being small. The trend steeply reverses on the right where transition is located upstream the entropy swallowing distance. In this case the bluntness is considered to be large. The trend reversal takes place where the transition location is identical to the

entropy swallowing distance. Figure 4.4 indicates that all tests conducted on the blunted cones in HEG can be assigned to tests with small bluntness. The trend observed in the HEG data is comparable to what was found by Softley. No strong outliers were found in the complementary measurements which indicates a good repeatability of results.

Moreover, Stetson [118] reported on extensive, systematic studies on nose tip bluntness effects on cone frustum boundary layer transition in hypersonic flows. In contrast to Softley, the blunt cone results are normalized with results obtained on sharp cones in the same facility. The normalization allows a direct comparison between different facilities already accounting for individual wind tunnel disturbance characteristics. All locations of transition begin, s_{TB}, are normalized with the entropy swallowing distance, s_{sw}. Figure 4.5 was reproduced from Stetson [118]. It contains results obtained in a blow down facility operated at Mach 5.9 with a reservoir temperature of 611 K. The model was a 8° half angle blunted cone with a base diameter of 101.6 mm. After reproduction the plot was complemented with the HEG results obtained on the three cone models. Following Stetson the entropy layer swallowing distance parameter was calculated using the method introduced by Rotta [100]. The upper plot in figure 4.5 provides the blunted cone transition displacement normalized by the sharp cone transition location, s_{TB}/s_{TS}. The lower plot provides the local transition Reynolds number ratio between blunted and sharp cone, Re_{sTB}/Re_{sTS}. Thus, it takes into account the local Reynolds number reduction due to the entropy layer generated by the blunted nose tip. Stetson identified three different regions, $s_{TB}/s_{sw} \approx 1$, $s_{TB}/s_{sw} \approx 0.1$, $s_{TB}/s_{sw} \approx 0.03$. In each region multiple effects on transition compete for the dominant role leading to different trends. It can be seen in figure 4.5 that all HEG measurements fall in the region of $s_{TB}/s_{sw} \approx 1$ in which the entropy layer is nearly swallowed by the growing boundary layer. In general, higher transition Reynolds numbers and a small rearward displacements of transition compared to the sharp cone are observed in this region.

To correctly judge the consistency of the HEG data with Stetsons results it should be noted that sharp cone transition data in HEG were available for cone model 3 only. The data obtained on model 3 (marked in green) show an excellent agreement with the data provided by Stetson. The results obtained on model 1 and model 2 are subject to higher scatter since sharp cone results of model 3 had to be used to normalize these results. Therefore, additional uncertainties caused by e.g. slightly different model geometries and instrumentation locations are introduced.

The comparison with Softley and Stetson revealed that the transition Reynolds number trends, caused by bluntness, can be reproduced in HEG. However, as seen in figure 4.4 the absolute transition Reynolds number appears to be lower compared to the data provided by Softley. Plausible explanations might be

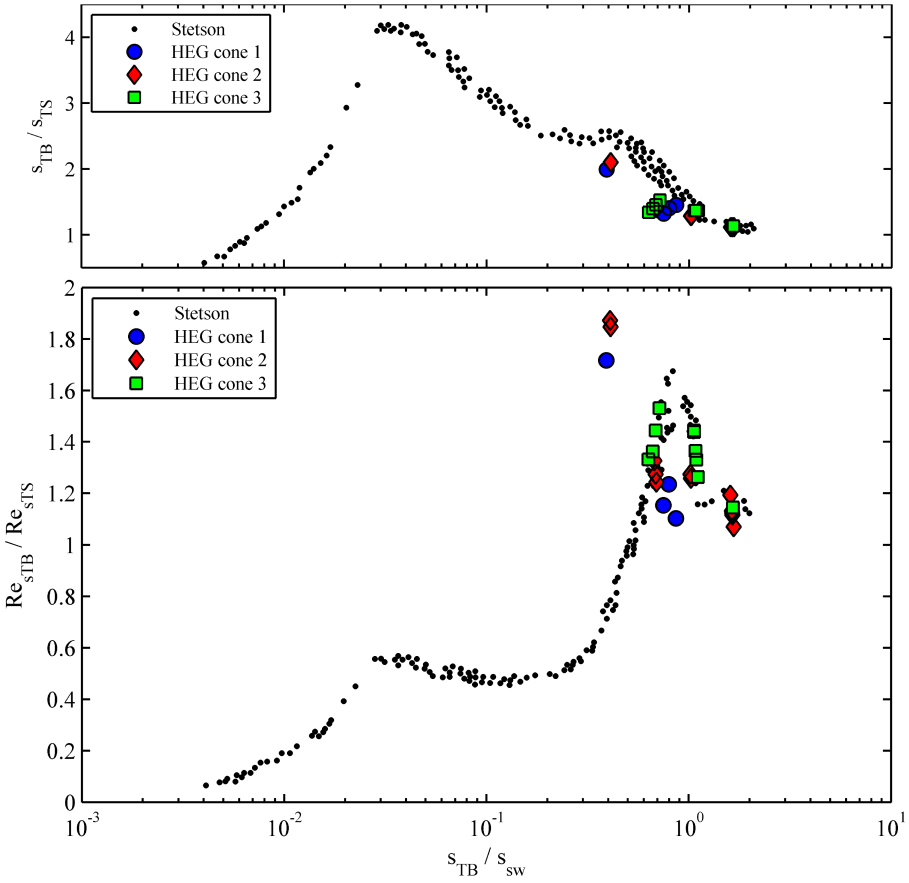

Figure 4.5: Effect of nosetip bluntness on cone frustum transition. Reproduced from Stetson [118].

found in the stabilizing effect of the higher Mach numbers applied by Softley or the probably higher disturbance level environment in HEG. Further, the trend seen in figure 4.4 reveals a pronounced effect of bluntness on the local transition Reynolds number in HEG. The comparison with Stetson finally reveals the importance of the entropy layer swallowing distance parameter and the use of the local Reynolds number. While a relatively good agreement is found comparing solely the transition location changes in figure 4.5 (upper plot) a very good agreement is obtained using the local transition Reynolds number ratios instead, figure 4.5 (lower plot).

4.1.3 Second Mode Instabilities

The boundary layer transition experiments in HEG were carried out under conditions favorable for the development of second mode instabilities, i.e. predominantly two-dimensional boundary layer, small surface roughness and a sufficiently high Mach number regime. Therefore, the second mode instability was expected to be present in the boundary layer. Further, it was assumed to be the dominant instability mechanism leading to transition on all three cone models. Using adequate measurement techniques with sufficiently high frequency response it was possible to detect the instability in the boundary layer above the model surface and study its role in the transition process.

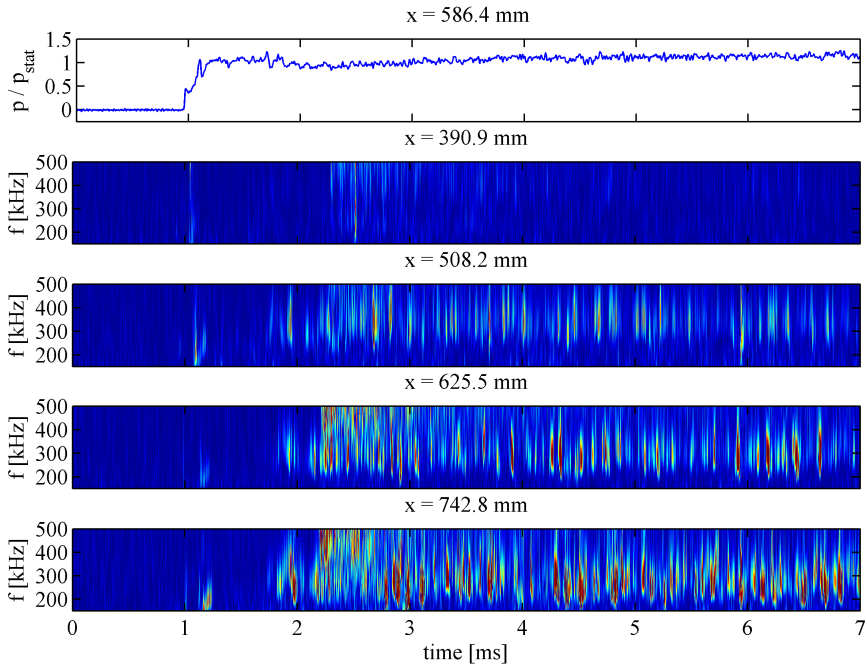

Figure 4.6: Wavelet transform of fast response surface pressure measurements, all sub-figures with identical scale. Cone 3, $Re_m = 2.4 \cdot 10^6$ m^{-1}, $R_n = 2.5$ mm.

The continuous wavelet transform is an evaluation technique providing a high resolution in time and frequency, [7]. Therefore, it was chosen to illustrate the development of the second mode instability over the HEG test time with respect to its amplitude and frequency. Figure 4.6 provides the coefficients of a wavelet transform of a fast response surface pressure measurement. The

energy content of the frequencies is represented by the color coding, whereas blue corresponds to a low and red to a high energy. A Morlet mother wavelet was applied in a frequency range of 150 kHz to 500 kHz with a corresponding frequency resolution between 0.5 kHz and 5.3 kHz. The first plot in figure 4.6 shows the normalized pressure trace of a fast response pressure transducer at a representative location on cone 3. It can be seen that the flow arrives at the model at around 1 ms after shock reflection which corresponds to 0 ms. The flow field needs approximately 1 ms to build up and to reach a constant pressure level. The subsequent plots reveal that almost immediately after the start-up process frequencies in the range of approximately 200 kHz to 400 kHz appeared in the boundary layer. For the present test condition the frequency range can be assigned to the second mode instability as shown by Wartemann et al. [137, 139]. The instabilities were present in the boundary layer over the complete test time. Further, figure 4.6 reveals that the instabilities are not continuously present. Instead, they are grouped in wave packets of different extent.

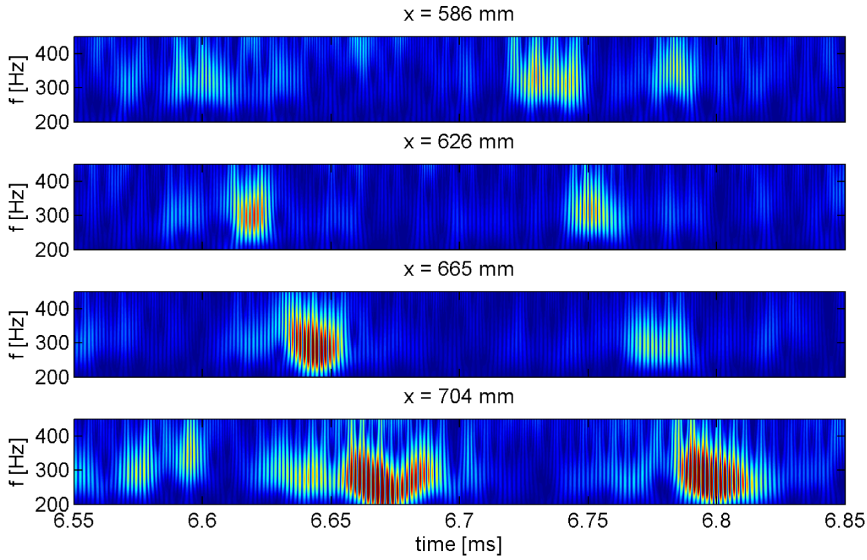

Figure 4.7: Segment of the wavelet transform in figure 4.6. Cone 3, $Re_m = 2.4 \cdot 10^6$ m^{-1}, $R_n = 2.5$ mm.

Figure 4.7 provides the wavelet coefficients of a time segment of figure 4.6, i.e. between 6.55 ms and 6.85 ms. Within this time span two wave packets separated by approximately 0.13 ms move downstream the cone between 586 mm and 704 mm. Starting at x = 586 mm the instabilities have a low pressure amplitude.

While moving downstream the wave packets appear at all subsequent transducers locations, i.e. at x = 626 mm, x = 665 mm and x = 704 mm. The amplitude growth, the increase of the packet length over time as well as the broadening of the frequency spectra are well observable and consistent with results reported by Estorf et al. [23]. The latter observation suggests that the state of second mode breakdown is reached at the last transducers location.
By synchronizing the fast response surface pressure measurements time-wise with a high speed schlieren setup the wave packet seen in figure 4.7 on the left can be observed in the contrast enhanced schlieren images in figure 4.8. The

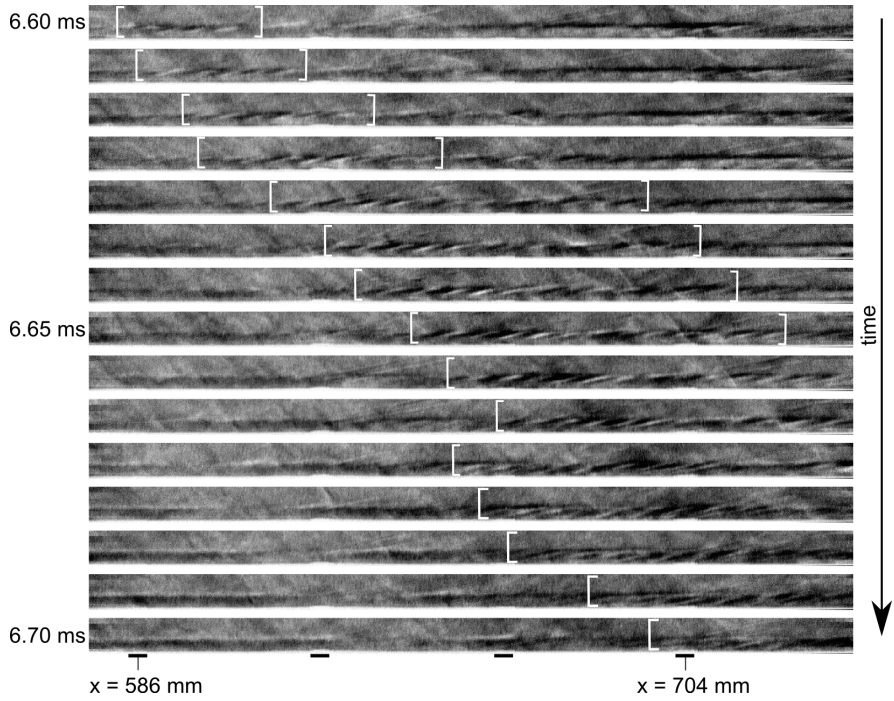

Figure 4.8: Consecutive schlieren images of the laminar boundary layer with the second mode wave packet shown in figure 4.7. The images were recorded at a frequency of approximately 175 kHz. Cone 3, $\mathrm{Re_m} = 2.4 \cdot 10^6\ \mathrm{m^{-1}}$, $\mathrm{R_n} = 2.5$ mm.

sequence covers a time span of 6.55 ms to 6.7 ms and a viewing area between x = 575 mm and x = 740 mm. Each image shows the same section on the top of the cone with the camera being aligned with the cone surface. The model wall starts directly at the bottom of each image. The flow direction is from left to right.

Second mode instabilities are known to appear as rope like structures in the boundary layer as reported by e.g. Demetriades [19] or Smith [110] and more recently by Laurence et al. [58, 57]. Structures of this nature can be identified in the provided images. To assist the reader, white markers were used to mark the approximate limits of the wave packet. In the first image of the sequence the second mode waves appear at the most upstream position with a relatively weak change of the density gradient. In the subsequent images the waves travel downstream while the wave amplitude and the packet extent increase. The black markers at the bottom of the last image provide the positions of the flush mounted fast response pressure transducers which allow a direct comparison with the time resolved data presented in figure 4.7. The comparison between both techniques is excellent as will be shown later in this section.
Furthermore, the schlieren images shown in figure 4.8 can be analyzed row-wise to obtained the spectral information included in each image and thus to provide additional information on the flow field, [57]. Therefore, the instability wavelength and the propagation speed were determined by means of spatial Fourier analysis and cross-correlation, respectively. Consequently, the frequency spectra across the boundary layer can be derived as shown in figure 4.9. The figure provides frequency spectra, time averaged over 2.66 ms, at two

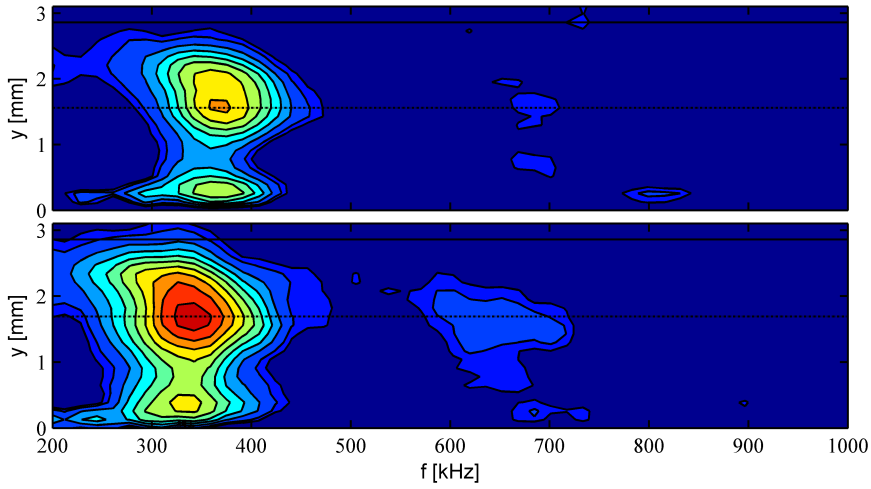

Figure 4.9: Frequency spectra across the boundary layer, averaged over 2.66 ms at x = 614 mm (top) and x = 697 mm (bottom). Both plots are produced using the same scaling. Cone 3, $Re_m = 2.4 \cdot 10^6$ m^{-1}, $R_n = 2.5$ mm.

separate locations above the model surface, i.e. x = 614 mm (figure 4.9 top) and x = 697 mm (figure 4.9 bottom), each evaluated in a window of 47 mm width. A solid line indicates the limit of the boundary layer estimated based

on the density gradient distribution. The dashed line indicates the maximum spectral amplitude in the boundary layer. It can be seen that the second mode instability causes a maximum of the density gradient at 1.7 mm above the surface corresponding to 59 % of the boundary layer thickness. A second peak is apparent in the vicinity of the model surface. While moving downstream, the second mode instability shifts towards lower frequencies and increases in amplitude. Furthermore, the first harmonic of the instability develops between the two location indicating the presence of secondary mechanisms and thus non-linear instability growth and imminent breakdown to turbulence, as introduced in figure 1.2.

In a next step the fast response surface pressure measurements provided in figure 4.7 are band pass filtered between 200 kHz and 450 kHz to isolate the second mode waves in the time resolved signal. The results are plotted in figure 4.10. The data were adjusted to the same time range, i.e. 6.55 ms to 6.85 ms,

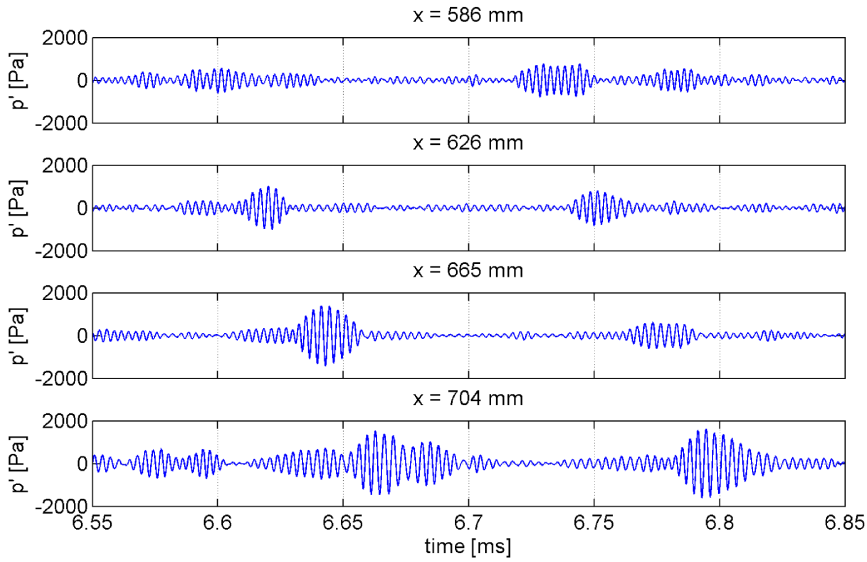

Figure 4.10: Band pass filtered time resolved surface pressure measurements. Cone 3, $\mathrm{Re_m} = 2.4 \cdot 10^6\ \mathrm{m^{-1}}$, $\mathrm{R_n} = 2.5$ mm.

to allow a direct comparison. The figure provides the time resolved pressure fluctuation p'. The results confirm the previously made observations (figure 4.8) regarding the second mode amplitude growth and the increase of the wave packet extent.
The high quality of the data presented in figure 4.10 and the high signal to noise

ratio of the instability in the pressure trace allow to correlate the transducer readings with each other to derive the group velocity of the wave packets above the model surface. Therefore, seven fast response pressure transducers located in a region with second mode presence were band pass filtered between 200 kHz and 450 kHz and cross-correlated with each other. A test time window of 6 ms was chosen with a time stepping of about 0.019 ms which corresponds to the estimated time required for an instability to reach the next downstream transducer. The calculated group velocities are provided in figure 4.11a. The

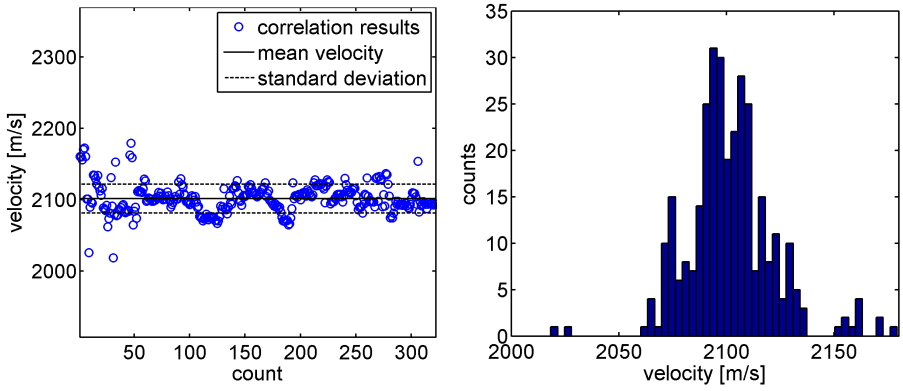

(a) (b)

Figure 4.11: Second mode propagation velocity based on fast response pressure measurements. Cone 3, $\mathrm{Re_m} = 2.4 \cdot 10^6\ \mathrm{m^{-1}}$, $\mathrm{R_n} = 2.5$ mm.

mean value of 2102 ± 40.5 m/s with 95 % confidence interval is based on 322 individual correlations. Figure 4.11b provides the distribution of the cross-correlation results which supports the presented mean propagation velocity. A numerical computation of the flow field around the cone revealed a boundary layer edge velocity of approximately 2455 m/s for the present test condition. Therefore, the second mode waves propagate with about 85 % of the boundary layer edge velocity. The result is in good agreement with data provided by Kimmel et al. [54] and Wagnild [134].

The presence of second mode wave packets along a series of pressure transducers on the cone generatix confirms the angle of attack as well as the yaw angle of the wind tunnel model to be sufficiently small. Thus, the assumption of a predominantly two-dimensional boundary layer is confirmed. Further, the dominant role of the second mode instability in the transition process on slender cone models in HEG is confirmed.

4.2 Experiments on Cone Configurations with Porous Surface

The study of boundary layer transition on solid surfaces presented in section 4.1 revealed the second mode instability to be the dominant mechanism leading to boundary layer transition. This motivated studies on passive hypersonic boundary layer transition control by means of second mode instability damping. The present section focuses on the proof of the concept by

- demonstrating the transition delay caused by the porous surface,
- qualitatively proving the damping of the second mode and finally by
- assessing the amplification rates of the instability on both surfaces.

The results of the present section were obtained on cone model 2, see section 2.3.1, which was equipped with a porous ceramic insert and a polished steel surface allowing to directly compare the boundary layer development on both surfaces. The section partly contains results published in Wagner et al. [132, 130].

4.2.1 Transition Delay

Cone model 2 was tested in HEG in a unit Reynolds number range of $1.4 \cdot 10^6$ m^{-1} to $6.4 \cdot 10^6$ m^{-1} in combination with a nose tip radius of 2.5 mm and 5 mm. An additional test at $\mathrm{Re_m} = 9.8 \cdot 10^6$ m^{-1} was conducted with the 2.5 mm tip to investigate the Reynolds number dependency. Figure 4.12 shows the normalized heat flux distribution on the solid reference surface, figure 4.12 (top), and the porous surface, figure 4.12 (bottom) for the small nose bluntness case. The comparison of both data sets reveals an effect of the porous surface on the heat flux distribution. It can be seen that the heat flux increase due to boundary layer transition is shifted to higher Reynolds numbers. The effect is observable over the full unit Reynolds number range. However, it can be seen that the heat flux measurements on the porous surface are subject to higher scatter compared to the solid surface. Based on a detailed analysis it is assumed that a minor misalignment of the thermocouples is causing the effect. In contrast to a solid steel surface, coaxial thermocouples cannot be integrated into a porous ceramic by polishing the transducer head to the surface. This would cause significant damage to the porous material making it unusable for its design purpose. For this reason, minor transducer misalignment had to be accepted although the integration was carried out with great care.
Figure 4.13 shows the normalized heat flux distribution on both surfaces for the

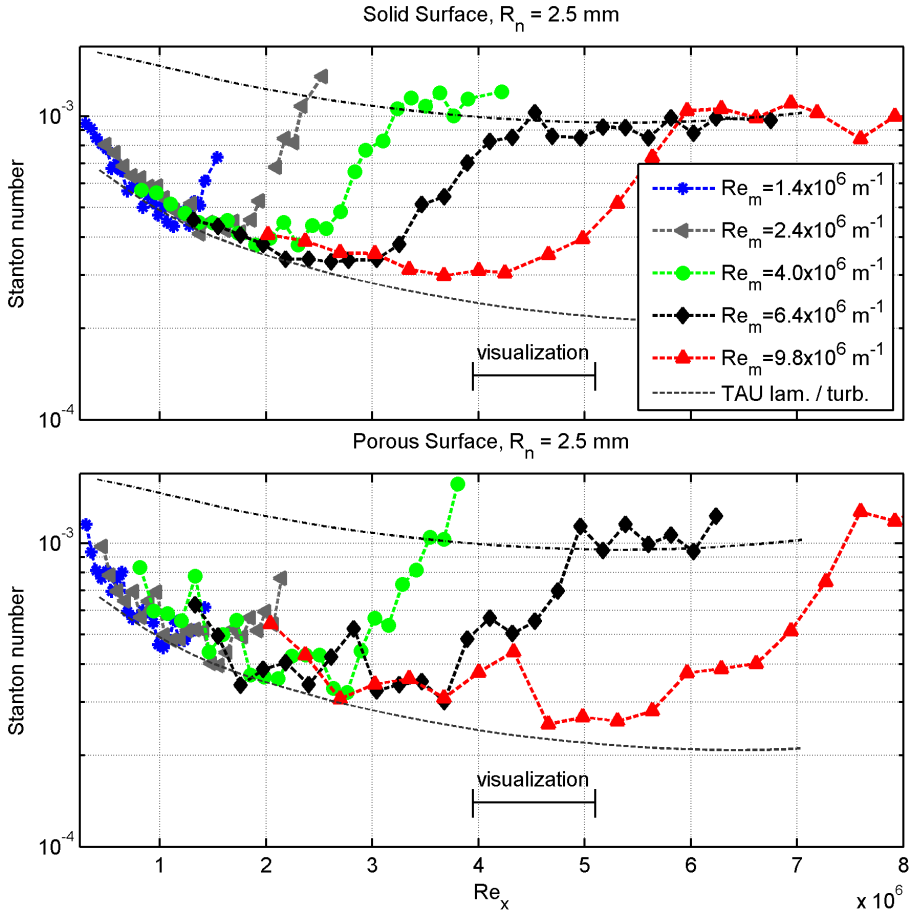

Figure 4.12: Normalized heat flux distribution on the solid and the porous surface of cone 2 with $R_n = 2.5$ mm.

tests with 5 mm nose tip radius. Compared to the small nose tip, boundary layer transition on the solid surface occurs significantly later as discussed in section 4.1.2. In the unit Reynolds number range applied, a fully developed turbulent boundary layer was not reached using the 5 mm nose tip. The comparison with the porous surface reveals that the transition process was strongly delayed.

Due to the above discussed scatter of the heat flux data on the porous surface it is not obvious where to define the beginning of transition on C/C. This issue is addressed in figure 4.14 which provides the results shown in figure 4.12 sorted by unit Reynolds number. To be less dependent on the precise location of the

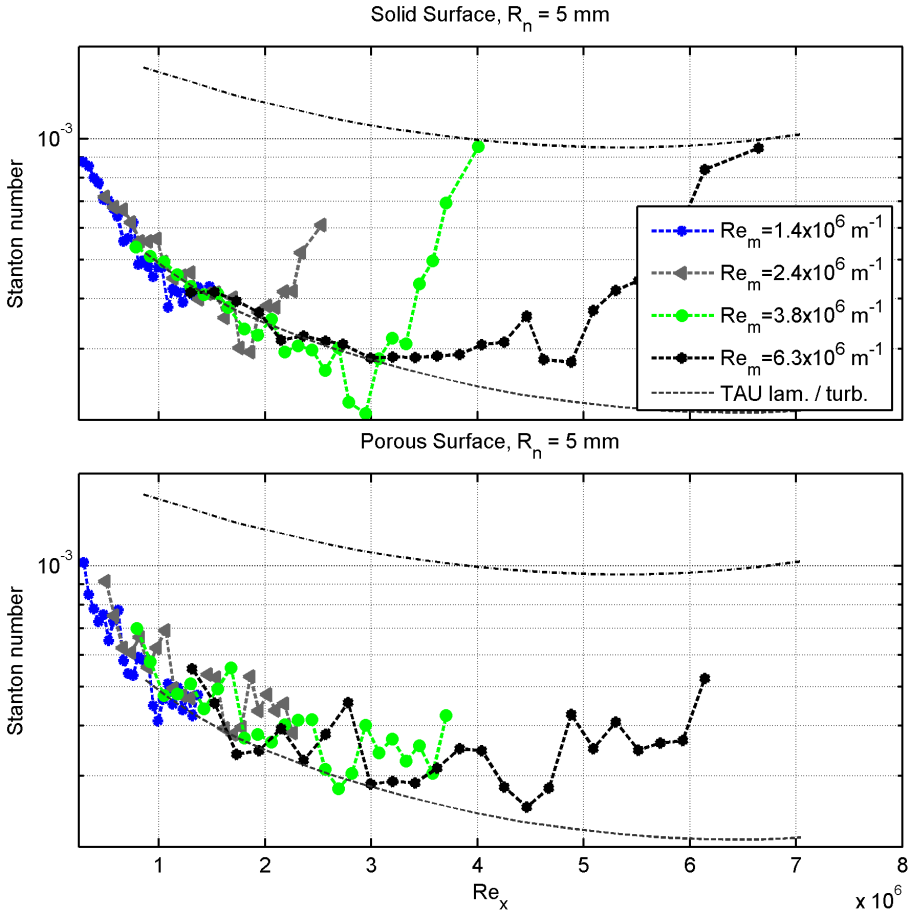

Figure 4.13: Normalized heat flux distribution on the solid and the porous surface of cone 2 with $R_n = 5$ mm.

transition start the last transducer readings before reaching the fully turbulent heat flux level were evaluated. A linear fit was introduced to represent the characteristic slope of the heat flux close to the end of transition. Subsequently, the mean relative displacement of the two fits was calculated. The results presented in table 4.2 show a relative transition delay of 15 % to 29 %. A trend towards higher relative delays for increasing unit Reynolds numbers is apparent. This suggests the porous ceramic to be more effective at higher unit Reynolds numbers. To confirm the observation the boundary layer on both sides of the cone was visualized simultaneously using a high speed schlieren setup.

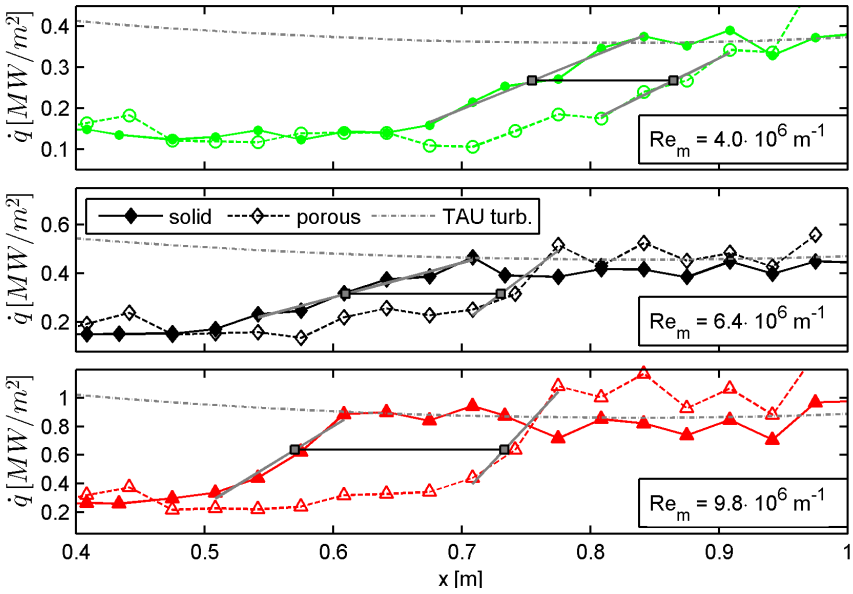

Figure 4.14: Heat flux distribution on the solid and the porous surface of cone 2 with $R_n = 2.5$ mm.

$Re_m[\ \cdot\ 10^6 m^{-1}]$	$(Re_{TP} - Re_{TS})/Re_{TS}$
4.0	0.15
6.4	0.20
9.8	0.29

Table 4.2: Relative transition delay on the porous surface with respect to the solid reference surface, $R_n = 2.5$ mm.

Figure 4.15 provides a schlieren photograph of the cone at a unit Reynolds number of $Re_m = 6.7 \cdot 10^6\ m^{-1}$ and a nose tip radius of 2.5 mm. The sketch on the top indicates the field of view relative to the model. White rectangles in the main image mark the boundaries of the magnified images shown below. It can be seen that the boundary layer on the solid surface, figure 4.15b, is turbulent. In contrast, the boundary layer on the porous surface, figure 4.15c, is predominantly laminar. First turbulent structures become apparent at the downstream end of the image.

The boundary layer state observed in the schlieren visualization can be compared to the mean heat flux distribution in figure 4.12 (black line). The field of view was marked in terms of the local Reynolds number. On the solid

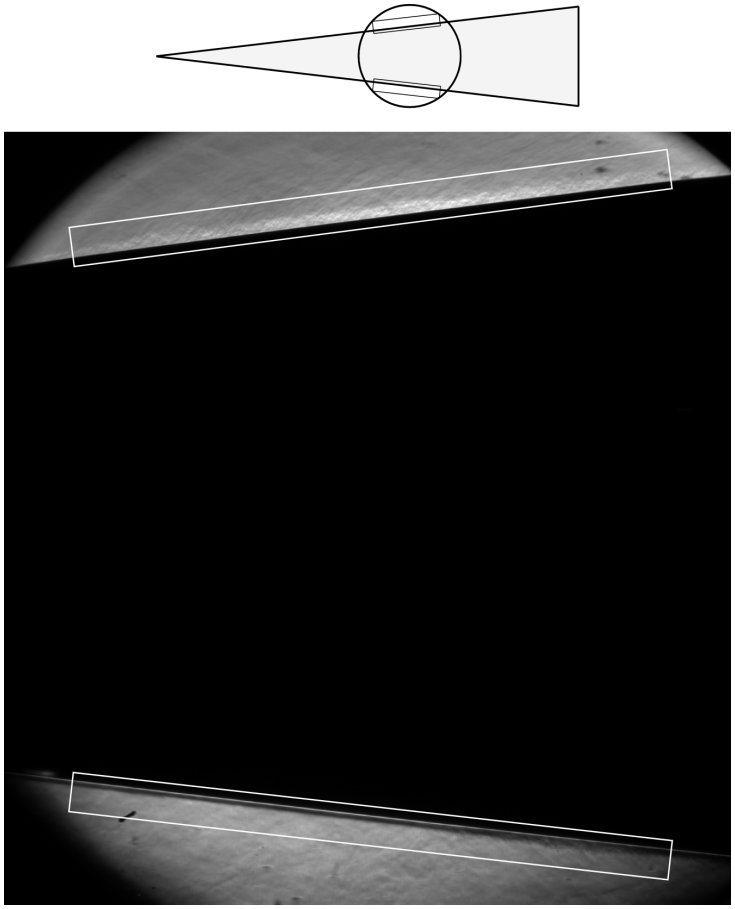

(a) Total view. (top: solid, bottom: porous)

(b) Solid surface

(c) Porous surface

Figure 4.15: High speed schlieren image showing laminar to turbulent transition on the solid surface (top) and a laminar boundary layer on the porous surface (bottom). The flow direction is from left to right. The sketch on the top indicates the visualized section on the cone. The rectangular boxes mark the boundaries of the magnified images which range from s = 590 mm to s = 760 mm measured from the model tip along the surface. $\mathrm{Re_m} = 6.7 \cdot 10^6\ \mathrm{m^{-1}}$, $\mathrm{R_n} = 2.5$ mm.

surface an averaged heat flux corresponding to the late stage of transition was recorded. On the porous surface the heat flux is at a lower level corresponds to an earlier stage of the transition process. Recalling the higher level of scatter in the heat flux data both the schlieren and the thermocouple measurements compare very well.

The transition location on slender cone models is known to be sensitive to angle of attack variations, as reported by Willems et al. [144]. Therefore, additional tests were conducted to study the effect of small deviations from the nominal angle of attack of AOA = 0°. In HEG, the angle of attack of the model was adjusted using an inclinometer with a measuring inaccuracy below 0.027°. In two subsequent tests the angle of attack was varied in a range of ±0.2° which is well above the uncertainty of the inclinometer used. Figure 4.16 shows the normalized heat flux distributions on the porous and the solid surface for these two runs. Although the windward and the leeward side of the model are well distinguishable no significant changes of the transition location on both surfaces were observable.
Since it can be assumed that the angle of attack deviation in all other tests was considerably smaller it is not expected to affect the above discussed results. It

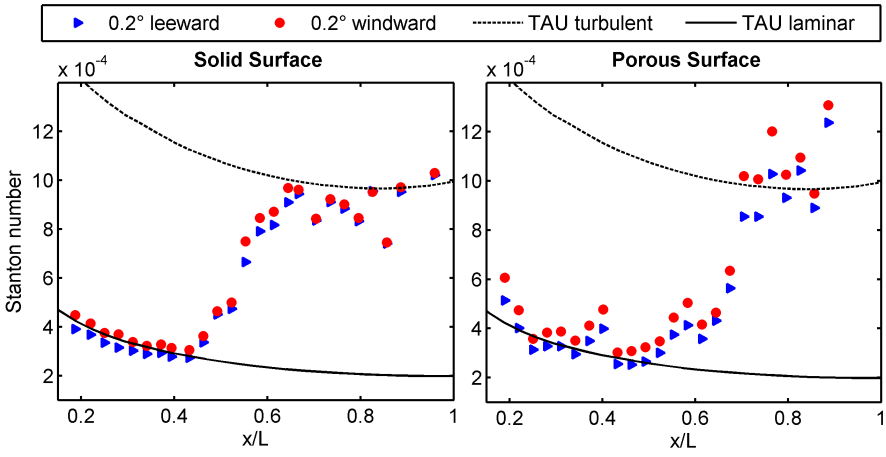

Figure 4.16: Normalized heat flux distribution on the solid and the porous surface of cone 2 for small angle of attack variation, Wagner [128]. $\mathrm{Re_m} = 6.4 \cdot 10^6\ \mathrm{m}^{-1}$, $\mathrm{R_n} = 2.5$ mm.

can be assumed that the angle of attack deviation in all tests with nominally zero angle of attack was considerably smaller.

4.2.2 Second Mode Damping

The boundary layer transition delay on the porous surface, reported in section 4.2.1, suggests that the instability growth above the ceramic insert is reduced. This sections focuses on the second mode instabilities measured on both sides of the cone to investigate the effect of the of the porous material on the instability amplitude.

Figure 4.17 provides the coefficients of the wavelet transforms for a frequency range of 100 kHz to 1 MHz on both sides of cone 2 at x = 785 mm. The boundary layer is laminar at this test conditions as shown in figure 4.12. The

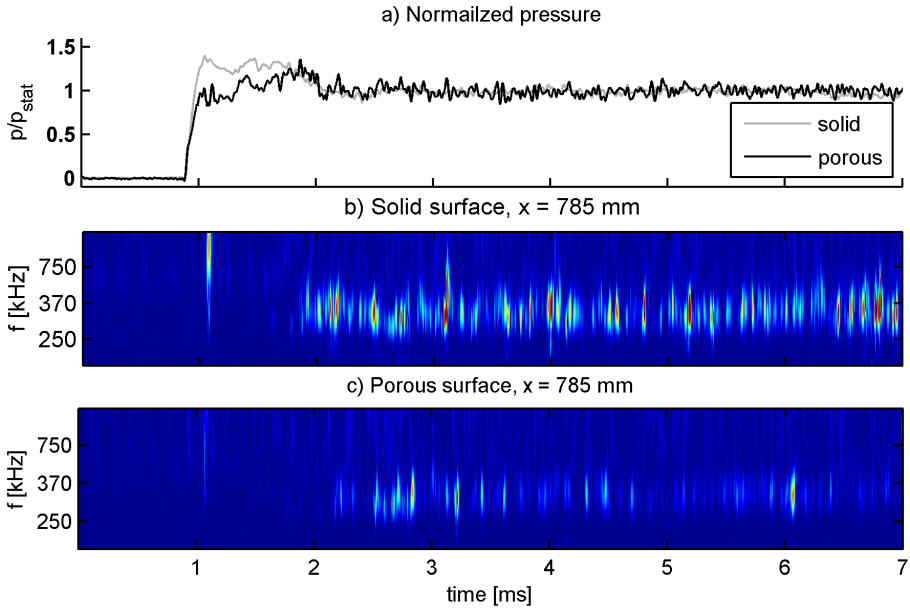

Figure 4.17: Wavelet coefficients of fast response pressure measurements on the solid and porous surface of cone 2 at $Re_m = 1.4 \cdot 10^6$ m^{-1}, $R_n = 2.5$ mm, Wagner et al. [130]. The same scaling is applied to both plots.

figure on the top shows the normalized pressure traces recorded by fast response pressure transducers on the solid and the porous surface. The pressure traces compare well ensuring the comparability of the measurements obtained on different sides of the model. Similarly to what was shown before in figure 4.6 first instability wave packets appear about 1 ms after flow arrival being grouped in separate wave packets. Comparing the wavelet coefficients obtained on the porous surface with those on the solid surface a significantly lower amplitude is

observed. This indicates a damping of the instability and thus a reduction of its growth rate.

The same conclusion can be drawn by analyzing the time averaged frequency spectra as shown in figure 4.18 and figure 4.19. The two plots show the amplitude spectra of the fast response pressure transducers on both sides of the cone for two different nose tip radii. The provided signals were smoothed in the frequency

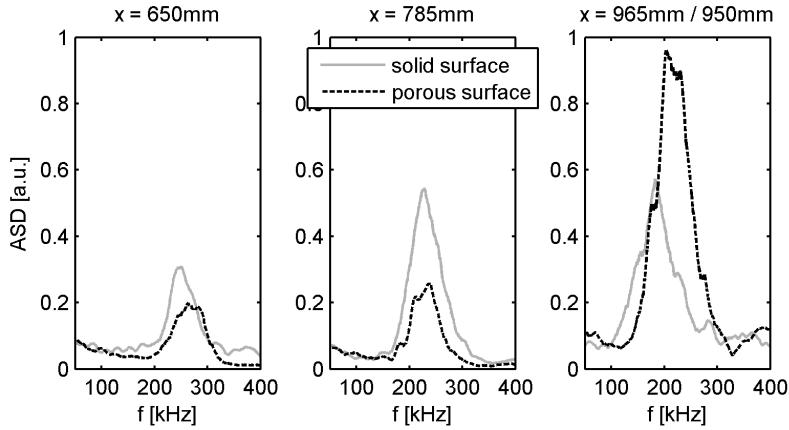

Figure 4.18: Amplitude spectral density of pressure fluctuations on the solid and the porous surface at $\mathrm{Re_m} = 1.5 \cdot 10^6\ \mathrm{m^{-1}}$, $\mathrm{R_n} = 2.5$ mm, Wagner et al. [132].

domain using a Savitzky-Golay filter of 6th order and a length of 251 samples. On the solid surface a second-mode peak forms at 260 kHz at the most upstream position. The peak increases in downstream direction whereas its maximum is shifted to lower frequencies, i.e. 220 kHz at $\mathrm{x} = 785$ mm. At the most downstream transducer location the peak broadened without further increase in amplitude which indicates second-mode breakdown and thus the forming of turbulent spots. This results in a heat flux increase further downstream the transducer position which can be observed in figure 4.12 (the PCB transducer position corresponds to $\mathrm{Re_x} = 1.3 \cdot 10^6$). In contrast, on the porous surface second-mode peak frequencies of 247 kHz and 227 kHz are measured at the first two transducer locations. Both peaks are significantly lower in amplitude compared to the solid surface measurements. Furthermore, the increase of the second-mode peak between the two transducer locations amounts to only 32 % compared to 116 % on the solid surface, based on the amplitude at the first transducer location. Thus, the second mode instability appears to be damped on the porous surface. However, at the most downstream transducer location a second-mode peak at 200 kHz forms with an amplitude indicating a very high

instability growth rate between x = 785 mm and x = 950 mm.

Figure 4.19 provides the amplitude spectral density for a test conducted at

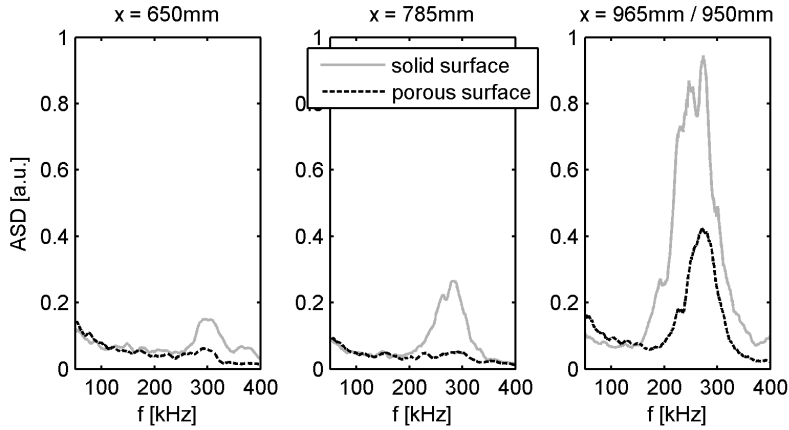

Figure 4.19: Amplitude spectral density of pressure fluctuations on the solid and the porous surface at $Re_m = 2.3 \cdot 10^6$ m^{-1}, $R_n = 5$ mm, Wagner et al. [130].

$Re_m = 2.3 \cdot 10^6$ m^{-1} with a nose radius of 5 mm. Regarding the heat flux traces in figure 4.13 one would expect the most downstream transducer on the solid surface to be in the transitional regime. All other transducers are in the laminar boundary layer. The two most upstream transducers on the porous surface do not shown a significant peak above the noise floor whereas the according transducers on the solid surface show second mode presence combined with a distinct growth. Between the two most downstream transducer locations on the porous surface the second mode amplitude increases rapidly whereas its amplitude remains significantly smaller compared to the reference surface. Hence, a damping effect of the porous surface on the second mode is again apparent.

With increasing unit Reynolds number the beginning of transition on the cone moves upstream. For a unit Reynolds number of $Re_m = 4.0 \cdot 10^6$ m^{-1} the locations of the fast response pressure transducers on both sides of the model range over the complete extent of the transition process. Thus, the most upstream transducer is placed in the early stage of transition, whereas the most downstream transducer is in the fully turbulent region, see figure 4.14. Therefore, figure 4.20 provides an insight into the transition process on each side. Comparing the two most upstream transducers second mode packets become apparent in both signals whereas on the porous surface more energy is concentrated in the second mode frequency range. The results suggests that

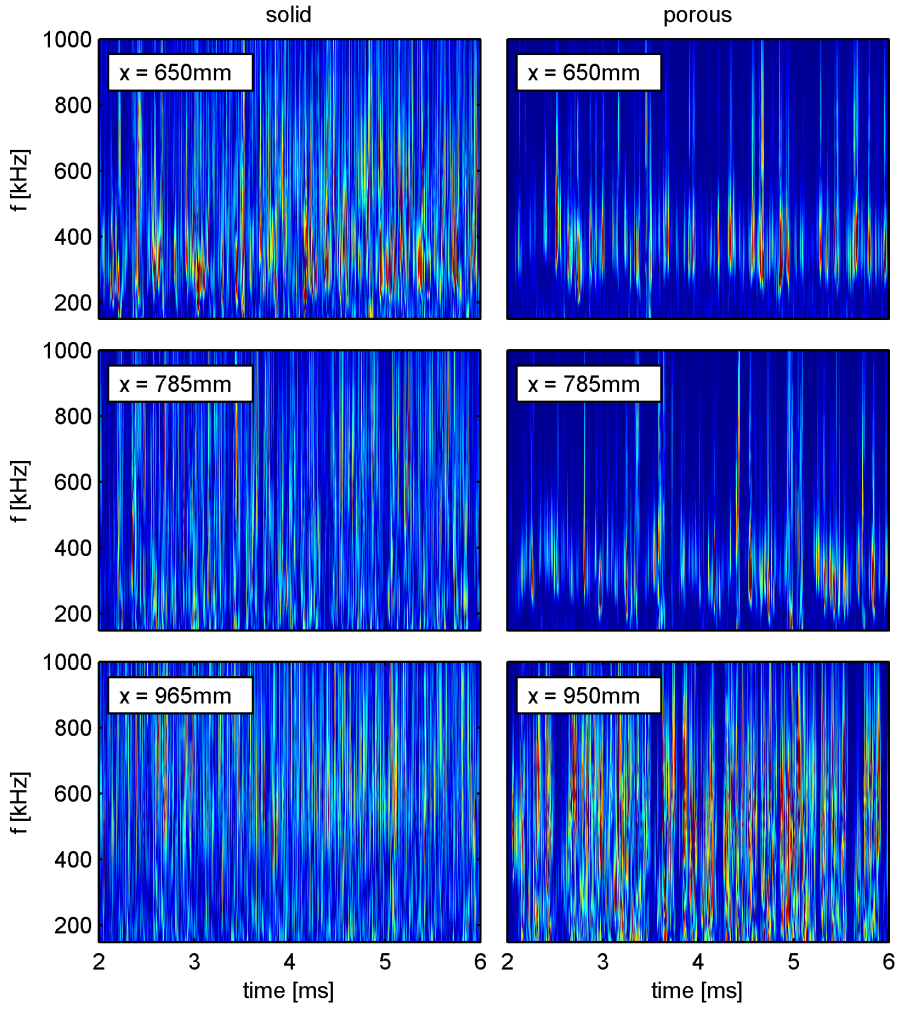

Figure 4.20: Wavelet coefficients of fast response pressure measurements on the solid and porous surface of cone 2 at $\mathrm{Re_m} = 4.0 \cdot 10^6\ \mathrm{m^{-1}}$, $\mathrm{R_n} = 2.5$ mm.

at this position second mode breakdown already occurs on the solid surface. The two following downstream transducer support this conclusion since no second mode waves are apparent anymore. Instead the energy is distributed over the entire frequency range. On the porous surface the second transducer still captures distinct second mode packets, although the amplitude appears

to be smaller compared to the upstream measurement. At the last transducer location the frequency spectra broadened showing no more instabilities. Again, it is noteworthy how quickly the second mode breaks down at the end of the transition process leading to a turbulent boundary layer on the porous surface. The observation suggests a strongly increased amplification rate at the end of the transition process as mentioned before in the discussion of figure 4.18.

4.2.3 Second Mode Amplification Rate

The results presented in section 4.2.2 provide a strong indication that the second mode amplification rate was significantly reduced above the porous ceramic. To confirm the assumption the growth rates were measured on both sides of the cone. However, this task was found to be particularly challenging from the measurement technique point of view. Fast response surface pressure transducers of the type PCB132A are calibration by the manufacturer using a single point calibration at an amplitude three orders of magnitude higher than a second mode wave, Berridge et al. [8]. Although the transducer provides an excellent linearity, uncertainties in the calibration coefficient exist. Although the problem is addressed by Berridge and Schneider [8], no alternative calibration technique is available at the moment.
Further, the short test times in HEG do not allow to average the signal over a long period of time to increase the signal to noise ratio. To overcome the latter issue up to three tests with identical test conditions were averaged to improve the signal quality. The results were smoothed using a Savitzky-Golay filter of 6th order.
Hence, keeping these two issues in mind the transducers were found to be suitable to discuss the basic trends of the second mode amplification rates on both sides of the model, quantitative amplification rates should be interpreted with caution. Note that the transducers on cone model 2 are not positioned along a single stream line. Thus, the calculated spatial amplification rates were derived assuming a fully axisymmetric flow filed and do not represent amplification rates of distinct instability wave packets.

The approximate spatial amplification rate, $-\alpha_i$, was calculated based on the amplitude spectral density of the surface pressure measurements taken at three locations along each side of cone 2. The following equation was used:

$$-\alpha_i = \frac{ln(A_2/A_1)}{s_2 - s_1} \tag{4.1}$$

where A_1 and A_2 are amplitudes of the spectral density at the locations s_1 and s_2.

Figure 4.21 provides the second mode amplification rates for an average unit Reynolds number of $Re_m = 1.5 \cdot 10^6$ m^{-1} and a nose radius of $R_n = 2.5$ mm. The red error bars indicate the standard deviation of the averaged results. At this test condition the boundary layer remains laminar over the complete porous surface, see figure 4.12. On the solid surface the most downstream fast response pressure transducer is in the transitional regime experiencing second mode breakdown as apparent in figure 4.18. Therefore, the last transducer location is not considered for amplification rate calculations. Further, figure 4.18 was used to limit the plotted results to a meaningful range with regard to the second mode frequency range. Figure 4.21 reveals that between x = 650 mm and x = 785 mm the most amplified frequencies are in the range of approximately $200 - 220$ kHz on both surfaces.

The calculated maximum amplification rate is approximately $-\alpha = 11.5$ m^{-1} on the solid surface and $-\alpha = 8.0$ m^{-1} on the porous surface of the model. Further downstream, between x = 785 mm and x = 950 mm the amplification rate above the porous surface increased to $-\alpha = 15.5$ m^{-1} with the most amplified frequencies being around 180 kHz. The data are consistent with the frequency spectra provided in figure 4.18 corresponding to the same test conditions.

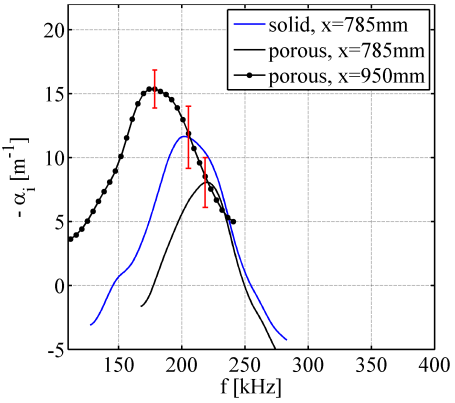

Figure 4.21: Spatial amplification rates, $Re_m = 1.5 \cdot 10^6$ m^{-1}, $R_n = 2.5$ mm.

By increasing the bluntness of the cone while keeping the unit Reynolds number constant additional test cases for transducer based amplification rate measurements are available since the transition Reynolds number increases. Figure 4.22 provides the amplification rates for a nose bluntness of $R_n = 5$ mm and unit Reynolds numbers of $Re_m = 1.4 \cdot 10^6$ m^{-1} and $Re_m = 2.5 \cdot 10^6$ m^{-1}. For the low Reynolds number case shown in figure 4.22a no significant instability amplification was measured between x = 650 mm and x = 785 mm, i.e. $-\alpha \approx 0$. The observation is in line with the frequency spectra provided in figure 4.19. Further downstream amplification rates of about $12 - 13$ m^{-1} were measured on both sides of the cone. The most unstable frequencies were found to be around 195 kHz. Finally, figure 4.22b provides the same set of results for a unit Reynolds number of $Re_m = 2.4 \cdot 10^6$ m^{-1}. Similar to figure 4.21 a considerably higher maximum amplification rate was measured on the solid surface compared to porous surface

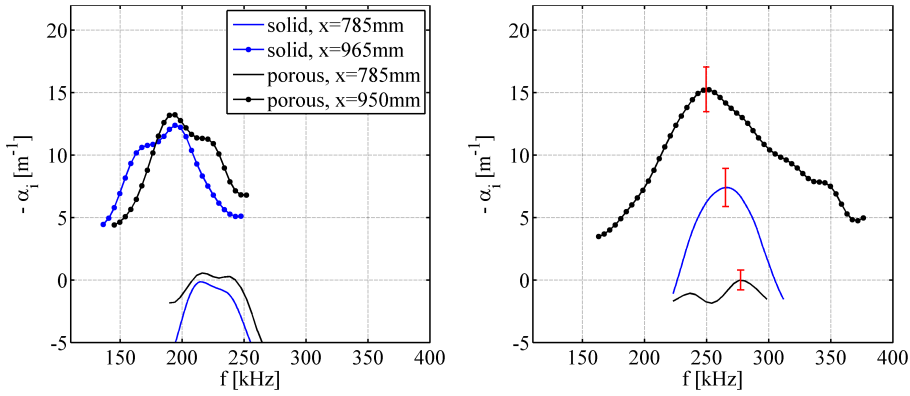

(a) $\mathrm{Re_m} = 1.4 \cdot 10^6\ \mathrm{m^{-1}}$, $\mathrm{R_n} = 5$ mm (b) $\mathrm{Re_m} = 2.4 \cdot 10^6\ \mathrm{m^{-1}}$, $\mathrm{R_n} = 5$ mm

Figure 4.22: Spatial amplification rates measured using fast response pressure transducers. Both figures share the same legend. $\mathrm{R_n} = 5$ mm.

between the first two transducer locations. In fact the instability was fully damped on the ceramics. Further downstream the boundary layer on the solid surface already becomes transitional making a amplification rate calculation meaningless. However, on the porous surface the growth rate increased to values comparable to those measured on the rear of the model in the two previous cases.

Complementary to the transducer based approach measurements using a non-intrusive schlieren deflectometry setup were performed. The schlieren based technique records fluctuations in the density gradient with a bandwidth of 50 MHz. First results after successfully implementing the technique in HEG were presented in Laurence et al. [57, 59]. The non-intrusive nature of the technique provides the advantage of being insensitive to mechanical vibrations of the wind tunnel model. This results in a spectral density of high signal to noise ratio as shown in figure 4.23a. The results were obtained in two consecutive tests on cone 2. While keeping the optical setup constant the model was rotated about 180° around its axis between the two runs. This resulted in a measurement on the solid surface followed by one on the porous surface, both at the same locations along the model, i.e. between x = 787 mm and x = 842 mm. Considerable lower second mode amplitudes on both locations above the porous surface are immediately apparent. The according amplification rates shown in figure 4.24b reveal a maximum growth rate around $-\alpha = 14\ \mathrm{m^{-1}}$ on the solid surface and $-\alpha = 8\ \mathrm{m^{-1}}$ on the porous surface. Both values compare very well with the independently conducted transducer based measurements

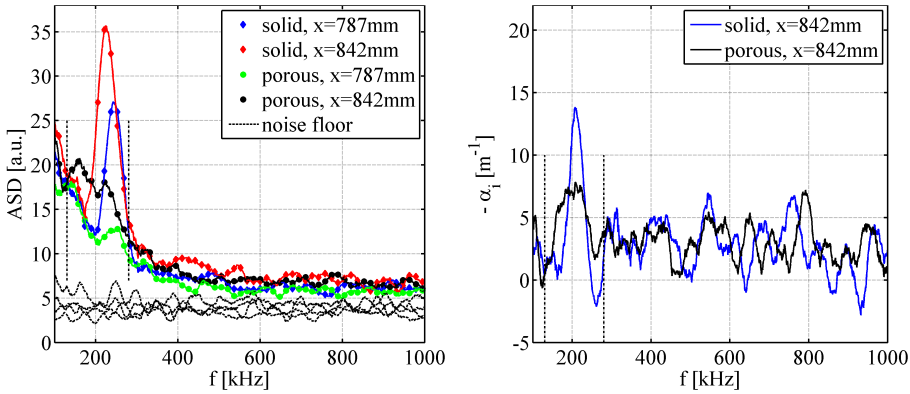

(a) Amplitude spectral density. (b) Amplification rate.

Figure 4.23: Spacial amplification rates based on schlieren deflectometry, $\mathrm{Re_m} = 1.5 \cdot 10^6\ \mathrm{m^{-1}}$, $\mathrm{R_n} = 2.5$ mm.

presented in figure 4.21. For a direct comparison of both data sets the results were plotted into figure A.6. In a next step the unit Reynolds number was increased to $\mathrm{Re_m} = 4.0 \cdot 10^6\ \mathrm{m^{-1}}$. To remain in the laminar boundary layer the measurements were conducted between x = 603 mm and x = 664 mm corresponding to a mean local Reynolds number of $Re_x = 2.5 \cdot 10^6$. As seen in

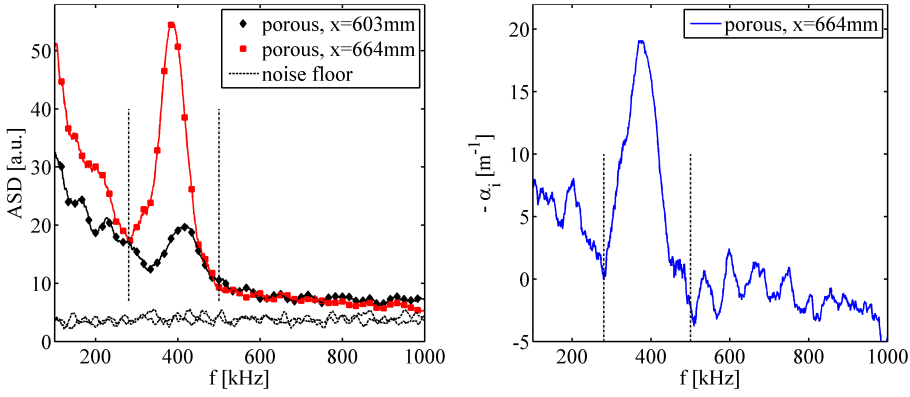

(a) Amplitude spectral density. (b) Amplification rate.

Figure 4.24: Spacial amplification rates based on schlieren deflectometry, $\mathrm{Re_m} = 4.0 \cdot 10^6\ \mathrm{m^{-1}}$, $\mathrm{R_n} = 2.5$ mm.

figure 4.23 the second mode amplitude increases between both measurement positions. The amplification rate on the porous surface was calculated to be about $-\alpha = 19\,\mathrm{m}^{-1}$. This is the highest amplification rate measured corresponding to the highest local Reynolds number investigated.

Despite of the before mentioned uncertainties, the above results confirm that the second mode amplification rate is significantly damped on the porous surface. Further, the results show a strong increase of the amplification rate towards the rear of the model and thus towards higher local Reynolds numbers. This implies a reduction of the damping efficiency of the carbon-carbon ceramic. Furthermore, a very good agreement between the amplification rates based on two independent measurement techniques was obtained which strongly supports the presented results.

Chapter 5

Discussion

Free-Stream Disturbance Environment For the first time hypersonic boundary layer transition on slender cones was addressed in HEG. The studies were initiated in the frame of the JAXA/DLR cooperation on *High Enthalpy Aerothermodynamics* by interchanging a 7° half angle cone, described in section 2.3.1, between the two shock tunnels HEG and HIEST. The comparison of the results obtained on both models is presented in section 4.1.1. It was shown that even though the identical model and instrumentation was used, the beginning of transition and the transition extent at comparable test conditions differ significantly. The results underline the strong dependency of transition studies on the test facility and the associated free-stream disturbance characteristics of each test environment.

The Second Mode Instability Furthermore, the experiments revealed the presence of the second mode instability in the boundary layer of the model in both facilities. It was the first time the second mode instability could be associated to the transition process on such configurations in HEG. The development of the instability in terms of amplitude and frequency along the solid model surface was investigated in section 4.1.3. The dominant role of the instability in the transition process was shown by relating the frequency spectra of fast response pressure transducers with the time averaged heat flux distribution along the model, see figure 4.20 and 4.12. The presence of second mode wave packets along a series of pressure transducers on the cone generatrix, as shown in section 4.1.3, confirmed the assumption of a predominantly two-dimensional boundary layer. Thus, the angle of attack as well as the yaw angle

of the wind tunnel model is shown to be sufficiently small not to affect the fundamental transition process.
Although indicated by linear stability theory, Mack [72], the prominence of the instability in the transition process was not clear at the beginning of the study. Particularly, since impulse facilities are expected to have a high level of free-stream fluctuations which, if sufficiently high, change the transition path or even bypass transition as described in section 1.1.1. However, the results on slender cones with solid surface led to the assumption that the free-stream disturbances in HEG and HIEST are sufficiently low in the frequency range of the second mode to allow second mode instability growth. This is in line with a study on free-stream density perturbations in the T5 shock tunnel using focused laser differential interferometry, Parziale et al. [86]. The study revealed a strong dependency of the tunnel noise on the disturbance frequency indicating low disturbance amplitudes in the second mode frequency range.

Nose Tip Bluntness To evaluate the results obtained on all three cone models with open literature results, the extensively studied effect of nose bluntness on transition was compared to the work of Softley [111] and Stetson [118]. The comparison of the data is conducted in section 4.1.2 following the method introduced by the before mentioned authors. A good repeatability of the results was shown. Furthermore, it was found that the test conditions covered in the scope of this work, in respect to the unit Reynolds number and the nose radius, can be assigned to transition studies with "small" nose bluntness. The trend of increasing transition Reynolds number with increasing bluntness Reynolds number was confirmed, see figure 4.4. The results are in line with the numerical study on the influence of cone bluntness on boundary layer instabilities conducted by Rosenboom et al. [99]. It was found that an increasing bluntness leads to a reduction of the amplification rate and a downstream shift of the position at which the first unstable frequencies appear.
In contrast to Softley, the slope of the transition Reynolds number increase with bluntness was found to be higher. At the same time the total transition Reynolds numbers were lower. Both could possibly be explained by the two different cone model half-angles, i.e. 5° in Softley's experiments and 7° in in the present study, as well as different free-stream disturbance levels in both facilities. The method chosen by Stetson eliminates the facility dependency by normalizing the blunt cone results with sharp cone results of the same facility. The comparison in terms of transition Reynolds numbers reveals an excellent agreement with the data obtained in HEG on cone 3, see figure 4.5. In conclusion the approach chosen in the study with respect to the model manufacturing and instrumentation as well as the test facility is proven to be suitable for the

conducted study.

Ultrasonically Absorptive C/C Based on the gathered understanding of the transition process it was assumed that a porous surface can be used to delay boundary layer transition by means of second mode attenuation. In contrast to existing work on porous surfaces with regular porosity or random microstructure (felt metal), e.g. [26, 94, 76, 27, 78], the present study aimed to employ a material which combines basic TPS properties with the capability to damp second mode waves. Therefore, the carbon-carbon ceramic described in section 3.1 with a natural, random porosity of about 15 % was chosen based on the mechanical properties such as porosity, pore size and machinability. To account for the small test times in HEG the time required for the test gas to fill the pore volume was estimated in section 3.2. The filling process was found to be sufficiently short with respect to the nozzle starting process. Subsequently cone model 2 was designed, manufactured and equipped with an insert holding the instrumented carbon-carbon ceramic as described in section 2.3.1.

C/C Absorber Properties To understand the effect of the porous material on the boundary layer instability the acoustic properties of C/C had to be assessed. This was done theoretically by means of the quasi-homogeneous absorber theory described in section 3.3 and experimentally by means of direct reflection coefficient measurements, described in section 3.4. In the latter case a test rig specifically designed to directly determine the reflection coefficient was employed. Custom made ultrasonic sound transducers, transmitting in the frequency range of the second mode waves, were used. The absorption characteristic of C/C was determined by investigating the reflection of ultrasonic waves from three porous test samples of varying thickness. The test rig is described in section 3.4.1 followed by section 3.4.2 which describes the method and the results. All technical means available at the present time were exploited to directly determine the reflection coefficient of the ultrasonically absorptive material in the pressure and frequency range of interest. The measurements revealed that C/C is an effective ultrasonic absorber. However, it was found that the C/C absorption characteristics were not well adapted to the test condition applied in HEG. Although the theory revealed an absorption of up to 19 % the absorption coefficient rapidly decreases towards lower ambient pressures as seen in figure 3.10. The trend is pronounced with decreasing frequencies. The experimentally obtained results, provided in figure 3.15, show an increase of the reflection coefficient towards lower pressures and thus support the theoretical prediction. The static pressure range above the model surface covered by the

HEG test conditions in this study was between approximately $0.017 \cdot 10^5$ Pa and $0.11 \cdot 10^5$ Pa. Consequently, it can be expected that for all tests in HEG an absorption coefficient distinctively lower than 19 % is reached. Since low surface pressures are directly associated with low unit Reynolds numbers and vice versa, the second mode damping efficiency of the C/C will be higher for higher free-stream unit Reynolds numbers. In return, the relative transition delay will be higher at higher unit Reynolds numbers. This assumption is supported by the results summarized in table 4.2 and figure 4.14 which provide the measured transition delay and the corresponding surface heat flux, respectively.
Further, the numerical and experimental investigations did not show a dependency of the absorption characteristics on the material depth. The weak dependency on the frequency found in the absorber theory could be confirmed in the bench tests showing a trend towards lower reflection coefficients for higher frequencies. Due to the high attenuation of ultrasonic waves in low pressure air the measurements do not cover the full pressure range of the HEG test conditions. Thus, the predicted steep increase of the reflection coefficient towards lower pressures could not be confirmed experimentally, although the global trend is matched.

Effect of C/C on Transition Tests in HEG revealed a damping effect on the second mode instabilities leading to a transition delay of up to 29 % as shown in figures 4.15 and 4.14. In addition the effect on the second mode instability was investigated qualitatively by revealing the attenuation of the acoustic waves above the surface and quantitatively by measuring the amplification rates. Linear stability analysis revealed that for all free-stream conditions applied in combination with the 2.5 mm cone tip the location on the model, at which the second mode waves become unstable for the first time, is well upstream of the porous insert, Wartemann [135]. Considering the second mode attenuation distinctively lower pressure amplitudes were measured on the porous side of cone model 2 as shown e.g. in figures 4.17 and 4.19. In some cases an unexpectedly high second mode amplitude was measured on the rear part of the porous surface, indicating a strong increase of the instability amplification rate. Figure 4.18 provides representative spectral densities showing a distinctively stronger second mode instability at the last transducer location compared to the upstream measurements. Keeping in mind the increasing boundary layer thickness, and thus the decreasing second mode frequency, in downstream direction the absorption coefficient is expected to decrease as well. The results provided in figure 4.18 correspond to a low pressure test condition, i.e. static pressure above the surface of around $0.017 \cdot 10^5$ Pa, accompanied by a low second mode instability frequency of approximately 200 kHz. To estimate the absorption coefficient along the model surface for this test condition

the quasi-homogeneous absorber theory can be used. The prediction of the absorption coefficient over pressure, presented in figure 3.10, can be rearranged to express the coefficient along the model for a specific test condition. Therefore, experimentally obtained second mode peak frequencies are used assuming the instability wave length to scale with 2δ, where δ denotes the boundary layer thickness, Mack [70]. Further, the boundary layer thickness and the model x-coordinate are assumed to scale with $\delta \propto \sqrt{(x)}$, [105, 20]. Figure 5.1 provides

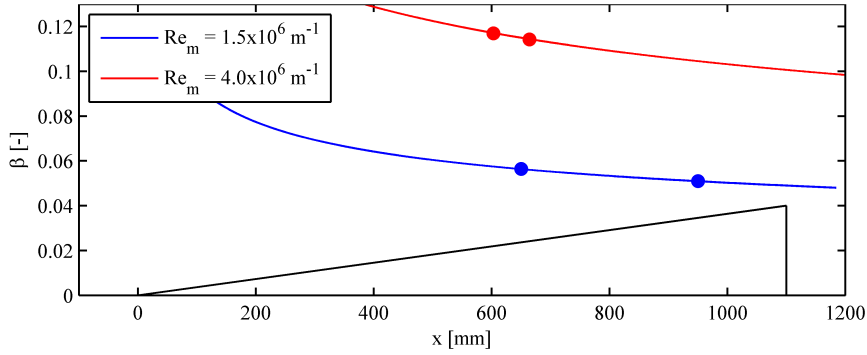

Figure 5.1: Absorption coefficient along the model for two HEG test conditions based on second mode peak frequencies measured at the indicated position on the cone.

an estimate of the absorption coefficient based on the above assumptions for two test conditions, i.e. $\mathrm{Re_m} = 1.5 \cdot 10^6\ \mathrm{m}^{-1}$ and $\mathrm{Re_m} = 4.0 \cdot 10^6\ \mathrm{m}^{-1}$. The second mode peak frequencies were obtained from the data sets presented in figure 4.18 and 4.24. The according positions of the measurements on the model are indicated using circular markers. The distribution of the absorption coefficient supports the above discussion showing a decrease in downstream direction as well as a higher absorber efficiency in case of higher unit Reynolds number, i.e. higher static pressure.

Spatial Amplification Rates Concerning the second mode spatial amplification rates the results should be understood as a point wise insight rather than a systematic study of the second mode growth which was not the purpose of the measurements at that time. To quantitatively assess the development of the second mode instability, the spatial amplification rates were measured by means of schlieren deflectometry and fast response pressure transducers, see section 4.2.3. A good agreement between the amplification rates calculated based on the two independently used measurement techniques was obtained as shown in

figure A.6. It supports the chosen approach and confirms the suitability of the measurement techniques. The measured amplification rates are in line with the qualitative results presented before, i.e. showing a reduced amplification rate of the instability above the porous surface. A final conclusion on the development of the second mode amplification rate cannot be drawn from the measurements provided. Therefore, a systematic study along the model at different test conditions would be required. Nevertheless, assuming linear stability growth, the results can be used as a first step to validate new boundary conditions for linear stability analysis considering ultrasonically absorptive porous materials with random microstructure. Corresponding work is currently in progress at DLR, Wartemann and Wagner [140].

Chapter 6

Conclusion

The hypersonic boundary layer transition process on slender cones at zero angle of attack in HEG was shown to be dominated by the second mode instability. Both the development of the instability amplitude and frequency along the model as well as its breakdown to turbulence were investigated by means of fast response pressure measurements, heat flux measurements and schlieren visualization. The obtained results compare well with studies conducted in established hypersonic test facilities used for boundary layer transition studies. Although a good overall agreement was found, the sensitivity of the transition process to the test facility became apparent considering transition location, transition length and the effect of bluntness. This highlights the need for the assessment of the free-stream disturbance environment in ground facilities used for transition research.

Furthermore, ultrasonically absorptive carbon-carbon ceramics was shown to be suitable for passive hypersonic boundary layer transition control. The effect of carbon-carbon ceramics on the second mode instability and ultimately on the transition location was studied by means of wind tunnel testing and by assessing the ultrasonic absorption properties. For the latter, the approach of using the quasi-homogeneous absorber theory in combination with the direct measurement of the reflection coefficient was proven to be effective. Carbon-carbon ceramics was shown to absorb up to 19 % of the acoustic power transmitted towards the porous surface. A corresponding reduction of the second mode amplification rate was found experimentally.

However, the absorber characteristic of the carbon-carbon ceramic was not well adjusted to the test conditions applied in HEG, resulting in a decreasing absorber efficiency with decreasing unit Reynolds number and static pressure. This underlines the need to properly adapt the porous material to meet the required

absorption properties imposed by the aerodynamic environment. The test rig developed in the scope of this study provides a stand-alone and inexpensive technique to experimentally assess ultrasonic absorption properties. Therefore, the present study provides all means to assess today's and future porous materials with respect to their applicability for passive hypersonic boundary layer transition control.

Ultimately, porous carbon-carbon ceramics was shown to be a promising candidate for the development of future TPS materials with passive transition control capabilities. Future work to further advance this technique would comprise the identification of hypersonic flight conditions of interest, the specification of the required absorber properties and the development of the porous TPS followed by bench tests to assess the effective acoustic absorber properties. The absorber would have to be approved in controlled wind tunnel experiments before the final integration onto a hypersonic vehicle for flight testing.

Appendix A

Appendix

section	notation	dimension
overall:	-> length	60 m
	-> mass	250 t
compression tube:	-> length	33 m
	-> diameter	0.55 m
	-> volume	8.06 m^3
shock tube:	-> length	17 m
	-> diameter	0.15 m
	-> volume	0.301 m^3
sec. reservoir	-> volume	5.4 m^3
test section	-> diameter	1.2 m
	-> volume	2.1 m^3
dump tank	-> volume	35.5 m^3
piston	-> mass	275 kg, no brakes
	-> mass	875 kg, brakes

Table A.1: HEG dimensions.

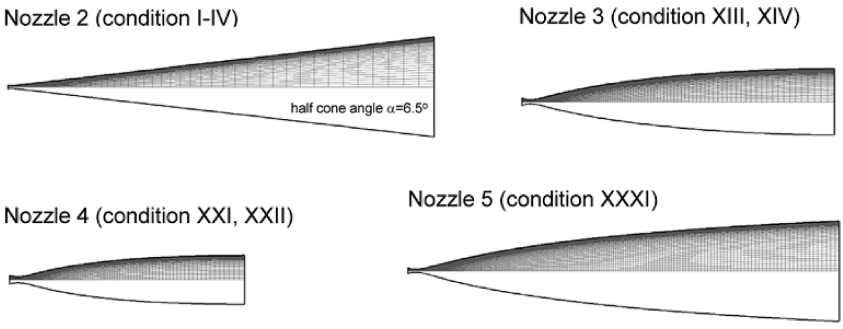

Nozzle	2	3	4	5
nominal M	8	8	6	10
d*[mm]	22	40	50	26
d_{Exit}[mm]	880	590	430	880
A_{Exit}/A^*	1600	218	74	1146
L [mm]	3780	2710	2015	3780

Figure A.1: HEG nozzles, [39].

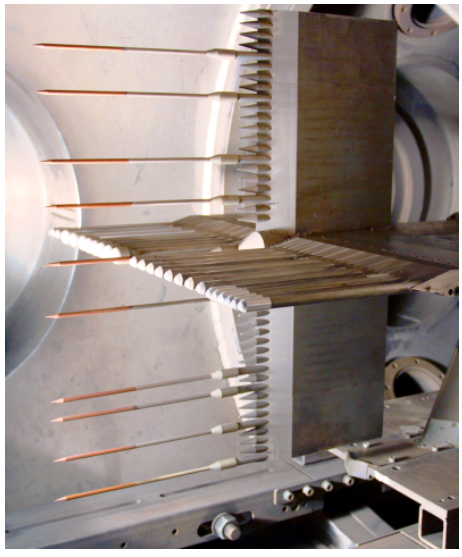

(a)

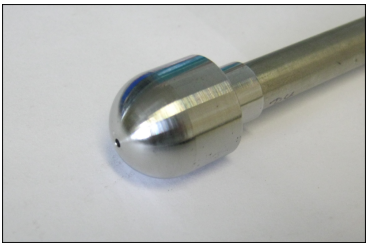

(b)

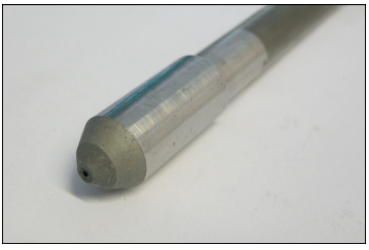

(c)

Figure A.2: a: Calibration rake. b: Half sphere wall heat flux probe (without instrumentation). c: Pitot pressure probe.

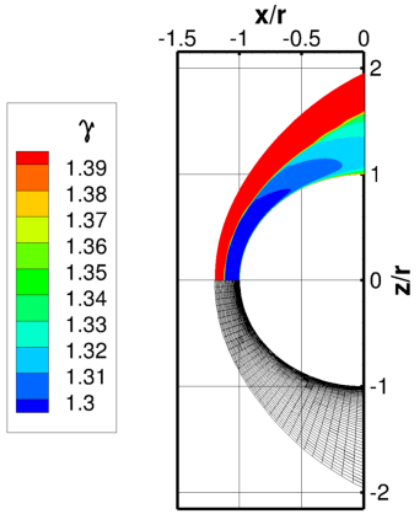

Figure A.3: Contour of the isentropic exponent γ and grid around the half-sphere.

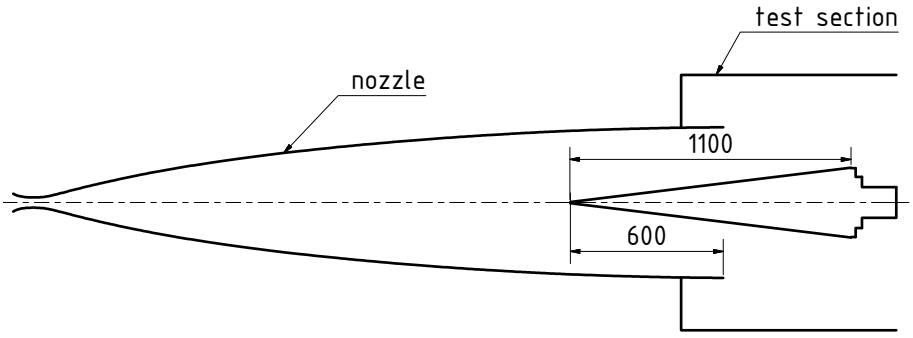

Figure A.4: Schematic view of the HEG Mach 8 nozzle and test section containing a cone model. All dimensions are provided in millimeter.

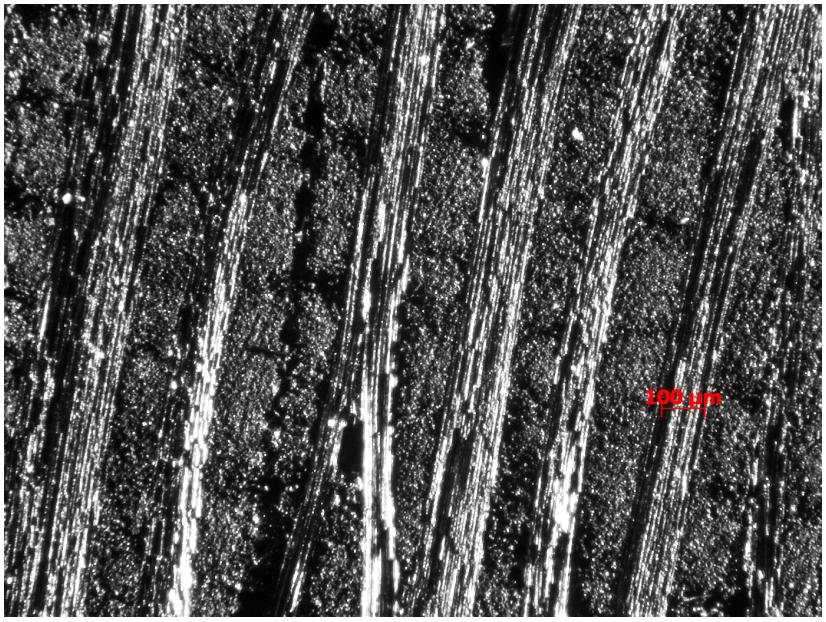

Figure A.5: Microscopic view of carbon-carbon ceramics.

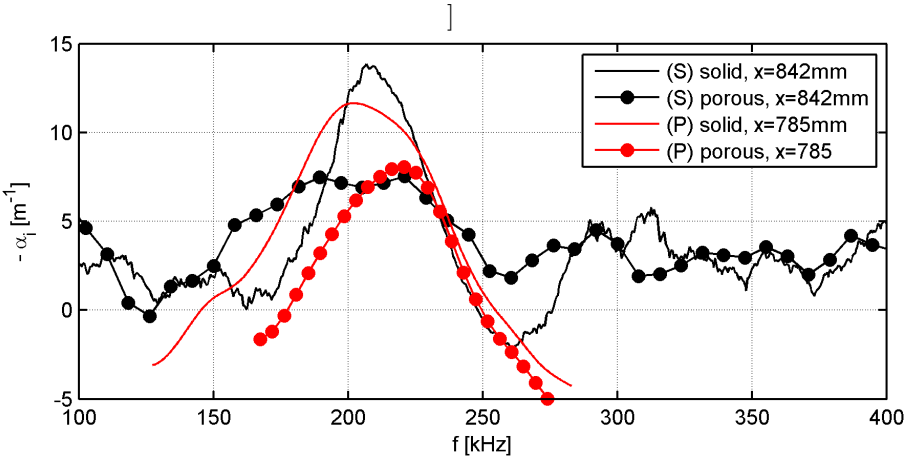

Figure A.6: Comparison of the spacial amplification rates based on schlieren deflectometry (S) and fast response pressure transducers (P), $\mathrm{Re_m} = 1.5 \cdot 10^6$ m^{-1}, $\mathrm{R_n} = 2.5$ mm.

$Re_m[m^{-1}]$ ->	$1.46 \cdot 10^6$	$2.4 \cdot 10^6$	$3.6 \cdot 10^6$ *	$4.0 \cdot 10^6$	$6.4 \cdot 10^6$	$9.8 \cdot 10^6$ **
p_0 $[MPa]$	6.8 (4.2%)	12.7 (1.7%)	15.8 (1.8%)	19.2 (4.2%)	28.4 (3.6%)	47.3
T_0 $[K]$	2720 (2.2%)	2895 (1.6%)	2620 (0.8%)	2734 (1.1%)	2582 (1.0%)	2835
h_0 $[MJ/kg]$	3.25 (6.0%)	3.48 (2.0%)	3.37 (0.9%)	3.24 (1.4%)	3.03 (0.9%)	3.4
M_∞ $[-]$	7.3 (0.2%)	7.3(0.2%)	7.4 (0.1%)	7.4 (0.2%)	7.4 (0.2%)	7.4
p_∞ $[Pa]$	789 (3.4%)	1453 (2.2%)	19.2 (4.2%)	2129 (4.0%)	3083 (3.9%)	5174
T_∞ $[K]$	267 (1.7%)	285 (2.3%)	252 (0.8%)	268 (2.1%)	248 (1.5%)	265
ρ_∞ $[g/m^3]$	10.2 (2.5%)	17.7 (2.2%)	23.0 (0.5%)	27.6 (4.8%)	43.2 (2.8%)	67.8
u_∞ $[m/s]$	2409 (0.7%)	2480 (0.9%)	2362 (0.3%)	2422 (0.8%)	2350 (0.6%)	2419
Re_m $[10^6 m^{-1}]$	1.46 (2.7%)	2.43 (2.9%)	3.6 (6.7%)	4.06 (4.2%)	6.39 (2.3%)	9.8

Table A.2: Averaged HEG test conditions and relative standard deviations. *The condition was used on model 1 and was modified for subsequent tests. **Single run - no standard deviation provided.

Bibliography

[1] *Annual Book of ASTM Standards*, volume 14.03 of *ASTM Standard E 230-96, Standard Specification and Temperature-Electromotive Force (EMF) Tables for Standardized Thermocouples*. American Society for Testing and Materials, Philadelphia, PA, 1997.

[2] D. Adamczak, H. Alesi, and M. Frost. HIFiRE-1: Payload design, manufacture, ground test, and lessons learned. In *16th AIAA/DLR/DGLR International Space Planes and Hypersonic Systems and Technologies Conference*, 2009. AIAA 2009-7294.

[3] D. Adamczak and R. L. Kimmel. HIFiRE-1 flight trajectory estimation and initial experimental results. In *17th AIAA International Space Planes and Hypersonic Systems and Technologies Conference 11 - 14 April 2011, San Francisco, California*, 2011. AIAA 2011-2358.

[4] S. Alber. *Veränderung des Schallabsorptionsverhaltens von offenporigen Asphalten durch Verschmutzung*. PhD thesis, University of Stuttgart, 2013.

[5] J. F. Allard and Noureddine Atalla. *Propagation of Sound in Porous Media*. WILEY, 2nd edition, 2009.

[6] J. D. Jr. Anderson. *Hypersonic and High-Temperature Gas Dynamics*. Education Series. AIAA, 2nd edition, 2006.

[7] P.M. Bentley and J.T.E. McDonnell. Wavelet transforms: an introduction. *Electronics & Communication Engineering Journal*, August 1994.

[8] D. C. Berridge and S. P. Schneider. Calibration of PCB-132 sensors in a shock tube. Technical Report NF1676L-13491 (NTRS), NASA Langley Research Center; Hampton, VA, United States, April 2012.

[9] H. Böhrk. Transpiration cooling at hypersonic flight - AKTiV on SHEFEX II. In *11th AIAA/ASME Joint Thermophysics and Heat Transfer Conference*, 2014. AIAA 2014-2676.

[10] H. Böhrk, V. Wartemann, T. Eggers, J. Martinez Schramm, A. Wagner, and K. Hannemann. Shock tube testing of the transpiration-cooled heat shield experiment AKTiV. In *18th AIAA International Space Planes and Hypersonic Systems and Technologies Conferences*, 2012. AIAA 2012-5935.

[11] G. A. Brès, Tim Colonius, and A. V. Fedorov. Acoustic properties of porous coatings for hypersonic boundary-layer control. *AIAA Journal*, 48(2):267–274, February 2010.

[12] G. A. Brès, Matthew Inkman, Tim Colonius, and A. V. Fedorov. Second-mode attenuation and cancellation by porous coatings in a high-speed boundary layer. *Journal of Fluid Mechanics*, 726:312–337, 2013.

[13] P. C. Carman. Fluid flow through granular beds. *Chemical Engineering Research and Design*, 75, Supplement(0):32 – 48, 1997.

[14] M. Choudhari and Paul Fischer. Roughness-induced transient growth. In *35th AIAA Fluid Dynamics Conference and Exhibit*, 2005. AIAA 2005-4765.

[15] W. J. Cook, J. C. and E. J. Felderman. Reduction of data from thin-film heat-transfer gages - a concise numerical technique. *AIAA Journal*, 4(3):561–562, 1966.

[16] Medtherm Cooperation. Product data sheet. `http://www.medtherm.com`. Accessed: 2014-07-13.

[17] John A. Copper. Experimental investigation of the equilibrium interface technique. *Physics of Fluids*, 5(7):844–849, 1962.

[18] M. R. Davis. Measurements in a subsonic turbulent jet using a quantitative schlieren technique. *Journal of Fluid Mechanics*, M:631–656, 1971.

[19] A. Demetriades. Hypersonic viscous flow over a slender cone, part iii: Laminar instability and transition. In *AIAA 7th Fluid and Plasma Dynamics Conference*, 1974. AIAA74-535.

[20] A. Demetriades. Laminar boundary layer stability measurements at Mach 7 including wall temperature effects. Technical report, FORD Aerospace and Communications Corp Newport Beach CA AERONUTRONIC DIV, 1977.

[21] G. Eitelberg. First results of calibration and use of the HEG. In *18th AIAA Aerospace Ground Testing Conference*, 1994. AIAA 94-2525.

[22] G. Eitelberg, T. J. McIntyre, W. H. Beck, and J. Lacey. The High Enthalpy Shock Tunnel in Göttigen. In *17th AIAA Aerospace Ground Testing Conference*, 1992. AIAA 92-3942.

[23] M. Estorf, R. Radespiel, S. P. Schneider, H. B. Johnson, and S. Hein. Surface-pressure measurements of second-mode instability in quiet hypersonic flow. In *46th AIAA Aerospace Sciences Meeting and Exhibit*, Reno, Nevada, January 2008. AIAA 2008-1153.

[24] A. V. Fedorov, V. Kozlov, A. Shiplyuk, A. Maslov, and N. Malmuth. Stability of hypersonic boundary layer on porous wall with regular microstructure. *AIAA Journal*, 44(8):1866–1871, August 2006.

[25] A. V. Fedorov, V. F. Kozlov, and R. C. Addison. Reflection of acoustic disturbances from a porous coating of regular microstructure. In *5th AIAA Theoretical Fluid Mechanics Conference*, 2008. AIAA 2008-3902.

[26] A. V. Fedorov, Norman D. Malmuth, A. Rasheed, and H. G. Hornung. Stabilization of hypersonic boundary layers by porous coatings. *AIAA*, 39(4):605–610, April 2001.

[27] A. V. Fedorov, A. Shiplyuk, A. Maslov, E. Burov, and N. Malmuth. Stabilization of a hypersonic boundary layer using an ultrasonically absorptive coating. *Journal of Fluid Mechanics*, 479:99–124, 2003.

[28] NASP Task Force. Report of the defense science board task force on the national aerospace plane (NASP). Technical report, Defense Science Board, Office of the Secretary of Defense , Washington, D.C. 20301-3140, September 1988.

[29] NASP Task Force. Report of the defense science board task force on the national aerospace plane (NASP). Technical report, Defense Science Board, Office of the Secretary of Defense , Washington, D.C. 20301-3140, November 1992.

[30] S. L. Gai. Free piston shock tunnels: Development and capabilities. *Progress in Aerospace Sciences*, 29:1–41, 1992.

[31] T. Giese. Kalibrierung der Antrömungsbedingungen und Charakterisierung der Störgrößen am Hochenthalpiekanal Göttingen (HEG). Master's thesis, Technische Universität Berlin, 2013.

[32] A. E. Gill. Instabilities of "top hat" jets and wakes in compressible fluids. *Physics in Fluids*, 8:1428–1430, 1965.

[33] D. Glass, R. Dirling, H. Croop, T. J. Fry, and G. J. Frank. Materials development for hypersonic flight vehicles. In *14th AIAA/AHI Space Planes and Hypersonic Systems and Technologies Conference*, Canberra, 2006. AIAA 2006-8122.

[34] D. E. Glass. Ceramic matrix composite (CMC) thermal protection systems (TPS) and hot structures for hypersonic vehicles. In *15th AIAA Space Planes and Hypersonic Systems and Technologies Conference*, Dayton, OH, 2008. AIAA 2008-2682.

[35] R. N. Gupta, J. M. Yos, and R. A. R. A. Thompson. P. Lee. A review of reaction rates and thermodynamic and transport properties for an 11-species air model for chemical and thermal nonequilibrium calculations to 30000 K. Technical Report 1232, NASA Reference Publication, 1990.

[36] H. Hald, A. Herbertz, M. Kuhn, and M. Ortelt. Technological aspects of transpiration cooled composite structures for thrust chamber applications. In *16th AIAA/DLR/DGLR International Space Planes and Hypersonic Systems and Technologies Conference*, Bremen, 2009. AIAA 2009-7222.

[37] K. Hannemann, S. Karl, J. Martinez Schramm, and J. Steelant. Methodology of a combined ground based testing and numerical modelling analysis of supersonic combustion flow paths. *Shock Waves*, 20(5):353–366, 2010.

[38] K. Hannemann and J. Martinez Schramm. *High Enthalpy, High Pressure Short Duration Testing of Hypersonic Flows, In: Springer Handbook of Experimental Fluid Mechanics*. Springer Berlin Heidelberg, 2007.

[39] K. Hannemann, J. Martinez Schramm, and S. Karl. Recent extensions to the High Enthalpy Shock Tunnel Göttingen (HEG). In *2nd International ARA Days*, Arcachon, France, October 2008.

[40] K. Hannemann, M. Schnieder, B. Reimann, and J. Martinez Schramm. The influence and the delay of driver gas contamination in HEG. In *21th AIAA Aerodynamic Measurement Technology and Ground Testing Conference*. AIAA, June 2000. AIAA 2000-2593.

[41] B. Heidenreich. Manufacture and applications of C/C-SiC and C/SiC composites. In J. P. Singh, N. P. Bansal, T. Goto, J. Lamon, S. R. Choi, M. M. Mahmoud, and G. Link, editors, *Processing and Properties of Advanced Ceramics and Composites IV*, volume 234. John Wiley & Sons, Inc., 2012.

[42] B. Heidenreich, S. Hofmann, M. Keck, R. Jemmali, M. Frieß, and D. Koch. C/C-SiC materials based on melt infiltration - manufacturing methods and experiences from serial production. In L. Zhang and D. Jiang, editors, *High Temperature Ceramic Matrix Composites 8: Ceramic Transactions*, volume 248. John Wiley & Sons, 2014.

[43] S. Hein, F. P. Bertolotti, M. Simen, A. Hanifi, and D. Henningson. Linear nonlocal instability analysis - the linear NOLOT code. Technical Report IB-223-94 A56, DLR, 1994.

[44] J. Hofferth, R. Humble, D. Floryan, and W. Saric. High-bandwidth optical measurements of the second-mode instability in a Mach 6 quiet tunnel. In *Aerospace Sciences Meetings*, 2013. AIAA 2013-0378.

[45] H. G. Hornung. Response of a pressure tap. `http://www2.galcit.caltech.edu/T5/publications/publications.html`. Accessed: 01.01.2013.

[46] Thorlabs Inc. Si avalanche photodetectors. `http://www.thorlabs.de/newgrouppage9.cfm?objectgroup_id=6686`. Accessed: 2014-07-13.

[47] Vision Research Inc. Phantom v1210. `http://www.visionresearch.com/Products/High-Speed-Cameras/v1210/`. Accessed: 2014-07-13.

[48] K. Itoh. Characteristics of the HIEST and its applicability for hypersonic aerothermodynamic and scramjet research. In *Progress in Astronautics and Aeronautics: Advanced Hypersonic Test Facilities*, pages 239–253, 2002.

[49] K. Itoh, S. Ueda, H. Tanno, T. Komuro, and K. Sato. Hypersonic aerothermodynamic and scramjet research using High Enthalpy Shock Tunnel. *Shock Waves*, 12:93–98, 2002.

[50] S. Karl. *Numerical investigation of a generic scramjet configuration*. Phd thesis, Technischen Universität Dresden, 2011.

[51] R. Kimmel and D. Adamczak. HIFiRE-1 background and lessons learned. In *50th AIAA Aerospace Sciences Meeting*, 2012. AIAA 2012-1088.

[52] R. L. Kimmel. Aspects of hypersonic boundary-layer transition control. In *41st Aerospace Sciences Meeting and Exhibit 6-9 January 2003, Reno, Nevada*. AIAA, 2003. AIAA 2003-772.

[53] R. L. Kimmel, D. Adamczak, D. Gaitonde, A. Rougeux, and J. R. Hayes. HIFiRE-l boundary layer transition experiment design. In *45th AIAA Aerospace Sciences Meeting and Exhibit*, January 2007. AIAA 2007-534.

[54] R. L. Kimmel, A. Demetriades, and Joseph C. Donaldson. Space-time correlation measurements in a hypersonic transitional boundary layer. *AIAA Journal*, 12(12):2484–2489, December 1996.

[55] R. M. Krek and P. A. Jacobs. STN, shock tube and nozzle calculations for equilibrium air. Department of mechanical engineering report, St. Lucia, Qld. : Department of Mechanical Engineering, The University of Queensland, 1993.

[56] Ames Aeronautical Laboratory. NACA report 1135 - equations, tables and charts for compressible flow. NACA Report 1135, National Advisory Committee for Aeronautics, Moffett Field, California, 1953.

[57] S. Laurence, A. Wagner, and K. Hannemann. Schlieren-based techniques for investigating instability development and transition in a hypersonic boundary layer. *Experiments in Fluids*, 55(8), 2014.

[58] S. Laurence, A. Wagner, K. Hannemann, V. Wartemann, H. Lüdeke, H. Tanno, and K. Ito. Time-resolved visualization of instability waves in a hypersonic boundary layer. *AIAA Journal*, Vol. 50(1):243–246, January 2012.

[59] S. Laurence, A. Wagner, Hiroshi Ozawa, and K. Hannemann. Visualization of hypersonic boundary-layer transition on a slender cone (invited). In *19th AIAA International Space Planes and Hypersonic Systems and Technologies Conference*, 2014. AIAA 2014-3110.

[60] Fei Li, M. Choudhari, Chau-Lyan Chang, R. Kimmel, D. Adamczak, and M. Smith. Transition analysis for the HIFiRE-1 flight experiment. In *Fluid Dynamics and Co-located Conferences*, 2011.

[61] R. Longstaff and A. Bond. The SKYLON project. In *17th AIAA International Space Planes and Hypersonic Systems and Technologies Conference*, 2011. AIAA 2011-2244.

[62] Cavitar Ltd. Cavilux smart. `http://www.cavitar.com/solutions_and_services/illumination_lasers/products/cavilux_smart`. Accessed: 2014-07-13.

[63] F. Lu. *Advanced Hypersonic Test Facilities*. Progress in Astronautics and Aeronautics. AIAA, 2002.

[64] S. V. Lukashevich, A. A. Maslov, A. N. Shiplyuk, A. V. Fedorov, and V. G. Soudakov. Stabilization of high-speed boundary layer using porous coatings of various thicknesses. *AIAA Journal*, 50(9):1897–1904, September 2012.

[65] S. V. Lukashevich, S. O. Morozov, and A. N. Shiplyuk. Experimental study of the effect of a passive porous coating on disturbances in a hypersonic boundary layer 1. Effect of the porous coating length. *Journal of Applied Mechanics and Technical Physics*, 54(4):572–577, 2013.

[66] J. Lukasiewicz and S. Bogdonoff. *Experimental Methods of Hypersonics*. Krieger Publishing Company, 2nd edition edition, 1996.

[67] A. Mack and V. Hannemann. Validation of the unstructured DLR-TAU-Code for hypersonic flows. In *32nd AIAA Fluid Dynamics Conference and Exhibit*, St. Louis, Missouri, 24-26 June 2002. AIAA 2002-3111.

[68] L. M. Mack. The stability of the compressible laminar boundary layer according to a direct numerical solution. part IV. In *Space Programs Summary*, volume 37-24, pages 271–274. Jet Propulsion Laboratory, Pasadena, CA, 1963.

[69] L. M. Mack. Boundary layer stability theory. Technical Report NASA-CR-131501, Jet Propulsion Laboratory, NASA, 1969.

[70] L. M. Mack. Linear stability theory and the problem of supersonic boundary-layer transition. *AIAA Journal*, 13(3):278 – 289, 1975.

[71] L. M. Mack. Boundary layer linear stability theory. *AGARD - Special Course on Stability and Transition of Laminar Flow*, 1984.

[72] L. M. Mack. Stability of axisymmetric boundary layers on sharp cones at hypersonic mach numbers. In *19th AIAA, Fluid Dynamics, Plasma Dynamics, and Lasers Conference*, 1987. AIAA 1987-1413.

[73] L. M. Mack. On the inviscid acoustic-mode instability of supersonic shear flows. *Theoretical and Computational Fluid Dynamics*, 2:97–123, 1990.

[74] M. R. Malik. Prediction and control of transition in supersonic and hypersonic boundary layers. *AIAA Journal*, 27(11):1487–1493, 1989.

[75] N. Malmuth, A. Fedorov, V. Shalaev, J. Cole, A. Khokhlov, M. Hites, and D. Williams. Problems in high speed flow prediction relevant to control. In *2nd AIAA, Theoretical Fluid Mechanics Meeting*, 1998. AIAA 98-2695.

[76] A. A. Maslov. Experimental and theoretical studies of hypersonic laminar flow control using ultrasonically absorptive coatings (UAC). Technical report, ISTC 2172-2001, 2003.

[77] A. A. Maslov, A. V. Fedorov, D. A. Bountin, A. N. Shiplyuk, A. A. Sidorenko, N.D. Malmuth, and H. Knauss. Experimental study of transition in hypersonic boundary layer on ultrasonically absorptive coating with random porosity. In *46th AIAA Aerospace Sciences Meeting and Exhibit*, Reno, Nevada, 7 - 10 January 2008. AIAA 2008-587.

[78] A. A. Maslov, A. Shiplyuk, A. Sidorenko, P. Polivanov, A. Fedorov, V. Kozlov, and N. Malmuth. Hypersonic laminar flow control using a porous coating of random microstructure. In *44th AIAA Aerospace Sciences Meeting and Exhibit*, Reno, Nevada, 9 - 12 January 2006. AIAA 2006-1112.

[79] S. McIntyre and G. Settles. Optical experiments on axisymmetric compressible turbulent mixing layers. In *Aerospace Sciences Meetings*, 1991. AIAA 1991-0623.

[80] R. Morgan. *Free piston driven reflected shock tunnels, Chapter 4.2 in Handbook of Shock Waves*, volume 1. Academic Press, 2001.

[81] M. V. Morkovin. Critical evaluation of transition from laminar to turbulent shear layers with emphasis on hypersonically travelling bodies. Technical Report AFFDL-TR-68-149, Air Force Flight Dynamics Laboratory, 1969.

[82] M. V. Morkovin. Transition at hypersonic speeds. Technical Report ICASE Interim Report 1, NASA Contractor Rep. 178315, 1987.

[83] M. Möser. *Technische Akustik*. Springer, 9th edition, 2012.

[84] M. Nishida. *Shock Tubes and Tunnels: Facilities, Instrumentation, and Techniques, Chapter 4.1 in Handbook of Shock Waves*, volume 1. Academic Press, 2001.

[85] M. Ortelt, A. Herbertz, and H. Hald. Investigations on fibre reinforced combustion chamber structures under effusion cooled LOX/LH2 operation. In *45th AIAA/ASME/SAE/ASEE Joint Propulsion Conference & Exhibit*, Denver, CO, 2010. AIAA 2009-5475.

[86] N. J. Parziale, J. E. Shepherd, and H. G. Hornung. Free-stream density perturbations in a reflected-shock tunnel. *Experiments in Fluids*, 55:1665, 2014.

[87] S. R. Pate. Effects of wind tunnel disturbances on boundary-layer transition with emphasis on radiated noise: A review. In *11th Aerodynamic Testing Conference*, Colorado Springs, Colorado, March 1980. 11th Aerodynamic Testing Conference. AIAA80-0431.

[88] S. R. Pate and C. J. Schueler. Radiated aerodynamic noise effects on boundary-layer transition in supersonic and hypersonic wind tunnels. *AIAA Journal*, 7:450–457, 1969.

[89] PCB Piezotronics. Introduction to piezoelectric pressure sensors. `http://www.pcb.com/TechSupport/Tech_Pres`. Accessed: 2014-07-13.

[90] PCB Piezotronics. Product data sheet. `http://www.pcb.com/Products.aspx?m=132A31`. Accessed: 2014-07-13.

[91] J. Pittman. Commercial hypersonic aircraft still decades away, says NASA aerospace engineer. Retrieved from http://www.forbes.com, 27 December 2012.

[92] L. Prandtl. Über Flüssigkeitsbewegung bei sehr kleiner Reibung. In *Verhandlungen III, Intern. Math. Kongress, Heidelberg*, 1904.

[93] A. Rasheed. *Passive hypervelocity boundary layer control using an ultrasonically absorptive surface*. PhD thesis, California Institute of Technology Pasadena, California, 2001.

[94] A. Rasheed, H. G. Hornung, A. V. Fedorov, and N. D. Malmuth. Experiments on passive hypervelocity boundary-layer control using an ultrasonically absorptive surface. *AIAA*, 40(3):481–489, March 2002.

[95] B. Reimann, I. Johnston, and V. Hannemann. DLR TAU-Code for high enthalpy flows. In Christian Breitsamter, Boris Laschka, Hans-Joachim Heinemann, and Reinhard Hilbig, editors, *Notes on Numerical Fluid Mechanics and Multidisciplinary Design*, volume 87, pages 99–106–. Springer Berlin Heidelberg, 2004.

[96] E. Reshotko. Boundary layer instability transition and control. In *32nd Aerospace Sciences Meeting & Exhibit*. AIAA 94-0001, 32nd Aerospace Science Meeting & Exhibit, January 10-13 1994.

[97] E. Reshotko. Transient growth: A factor in bypass transition. *Physics of Fluids*, 13(5):1067–1075, May 2001.

[98] E. Reshotko and A. Tumin. Role of transient growth in roughness-induced transition. *AIAA Journal*, 42(4):766–770, 2004.

[99] I. Rosenboom, S. Hein, and U. Dallmann. Influence of nose bluntness on boundary-layer instabilities in hypersonic cone flows. In *3Oth AIAA Fluid Dynamics Conference*, 1999. AIAA 99–3591.

[100] N. R. Rotta. Effects of nose bluntness on the boundary layer characteristics of conical bodies at hypersonic speeds. Technical report AD0645668, New York Univ., N. Y. Dept. of Aeronautics and Astronautics., 1966.

[101] Shock Wave Laboratory RWTH Aachen. Coaxial thermocouples for fast heat transfer measurement. `http://www.swl.rwth-aachen.de/en/industry-solutions/thermocouples/`. Accessed: 2014-07-13.

[102] W. S. Saric, H. L. Reed, and E. J. Kerschen. Boundary-layer receptivity to freestream disturbances. *Annu. Rev. Fluid Mech.*, 34:291–319, 2002.

[103] W. S. Saric, E. Reshotko, and D. Arnal. Hypersonic laminar-turbulent transition. *Hypersonic Experimental and Computational Capability, Improvement and Validation*, 2(AGARD AR-319):2–1 to 2–27, 1998.

[104] H. Schlichting. *Grenzschicht-Theorie*. Verlag G. Braun Karlsruhe, 5. erweiterte und neubearbeitete Auflage edition, 1965.

[105] H. Schlichting and K. Gersten. *Grenzschicht-Theorie*. Springer-Verlag, Berlin, Heidelberg, 10. überarbeitete Auflage edition, 2006.

[106] S. P. Schneider. Effects of roughness on hypersonic boundary-layer transition. *Journal of Spacecraft and Rockets*, 45(2):193–209, 2008.

[107] J. Martinez Schramm. *Aerothermodynamische Untersuchung einer Wiedereintrittskonfiguration und ihrer Komponenten in einem impulsbetriebenen Hochenthalpie-Stoßkanal*. PhD thesis, Georg-August-Universität Göttingen, 2008.

[108] D. L. Schultz and T. V. Jones. *AGARD-AG-165 - Heat-transfer measurements in short-duration hypersonic facilities*. Number AGARD-AG-165. NATO Science and Technology Organization, 1973.

[109] G. S. Settles. *Schlieren and Shadowgraph Techniques: Visualizing Phenomena in Transparent Media*, volume ISBN: 3-540-66155-7. Springer Berlin Heidelberg, 2001.

[110] L. Smith. Pulsed-laser schlieren visualization of hypersonic boundary-layer instability waves. In *18th AlAA Aerospace Ground Testing Conference*, 1994. AIAA-94-2639.

[111] E. J. Softley. Boundary layer transition on hypersonic blunt, slender cones. In *2nd Fluid and Plasma Dynamics Conference*, 1969. AIAA69-705.

[112] E.J. Softley, B.C.Graber, and R.E.Zempel. Experimental observation of transition of the hypersonic boundary layer. In *AIAA 6th Aerospace Sciences Meeting*, 1968. AIAA68-39.

[113] R. J. Stalker. *An investigation of free piston compression of shock tube driver gas*. Number MT-44 in Canada Nrc Mechanical Engineering Report Mt. National Research Council of Canada, 1961.

[114] R. J. Stalker. The free-piston shock tube. *The Aeronautical Quarterly*, 17:351–370, November 1966.

[115] R. J. Stalker. A study of the free-piston shock tunnel. *AIAA Journal*, 5(12):2160–2165, December 1967.

[116] S. Stanfield, R. Kimmel, and D. Adamczak. HIFiRE-1 data analysis: Boundary layer transition experiment during reentry. In *50th AIAA Aerospace Sciences Meetings*, 2012. AIAA 2012-1087.

[117] J. Steelant. Lapcat: an EC funded project on sustained hypersonic flight. In *57th International Astronautical Congress*, 2006.

[118] K. F. Stetson. Nosetip bluntness effects on cone frustrum boundary layer transition in hypersonic flow. In *AIAA 16th Fluid and Plasma Dynamics Conference*, 1983. AIAA-83-1763.

[119] H. Tanno, T. Komuro, K. Sato, K. Itoh, M. Takahashi, and K. Fujii. Measurement of hypersonic boundary layer transition on cone models in the free-piston shock tunnel HIEST. In *47th AIAA Aerospace Sciences Meeting*, Orlando, Florida, January 2009. AIAA 2009-781.

[120] H. Tanno, T. Komuro, K. Sato, K. Itoh, M. Takahashi, and K. Fujii. Measurement of hypersonic high-enthalpy boundary layer transition on a 7º cone model. In *48th AIAA Aerospace Sciences Meeting Including the New Horizons Forum and Aerospace Exposition*, Orlando, Florida, January 2010. AIAA 2010-310.

[121] A. Toepler. *Beobachtungen nach einer neuen optischen Methode.* Max Cohen und Sohn, Bonn, 1864.

[122] L. S. Tsyryulnikov and S.G. Mironov. Determination of ultrasound absorption characteristics of thin porous coatings. *Thermophysics and Aeromechanics*, 11(4):509–518, 2004.

[123] J. Turner, M. Hörschgen, W. Jung, A. Stamminger, and P. Turner. SHEFEX Hypersonic re-entry flight experiment; vehicle and subsystem design, flight performance and prospects. In *14th AIAA/AHI Space Planes and Hypersonic Systems and Technologies Conference*, 2006. AIAA 2006-8115.

[124] E. R. van Driest. The problem of aerodynamic heating. In *Aeronautical Engineering Review*, pages 26–41, October 1956.

[125] C. VanDercreek, M. Smith, and K. Yu. Focused schlieren and deflectometry at AEDC hypervelocity wind tunnel no. 9. In *Fluid Dynamics and Co-located Conferences*, 2010. AIAA 2010-4209.

[126] J. L. Verant. Numerical enthaplies rebuilding for perfect gas and nonequilibrium flows applications to high-enthalpy wind tunnels. Internal Report 69/6121 SY, HT-TN-E-1-201-ONER, ONERA, 1995.

[127] T. P. Wadhams, E. Mundy, M. G. Mac Lean, and M. S. Holden. Ground test studies of the HIFiRE-1 transition experiment part 1: Experimental results. *Journal of Spacecraft and Rockets*, 45(6):1134–1148, November-December 2008.

[128] A. Wagner, K. Hannemann, and M. Kuhn. Experimental investigation of hypersonic boundary-layer stabilization on a cone by means of ultrasonically absorptive carbon-carbon material. In *18th AIAA/3AF International Space Planes and Hypersonic Systems and Technologies Conference*. AIAA, September 2012. AIAA2012-5865.

[129] A. Wagner, K. Hannemann, and M. Kuhn. Ultrasonic absorption characteristics of porous carbon-carbon ceramics with random microstructure for passive hypersonic boundary layer transition control. *Experiments in Fluids*, 55(6), 2014.

[130] A. Wagner, K. Hannemann, V. Wartemann, and T. Giese. Hypersonic boundary-layer stabilization by means of ultrasonically absorptive carbon-carbon material - part 1: Experimental results. In *51st AIAA Aerospace Sciences Meeting*, Texas, January 2013. AIAA 2013-0270.

[131] A. Wagner, K. Hannemann, V. Wartemann, H. Tanno, and K. Ito. Free piston driven shock tunnel hypersonic boundary layer transition experiments on a cone configuration. In *AVT - Specialists' Meeting on Hypersonic Laminar-Turbulent Transition*, RTO-MP-AVT-200, San Diego, California, USA, April 2012. RTO.

[132] A. Wagner, M. Kuhn, J. Martinez Schramm, and K. Hannemann. Experiments on passive hypersonic boundary layer control using ultrasonically absorptive carbon-carbon material with random microstructure. *Experiments in Fluids*, 54(10), 2013.

[133] A. Wagner, S. Laurence, J. Martinez Schramm, K. Hannemann, V. Wartemann, H. Lüdeke, H. Tanno, and K. Ito. Experimental investigation of hypersonic boundary-layer transition on a cone model in the High Enthalpy Shock Tunnel Göttigen (HEG) at Mach 7.5. In *17th AIAA International Space Planes and Hypersonic Systems and Technologies Conference*, San Francisco, California, USA, April 2011. AIAA 2011-2374.

[134] R. Wagnild. private communication. 04.08.2014.

[135] V. Wartemann. private communication. 22.07.2014.

[136] V. Wartemann. *Mack-Moden-Dämpfung mittels mikroporöser Oberflächen im Hyperschall*. PhD thesis, Technischen Universität Carolo-Wilhelmina zu Braunschweig, 2014.

[137] V. Wartemann, T. Giese, T. Eggers, A. Wagner, and K. Hannemann. Hypersonic boundary-layer stabilization by means of ultrasonically absorptive carbon-carbon material - part 2: Computational analysis. In *51st AIAA Aerospace Sciences Meeting*, Texas, January 2013. AIAA 2013-271.

[138] V. Wartemann, H. Lüdeke, and N. D. Sandham. Numerical investigation of hypersonic boundary-layer stabilization by porous surfaces. *AIAA Journal*, 50(6):1281–1290, June 2012.

[139] V. Wartemann, A. Wagner, T. Giese, T. Eggers, and K. Hannemann. Boundary-layer stabilization by an ultrasonically absorptive material on a cone in hypersonic flow: numerical investigations. *CEAS Space Journal*, 6(1), 2013.

[140] V. Wartemann, A. Wagner, M. Kuhn, T. Eggers, and K. Hannemann. Passive hypersonic boundary layer transition control using an ultrasonically absorptive coating with random microstructure: Computational analysis based on the ultrasonic absorption properties of carbon-carbon. In *IUTAM ABCM Symposium on Laminar Turbulent Transition*, September 2014.

[141] E. W. Washburn. The dynamics of capillary flow. *Physical Review*, 17:273–283, March 1921.

[142] H. Weihs, J. Longo, and J. Turner. Key experiments within the SHEFEX II mission. In *IAC 2008*, number IAC-08.D2.6.4, Glasgow, Scottland UK, 2008.

[143] A. JR. Whitehead. NASP aerodynamics. In *AlAA First National Aero-Space Plane Conference*, 1989. AIAA 89-5013.

[144] S. Willems and A. Gülhan. Damping of the second mode instability with regular and random porous surfaces on a slender cone in hypersonic flow. In *AVT- Specialists' Meeting on Hypersonic Laminar-Turbulent Transition*, San Diego, California, USA, April 2012.

[145] M. Zanchetta and C. Walton. ATLLAS II: D2.1.1 preliminary vehicle definition and performance. Technical report, Gas Dynamics Ltd, 2012.

Curriculum Vitae

Alexander Wagner

German Aerospace Center (DLR)
Spacecraft Department
Bunsenstraße 10, Göttingen 37073
Germany

Phone: (+49) 551-7092648
Fax: (+49) 551-7092800
Email: Alexander.Wagner@dlr.de
Homepage: http://www.dlr.de/as/en

Personal

Born on September 27, 1981.
Germany.

Education

2001-2007 Dipl.-Ing., University of Technology Dresden, Germany
Specialization in Aerospace Engineering. Graduated with "sehr gut" (highest grade).

2007-2008 Diploma Course, von Karman Institute, Belgium.
Investigation on roughness induced transition at the VKI Longshot facility. Graduated with distinction.

2011-2014 Ph.D., Katholieke Universiteit Leuven, Belgium.
Passive hypersonic boundary layer transition control using ultrasonically absorptive carbon-carbon ceramic with random microstructure.

Awards

2007 DLR-Technology Price
Student Research Project on *Thermography based investigation of laminar-turbulent boundary layer transition on a wing by means of wind tunnel testing and free flight.*
University of Technology Dresden.

Employment

2008-2014 German Aerospace Center (DLR).
Research Associate.

Publications

An up-to-date list of all publications is provided online:

`www.researchgate.net/profile/Alexander_Wagner4`

Last updated: October 14, 2014

List of publications

Journal Publications

First Author

- A. Wagner, M. Kuhn, J. Martinez Schramm and K. Hannemann. Experiments on passive hypersonic boundary layer control using ultrasonically absorptive carbon-carbon material with random microstructure. *Experiments in Fluids*, 54(10), 2013.

- A. Wagner, K. Hannemann and M. Kuhn. Ultrasonic absorption characteristics of porous carbon-carbon ceramics with random microstructure for passive hypersonic boundary layer transition control. *Experiments in Fluids*, 55(6), 2014.

Coauthor

- S. Laurence, A. Wagner, K. Hannemann, V. Wartemann, H. Lüdeke, H. Tanno and K. Ito. Time-resolved visualization of instability waves in a hypersonic boundary layer. *AIAA Journal*, Vol. 50(1), 2012.

- V. Wartemann, A. Wagner, T. Giese, T. Eggers and K. Hannemann. Boundary-layer stabilization by an ultrasonically absorptive material on a cone in hypersonic flow: numerical investigations. *CEAS Space Journal*, 6(1), 2013.

– S. Laurence, A. Wagner and K. Hannemann. Schlieren-based techniques for investigating instability development and transition in a hypersonic boundary layer. *Experiments in Fluids*, 55(8), 2014.

– N. D. Sandham, E. Schülein, A. Wagner, S. Willems and J. Steelant. Transitional shock-wave/boundary-layer interactions in hypersonic flow. *Journal of Fluid Mechanics*, 752, pp 349 – 382, 2014.

Conference Publications

First Author

– A. Wagner, S. Laurence, J. Martinez Schramm, K. Hannemann, V. Wartemann, H. Lüdeke, H. Tanno and K. Ito. Experimental investigation of hypersonic boundary-layer transition on a cone model in the High Enthalpy Shock Tunnel Göttigen (HEG) at Mach 7.5. *17th AIAA International Space Planes and Hypersonic Systems and Technologies Conference*, AIAA 2011-2374, 2011.

– A. Wagner, K. Hannemann and M. Kuhn. Experimental investigation of hypersonic boundary-layer stabilization on a cone by means of ultrasonically absorptive carbon-carbon material. *In 18th AIAA/3AF International Space Planes and Hypersonic Systems and Technologies Conference*, AIAA 2012-5865, 2012.

– A. Wagner, K. Hannemann and T. Eggers. Recent Aerothermodynamic Studies in the High Enthalpy Shock Tunnel Göttingen (HEG). *International Symposium on Hypersonic Aerothermodynamics - Recent Advances*, Bangalore, India, 2012.

– A. Wagner, K. Hannemann, V. Wartemann, H. Tanno and K. Ito. Free piston driven shock tunnel hypersonic boundary layer transition experiments on a cone configuration. *AVT - Specialists' Meeting on Hypersonic Laminar-Turbulent Transition*, RTO-MP-AVT-200, 2012.

– A. Wagner and K. Hannemann. Stabilization of a hypersonic boundary layer on a cone by means of ultrasonically absorptive carbon-carbon material (Invited). *California Institute of Technology Seminar*, Pasadena, California, USA, 2012.

– A. Wagner, K. Hannemann, V. Wartemann and T. Giese. Hypersonic boundary-layer stabilization by means of ultrasonically absorptive carbon- carbon material - Part 1: Experimental Results. *51st AIAA Aerospace Sciences Meeting*, AIAA 2013-0270, 2013.

– A. Wagner, V. Wartemann, K. Hannemann and T. Eggers. Experimental investigations of hypersonic boundary-layer stabilization by means of porous surfaces (Invited). *Texas A&M University Seminar*, College Station, Texas, USA, 2013.

– A. Wagner, V. Wartemann, M. Kuhn, J. Martinez Schramm and K. Hannemann. Experimental investigation of hypersonic boundary layer transition delay by means of ultrasonically absorptive carbon-carbon material in the High Enthalpy Shock Tunnel Göttingen (HEG). *Lecture Series on high-speed laminar-turbulent transition*, von Karman Institute, Bruxelles, Belgium, 2013.

Coauthor

– J. Martinez Schramm, A. Wagner, J. Wolfram, K. Hannemann, T. Barth and J.-D. Mulot. Post Flight Experiments of the SHEFEX I Configuration in the High Enthalpy Shock Tunnel Göttingen (HEG). *27th International Symposium on Shock Waves*, St. Petersburg, Russia, 2009.

– J. Martinez Schramm, A. Wagner, J. Wolfram, K. Hannemann, T. Barth, J.-D. Mulot and A. Schröder. Post flight analysis of SHEFEX I: Shock tunnel testing and related CFD analysis. *16th AIAA/DLR/DGLR International Space Planes and Hypersonic Systems and Technologies Conference*, Bremen, Germany, 2009.

– K. Hannemann, J. Martinez Schramm, A. Wagner, S. Karl and V. Hannemann. A Closely Coupled Experimental and Numerical Approach for Hypersonic and High Enthalpy Flow Investigations Utilising the HEG Shock Tunnel and the DLR TAU Code. *NATO Research and Technology Organisation. Aerothermodynamic Design, Review on Ground Testing and CFD*, Rhode St. Genese, Belgium, 2010.

- J. Martinez Schramm, T. Barth, A. Wagner and K. Hannemann. Post Flight Analysis of SHEFEX I: Shock Tunnel Testing and Related CFD Analysis. *7th European Symposium on Aerothermodynamics for Space Vehicles*, Brugge, Belgium, 2011.

- J. Martinez Schramm, A. Wagner, B. Reimann, M. Fertig, P. Viguier, J.-L. Verant. Measurements on the EXOMARS Configuration in the High Enthalpy Shock Tunnel Göttingen (HEG). *7th European Symposium on Aerothermodynamics for Space Vehicles*, Brugge, Belgium, 2011.

- H. Böhrk, V. Wartemann, T. Eggers, J. Martinez Schramm, A. Wagner and K. Hannemann. Shock Tube Testing of the Transpiration-Cooled Heat Shield Experiment AKTiV. *18th AIAA International Space Planes and Hypersonic Systems and Technologies Conferences*, AIAA 2012-5935, 2012.

- V. Wartemann, T. Giese, T. Eggers, A. Wagner and K. Hannemann. Hypersonic boundary-layer stabilization by means of ultrasonically absorptive carbon-carbon material - Part 2: Computational Analysis. *51st AIAA Aerospace Sciences Meeting*, AIAA 2013-271, 2013.

- S. Laurence, A. Wagner and K. Hannemann. Investigation of hypersonic boundary-layer transition using high speed visualization techniques. *29th International Symposium on Shock Waves*, Madison, Wi, USA, 2013.

- S. Laurence, A. Wagner, H. Ozawa and K. Hannemann. Visualization of Hypersonic Boundary-Layer Transition on a Slender Cone (Invited). *19th AIAA International Space Planes and Hypersonic Systems and Technologies Conference*, AIAA 2014-3110, 2014.

- V. Wartemann, A. Wagner, M. Kuhn, T. Eggers and K. Hannemann. Passive hypersonic boundary layer transition control using an ultrasonically absorptive coating with random microstructure: Computational analysis based on the ultrasonic absorption properties of carbon-carbon. *IUTAM ABCM Symposium on Laminar Turbulent Transition*, September 2014.

Arenberg Doctoral School of Science, Engineering & Technology
Faculty of Engineering
Department of Mechanical Engineering
Research group ...
Celestijnenlaan 300C box 2402
3001 Leuven, Belgium

KATHOLIEKE UNIVERSITEIT LEUVEN